









# The Evaporating Massive Embedded Stellar Cluster IRS 13 Close to Sgr A\*. I. Detection of a rich population of dusty objects in the IRS 13 cluster

FLORIAN PEIßKER <sup>1</sup>, MICHAL ZAJAČEK <sup>2</sup>, LAURITZ THOMKINS,<sup>1</sup> ANDREAS ECKART <sup>1,3</sup>, LUCAS LABADIE <sup>1</sup>,  
VLADIMÍR KARAS <sup>4</sup>, NADEEN B. SABHA <sup>5</sup>, LUKAS STEINIGER <sup>1</sup> AND MARIA MELAMED <sup>1</sup>

<sup>1</sup>*I. Physikalisches Institut der Universität zu Köln, Zùlpicher Str. 77, 50937 Köln, Germany*

<sup>2</sup>*Department of Theoretical Physics and Astrophysics, Faculty of Science, Masaryk University, Kotlářská 2, 611 37 Brno, Czech Republic*

<sup>3</sup>*Max-Planck-Institut für Radioastronomie, Auf dem Hügel 69, 53121 Bonn, Germany*

<sup>4</sup>*Astronomical Institute, Czech Academy of Sciences, Boční II 1401, CZ-14100 Prague, Czech Republic*

<sup>5</sup>*Institut für Astro- und Teilchenphysik, Universität Innsbruck, Technikerstr. 25, 6020 Innsbruck, Austria*

## ABSTRACT

A detailed analysis of the Nuclear Stellar Cluster (NSC) concedes not only the existence of the S-cluster with its fast-moving stars and the supermassive black hole (SMBH) Sgr A\*. It also reveals an embedded region of gas and dust with an exceptionally high stellar density called IRS 13. The IRS 13 cluster can be divided into the northern and the eastern counterparts, called IRS 13N and IRS 13E, respectively. This work will focus on both regions and study their most prominent members using rich infrared and radio/submm data baselines. Applying a multiwavelength analysis enables us to determine a comprehensive photometric footprint of the investigated cluster sample. Using the raytracing-based radiative transfer model HYPERION, the spectral energy distribution of the IRS 13 members suggests a stellar nature of the dusty sources. These putative Young Stellar Objects (YSOs) have a comparable spectroscopic identification to the D and G sources in or near the S cluster. Furthermore, we report the existence of a population of dusty sources in IRS 13 that can be mostly identified in the H-, K-, and L-band. Together with the objects reported in literature, we propose that this population is the outcome of a recent star formation process. Furthermore, we report that these presumably young objects are arranged in a disk structure. Although it cannot be excluded that the intrinsic arrangement of IRS 13 does show a disk structure, we find indications that the investigated cluster sample might be related to the counterclockwise disk.

*Keywords:* editorials, notices — miscellaneous — catalogs — survey

## 1. INTRODUCTION

The bright and variable radio source Sgr A\*, identified as the supermassive black hole (SMBH), is located at the center of the Nuclear Star Cluster (NSC; Menten et al. 1997; Eckart et al. 2017; Tursunov et al. 2020; Genzel 2022). Sheltering a rich depot of various types of stars, the NSC in the Galactic center (GC) enables detailed studies of its structure and components (Schödel et al. 2009; Baumgardt et al. 2018; Shahzamanian et al. 2022). As a prominent sub-structure of the NSC, the IRS 13 cluster has drawn attention because of the possibility of hosting an intermediate-mass black hole (IMBH) with

several  $\sim 10^4 M_{\odot}$  (see Portegies Zwart & McMillan 2002; Maillard et al. 2004; Schödel et al. 2005). Although every attempt to find such an IMBH resulted in a dead end (see the X-ray observations in Zhu et al. 2020; Wang et al. 2020), the question remains why the embedded cluster IRS 13 seems to resist the gravitational, and consequently disruptive, influence of Sgr A\* (Mužić et al. 2008). With this correlation in mind, Tsuboi et al. (2017a) analyzed the ionized gas associated with IRS 13E showing velocities of up to several hundred km/s on a highly eccentric orbit around a central component of the cluster, namely E3 (Fritz et al. 2010). Tsuboi et al. suggested that the blue and redshifted velocities might indicate the presence of an IMBH responsible for the circular motion of the ionized gas. Although the existence of an IMBH is disputed (Zhu et al. 2020), the

IRS 13 cluster features various additional fruitful scientific topics (Paumard et al. 2006). For example, Eckart et al. (2004) investigated the population of presumably Young Stellar Objects (YSOs) in IRS 13N. Photometric analysis of these dusty IRS 13N objects showed similarities with the D-sources (also donated as G-sources, see Peißker et al. 2020b; Ciurlo et al. 2020) in the S-cluster (Eckart et al. 2004, 2013) suggesting a common nature. On larger scales, and in comparison with the observations of single objects such as the mentioned D-sources, Lutz et al. (1993) analyzed the forbidden iron line emission in the *inner parsec* showing a bow-shock-like distribution. The strongest [FeIII] emission was located at the position of the IRS 13 cluster, which also included the region of the prominent early-type star IRS 2L (Buchholz et al. 2013; Roche et al. 2018). As we found in Peißker et al. (2020b), all the dusty objects located to the west of the Br $\gamma$ -bar (Schödel et al. 2011; Peißker et al. 2020c) do exhibit prominent [FeIII] lines, while the spectra of all the sources, which are located in projection to the east of the bar, do not exhibit [FeIII] emission. The basic mechanism behind this dichotomy is still under debate and may be part of a larger scientific frame (Jalali et al. 2014; Peißker et al. 2021c) that will be discussed in the upcoming publications.

A different debate accompanies the analysis of the dusty sources of the Galactic center (for an overview, see Peißker et al. 2020b; Ciurlo et al. 2020). This discussion started with the observation of the fast-moving G2 a decade ago (Gillessen et al. 2012). While the authors of Gillessen et al. proposed a coreless cloud nature of the object, several follow-up studies questioned this classification and suggested a stellar origin to explain the emission of G2 (Murray-Clay & Loeb 2012; Scoville & Burkert 2013; Eckart et al. 2013; Zajaček et al. 2014; Shahzamanian et al. 2016; Zajaček et al. 2017). Currently, numerous authors are in favor of a stellar nature of G2, especially because of the missing flare activity of Sgr A\* that was proposed for the periape. For example, Witzel et al. (2014) showed a point-like L-band source close to Sgr A\* with no elongation. Recently, we underlined the classification of G2 as a low-mass star embedded in a dusty envelope by analyzing a large data baseline covering the epochs between 2005-2019 (Peißker et al. 2021c). Observations of other objects, such as X7 (Clénet et al. 2003; Clénet et al. 2005; Mužić et al. 2010), revealed a similar nature compared to G2 (Peißker et al. 2021a). The data suggest that these dusty sources belong to a stellar subclass which shows characteristics similar to YSOs (Lada 1987). Based on observed colors of dusty sources found in IRS 13, Eckart et al. (2004) classified the investigated objects as YSOs. In this work, we will

focus on the dusty sources of IRS 13, which seem to follow the same morphology as G2, X7, and the D-sources (Peißker et al. 2020b, 2021c).

Based on a multi-wavelength photometric analysis, we use the radiative transfer code HYPERION (Robitaille 2011) to investigate the stellar type of the dusty sources. Furthermore, we test the validity of HYPERION by analyzing the flux density distribution of IRS 3. In addition to the dusty sources found in Eckart et al. (2004), we identify 33 newly discovered objects that can be observed in the H-, K-, and L-band. For this new population of objects, we find a similar photometric footprint compared to the literature known dusty sources suggesting a similar nature. Compared with a uniform cluster, IRS 13 seems to show an underlying pattern regarding the normalized angular momentum vector, which advocates a counterclockwise disk membership. However, this particular point will be investigated in detail in Paper II. In this paper, we focus on the detection and analysis of the newly discovered sources and the classification of the dusty objects. This work is structured as follows. In Sec. 2, we will list the used instruments and the related telescopes. We also give an overview of the used methods and tools for the analysis. Section 2 is followed by the results in Sec. 3 where we present the identification and the analysis of the dusty sources of the IRS 13N cluster. The results of Sec. 3 are discussed in Sec. 4. Subsequent to Sec. 4, we conclude the discussion in Sec. 5. In Appendix A, we list the used data and show supporting results of our analysis presented.

## 2. DATA AND TOOLS

In this section, we will introduce the instruments that were used to observe the GC and describe the applied techniques for the analysis. The public available archival data is listed in Appendix A.

### 2.1. SINFONI and NACO

The Spectrograph for INtegral Field Observations in the Near Infrared (SINFONI, Eisenhauer et al. 2003; Bonnet et al. 2004) and Nasmyth Adaptive Optics System (NAOS) – Near-Infrared Imager and Spectrograph (CONICA), abbreviated as NACO (Lenzen et al. 2003; Rousset et al. 2003), were mounted at the Very Large Telescope on top of Cerro Paranal (Chile). The near-infrared imager NACO operates in the H-, K-, L-, and M-band and provides a set of narrow filters. NACO is equipped with an S13, S27, and S54 camera with a related spatial pixel scale of 13.3 mas, 27.0 mas, and 54.3 mas, respectively.

Furthermore, SINFONI is capable of providing a spectrum along with the produced image due to its Inte-

grated Field Unit (IFU). Hence, every pixel shows a related spectrum, resulting in a 3d data cube (two spatial dimensions and one spectral dimension). The SINFONI data used here were observed in the H+K band ( $1.4 - 2.4 \mu m$ ) with a related pixel scale of  $0.1''$  and a spectral resolution of 1500. Adaptive optics is enabled for both instruments. We apply common reduction steps, like the LINEARITY/DARK correction resulting in FLAT FIELDING. The pre-mentioned reduction steps are applied to the data of both instruments. Because of the spectroscopic characteristics of SINFONI, we also use a WAVELENGTH and DISTORTION calibration. It should be noted that NACO and SINFONI are decommissioned since 2019. As a successor, ERIS (Davies et al. 2018) combines the capabilities of NACO and SINFONI.

## 2.2. ALMA

The Atacama Large (Sub)Millimeter Array (ALMA) is located on the Chajnantor plateau (Chile). The radio and submm observations can be executed between 31 and 1000 GHz. The majority of the ALMA CO data used in this work (Prog. ID: 2015.1.01080.S) is reduced with Common Astronomy Software Applications (CASA, CASA Team et al. 2022) and was analyzed and discussed in Tsuboi et al. (2017b, 2019, 2020a,b). In addition, we use scientific-ready data from the ALMA archive related to the Prog. ID 2012.1.00543.S (Martín et al. 2012; Moser et al. 2017). The ALMA data discussed and analyzed in this work shows CO v=0 (transition 3-2) at 343 GHz.

### 2.3. Radiative transfer model

For the flux analysis based on the presented multi-wavelength observations, we use the radiative transfer code HYPERION<sup>1</sup> using dust grains as ray-tracing sources (Robitaille 2011, 2017). The spectrum that serves as an input quantity for HYPERION, we use flux density values estimated from the magnitude of the related source. Consequently, we measure the peak counts of the object of interest and compare it with a reference source with known properties. For this, we use

$$\text{mag}_{\text{obj}} = \text{mag}_{\text{ref}} - 2.5 \log \left( \frac{\text{counts}_{\text{obj}}}{\text{counts}_{\text{ref}}} \right) \quad (1)$$

where  $\text{mag}_{\text{ref}}$  and  $\text{counts}_{\text{ref}}$  refer to the reference source,  $\text{mag}_{\text{obj}}$  and  $\text{counts}_{\text{obj}}$  to the analyzed object. We estimate the source flux with

$$f_{\text{obj}} = f_{\text{ref}} \times 10^{[-0.4(\text{mag}_{\text{obj}} - \text{mag}_{\text{ref}})]} \quad (2)$$

<sup>1</sup> HYPERION: an open-source parallelized three-dimensional dust continuum radiative transfer code.

where  $f_{\text{ref}}$  donates the flux (called zero flux) of the reference source. The basic settings for the code are listed in Table 1. The code allows modeling various components

Properties	Setting
Number of Photons	$10^4$
Raytracing sources	$10^2$
Number of Iterations	10

**Table 1.** Basic input parameters for HYPERION. Additional parameters for the model are listed in Sec. 3. To optimize the computational time for the investigated cluster members, we reduce the number of photons and raytracing sources by two orders of magnitude compared to the model results discussed in Peißker et al. (2023b). Due to the low coverage of the spectral distribution because of the deficient amount of flux density values, the reduced number of radiators is not reflected in a significant qualitative difference.

of YSOs, such as the gaseous accretion disk or bipolar cavities (see Fig. 1 and Sicilia-Aguilar et al. 2016). For the code used in this analysis, we model a flared disk with increasing height. The shape of the flared disk is described with

$$h_{(R)} = h_0 \left( \frac{R}{R_0} \right)^\beta \quad (3)$$

where we set  $\beta = 1.25$  following the settings used in Robitaille (2011, 2017). Furthermore, a flattened rotational and infalling dust envelope (Ulrich type, see Ulrich 1976) can be modeled depending on the flux density. Since HYPERION uses grains as emitters, the properties of dust are directly related to the outcome of the model. Therefore, in the following section, we will outline the dust model used for the radiative transfer analysis. For the assumed model that is used in HYPERION, we construct a dusty envelope and a gaseous accretion disk that are arranged around a stellar core. Due to the lack of high-resolution (spectral/spatial) IFU data covering the IRS 13 region, we cannot validate or exclude the presence of bipolar cavities (an example of these cavities is displayed in Peißker et al. 2019). In summary, our assumed model resembles the composition of a class I YSO (Fig. 1).

#### 2.3.1. Dust models

The composition of dust has a particular impact on photometric studies in the GC. It is, therefore, obvious that the evolution of dust models is coupled to a precise knowledge of the different spectral species. For example, Weingartner & Draine (2001) limit their extinction law to the presence of carbonaceous and silicate grains. In contrast, the authors of Fritz et al.

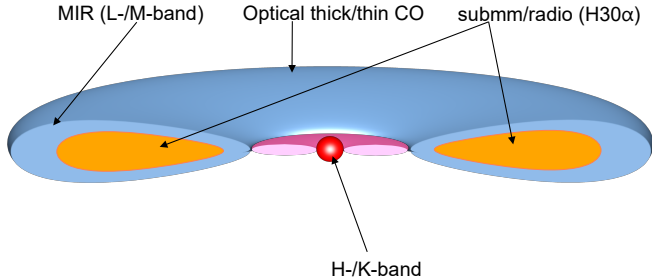


**Figure 1.** Sketch of a class I YSO. As indicated, various components are only detectable at specific wavelengths/bands. Using this model of a class I YSO, we expect higher luminous mid-infrared (L-/M-band) emission compared to the near-infrared (H-/K-band). This sketch is inspired by a similar figure shown in Sicilia-Aguilar et al. (2016).

(2011) investigated the incorporation of many more infrared emission lines such as CO, CO<sub>2</sub>, aliphates, and silicates. In addition, Fritz et al. consider the presence of ice particles (H<sub>2</sub>O and CO ice) in agreement with the studies by Moneti et al. (2001) and Moutaka et al. (2015). Fritz et al. (2011) conclude that the model of Zubko et al. (2004) is the best-fitting model to describe the extinction toward the GC. However, Zubko et al. uses  $R_V = A_V/E_{B-V} = 3.1$  which is consistent with the work by Draine (2003). Therefore, we use Draine (2003) to model the dust grains used in this work to perform a spectral analysis.

#### 2.4. High-pass filter

The high-pass filtering technique is a common tool for deblurring imaging data by minimizing the influence of the PSF wings of a bright star. While the Lucy Richardson (LR) algorithm (Lucy 1974) offers a variety of setup parameters, the smooth-subtract algorithm is a robust approach to analyzing the data. Critically, the LR algorithm tends to transform elongated structures into point sources. While this does not necessarily exclude the usage of the algorithm on regions with extended structures, IRS 13 shows elongated and compact objects with unknown nature<sup>2</sup>. The accessible implementation into the process of analyzing the data is done by smoothing the original image  $I_{\text{orig}}$  with a Gaussian kernel with a size that should be in the range of the PSF measured in

<sup>2</sup> Please see DS28 and DS33 shown in Fig. 3 which form an elongated structure with  $\alpha$ . Using the LR algorithm without the knowledge of the nature of these sources might bias the interpretation.

the data. The resulting smoothed image  $I_{\text{smo}}$  describes a low-pass filtered version of  $I_{\text{orig}}$ . With

$$I_{\text{orig}} - I_{\text{smo}} = I_{\text{high}} \quad (4)$$

we acquire the high-pass filtered version  $I_{\text{high}}$  of  $I_{\text{orig}}$ . To enhance the image quality, one can apply a Gaussian smoothing filter smaller than the PSF to  $I_{\text{high}}$ . A comparable description of this process is outlined in Peißker et al. (2022) as well. A rather qualitative comparison is presented in the following, where we investigate the astrometric and photometric imprint of the high-pass filter on the data. In general, we find no significant difference between a stellar position determined in  $I_{\text{orig}}$  or  $I_{\text{high}}$ . For the flux shown in Fig. 2, we find an uncertainty of about 20% between filtered and non-filtered data. Taking into account the usual flux density uncertainties shown, for example, in Peißker et al. (2023b) and this work, the value distribution shown in Fig. 2 is well inside the expected range. We emphasize that we expect a flux difference between high-pass filtered and non-filtered data due to the presence of elongated structures, such as the mini-spiral (see Fig. 3). High-pass filtering tends to convert elongated structures into point sources, resulting in a broader flux distribution as shown in Fig. 2. Therefore, the analysis of individual sources with the high-pass filter presented here should be carried out with caution.

### 3. RESULTS

In the following, we present the results of the multi-wavelength analysis of IRS 13. From the proper motion analysis, we derive the cluster membership of the individual sources. Using photometric measurements in various bands, we classify the observed objects and estimate the related stellar mass. In Fig. 3, we show a NACO L-band overview of the region of interest. The region displayed in Fig. 3 is called IRS 13 and can be (historically) divided up into IRS 13N and IRS 13E. The North-East nomenclature may result in confusion due to the proper motion of the IRS 13E-related sources and the coinciding IRS 13N objects. For ease of confusion, we will only use the term IRS 13 here when referring to the sources of IRS 13N and IRS 13E.

#### 3.1. Photometric analysis

The analysis of about two decades of NIR and MIR NACO data revealed 33 sources that can be observed in various bands in addition to previously known dust-enshrouded objects. In Fig. 3, we show the L-band detection of all the investigated sources in this work. In addition, Appendix D and Appendix E reveal the related H- and K-band identification of the dusty sources (DS).

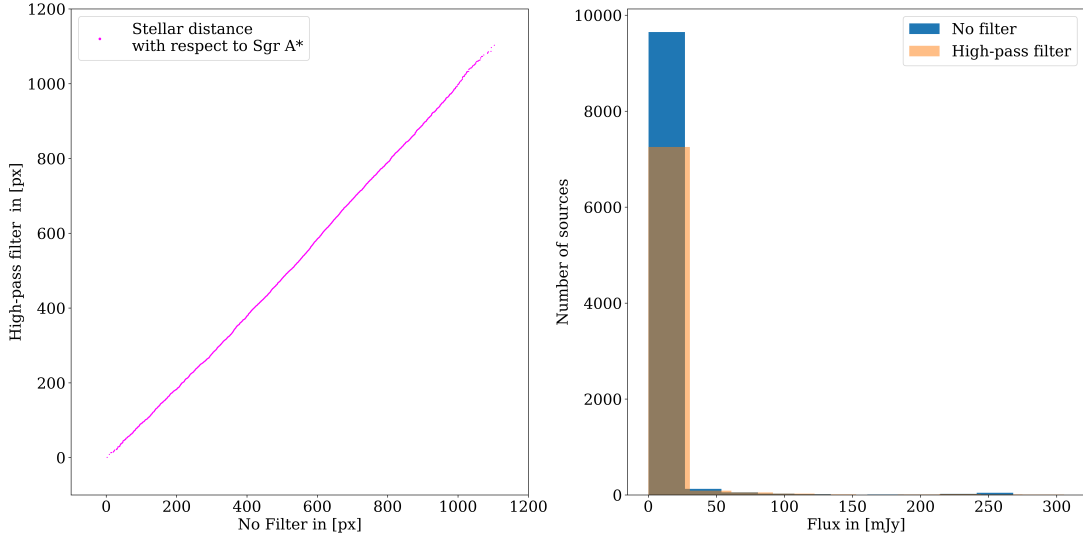


**Figure 2.** Comparison of raw data with processed data treated with a high-pass filter. The plot on the left shows the distance of several thousand stars with respect to Sgr A\*. This plot underlines the robustness of the used high-pass filter regarding an astrometric analysis since every individual star shows the same distance to Sgr A\* independent of the used approach (filter/no filter). On the right side, we show the K-band flux distribution of about 10000 stars and estimate a difference between filtered and nonfiltered data of about 20%. Please see the text for details.

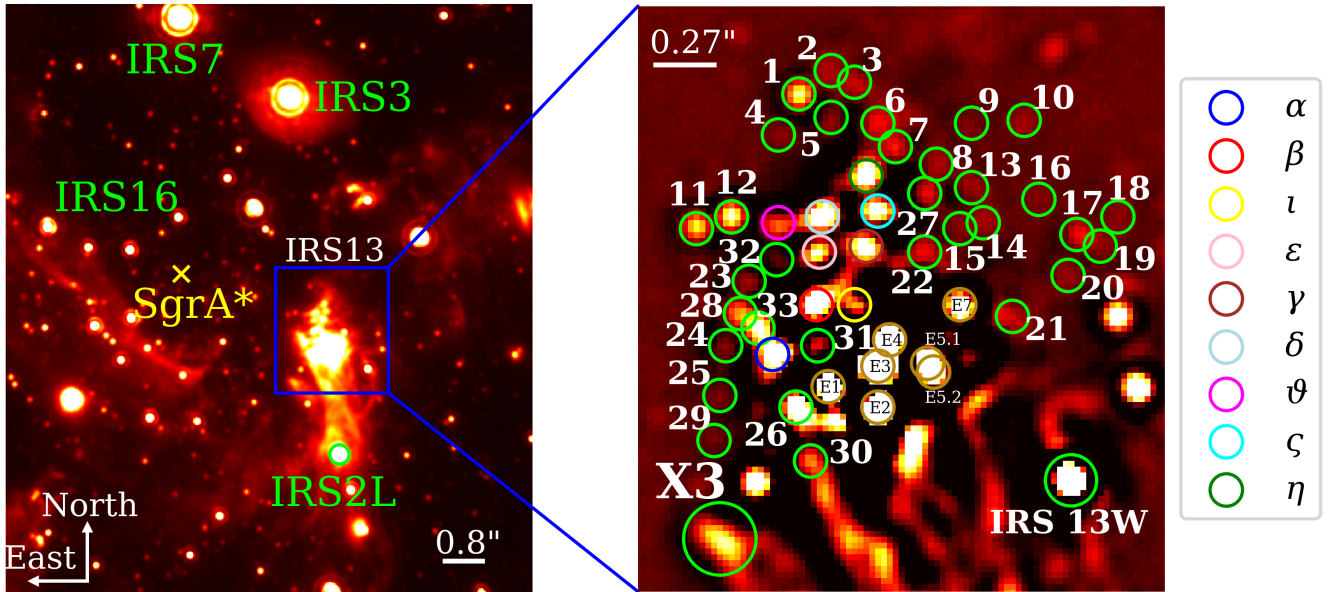


**Figure 3.** Finding chart for the dusty sources associated with a zoomed view toward the IRS 13 cluster. While the Greek-named sources are previously analyzed in the literature, we find additional sources that we enumerate to avoid confusion. The sources E1-E7 belong to IRS 13E and are marked for clarity. The bow-shock source X3 is analyzed in Peißker et al. (2023b). In addition, IRS 13W is associated with a M3 giant star (Maillard et al. 2004). The data shown was observed with NACO in 2004. Whereas the left image displays a continuum overview of the direct vicinity of Sgr A\* (about  $0.45 \times 0.50$  pc), the right represents a zoomed-in high-pass filtered view towards IRS13. Please consult Appendix D and Appendix E for the H- and K-band counterparts of the sources marked. In addition, Sec. F displays all newly identified dusty sources in the H-, K-, and L-band, including their related light curve. Every source not marked in this finding chart is not considered to be a cluster member due to its proper motion or previous studies (Pfuhl et al. 2014; Gautam et al. 2019).

The rich data set permits us to produce light curves and individual detections of all new DS objects (Ap-

pendix F). Furthermore, Table 2 lists the magnitudes of the newly discovered DS objects. We compare all

the known IRS 13 objects with the literature and list the new sources identified in Table 13, Appendix B. Consistent with the literature, we identified all known sources in the L-, K-, H-, and M-band. Because every previous analysis of the cluster covered only a fraction of the objects investigated here, our objective was to provide a complete list of all sources with a consistent nomenclature. To avoid confusion with existing studies of the region, we adapt the nomenclature for the brightest sources (E1-E7 and  $\alpha$ - $\iota$ ) of the IRS 13 cluster.

For the analysis of the data, we applied the introduced image sharpener and extracted the positions with a Gaussian fit with dimensions that correspond to the PSF of the data. The FWHM is about 5 to 6 pixels. With a spatial pixel scale for the L-band data of 27 mas, the dimensions of the corresponding PSF are about 1.3"-1.6". For the K-band data and a related spatial pixel scale of 13 mas, the dimensions of the PSF transfer to 0.6"-0.7". Since the sources studied in this work have dominant MIR emissions suffering from reduced confusion and crowding, we focus on the L-band and M-band whenever the detection of the objects in the NIR is blended. Due to the prominent and variable background of the crowded and dense cluster, we did not apply a local background subtraction since we consider confusion as the dominant source of uncertainty. Especially DS4 and DS5 suffer from confusion and blending effects that are confronted by the usage of the mean covering almost two decades of observations (Table 2).

### 3.2. Proper motion

Simultaneously to the photometric analysis presented in Sec. 3.1, we estimate the proper motion of the investigated cluster members. Due to the chance of confusion regarding the detectability of the DS sources, we use K- and L-band observations whenever possible carried out with NACO between 2002 and 2019. Except for 2014 and 2015, we trace the objects listed in Table 13 in the majority of available observations. We fit a PSF-sized Gaussian to the individual sources to extract its position (Table 3). The origin of our reference frame coincides with the position of Sgr A\*. For this, we identify the position of the B2V star S2 and use its well-known and observed orbital solution. From the orbital solution and the position of S2 (Do et al. 2019), we derive the location of Sgr A\*. We refer to Appendix C, which lists all positions of S2 and the dusty sources investigated in this work. Since the IRS 13 cluster is about 0.12 parsec away from the location of the SMBH, we assume an approximately vanishing velocity  $v_{Sgr A^*}$  of Sgr A\*. Even for objects close to Sgr A\*, the velocity effect caused by  $v_{Sgr A^*}$  is in the subpixel regime (Parsa et al. 2017).

We list the resulting proper motion of the DS sources and all other objects investigated in this work in Table 3. Due to the high degree of crowding, the standard deviation-based uncertainties may not cover the full set of entities. With upcoming JWST observations, we expect decreased astrometric uncertainties from MIRI IFU data due to unique Doppler-shifted emission lines. However, we use the results from the presented astrometric analysis to investigate the cluster and the sources for any anisotropy. We will use the approach of Eckart & Genzel (1997) and Genzel et al. (2000), where the authors used the anisotropy parameter to analyse the stellar content of the S-cluster. The anisotropy parameter is defined as

$$\gamma_{TR} = \frac{v_T^2 - v_R^2}{v_T^2 + v_R^2} \quad (5)$$

where  $v_T$  and  $v_R$  refer to the proper motion components perpendicular and parallel to the projected radius vector in the sky, respectively. The anisotropy parameter  $\gamma_{TR}$  provides an accessible numerical approach to investigate IRS 13 related objects for abnormalities. These abnormalities would imply a tendency for a specific stellar type or substructures. A uniform data point distribution indicates a continuous and randomized structure of the cluster. For example, Ali et al. (2020) expected sine-like distribution for the inclination angle. While this can not be transferred to the anisotropy parameter, the Gaussian-shaped and uniform cluster discussed in von Fellenberg et al. (2022) can be used for the expected distribution of the dusty sources. Therefore, we will investigate the cluster sample for Gaussian-like structures to investigate the presence of substructures.

In Table 3, we list the resulting proper motions of all investigated objects (Table 13) with the related distances to Sgr A\*. Using the proper motions listed in Table 3, we derive the velocity-velocity diagram (Fig. 4). From the fit and the data points displayed in Fig. 4, it is evident that the proper motion of the investigated sources shows an asymmetric distribution around the geometrical center, implying the presence of a trend. Translating this finding to a density as a function of quadrant yields:

- 1: 13 sources in a (26.5%)
- 2: 19 sources in b (38.8%)
- 3: 7 sources in c (14.3%)
- 4: 10 sources in d (20.4%)

Based on this analysis, the significance of a trend for the proper motion of the DS sources lacks a reasonable level of explicitness. From the analysis of the proper motion distribution, it is implied that the dusty sources follow

ID	H-band	K-band	L-band	K-L	$\Delta$ K-L	H-K	$\Delta$ H-K
DS1	14.40 $\pm$ 0.15	12.37 $\pm$ 0.50	10.13 $\pm$ 0.33	2.24	0.59	2.03	0.52
DS2	-	-	12.60 $\pm$ 0.24	-	-	-	-
DS3	-	-	12.30 $\pm$ 0.30	-	-	-	-
DS4	18.27 $\pm$ 0.59	15.71 $\pm$ 0.35	14.03 $\pm$ 1.41	1.68	1.45	2.56	0.68
DS5	-	-	14.37 $\pm$ 1.68	-	-	-	-
DS6	18.91 $\pm$ 0.2	17.62 $\pm$ 0.44	11.43 $\pm$ 0.54	6.19	0.69	1.29	0.48
DS7	-	-	11.54 $\pm$ 0.48	-	-	-	-
DS8	19.17 $\pm$ 0.2	17.57 $\pm$ 0.44	12.56 $\pm$ 0.76	5.01	0.87	1.60	0.48
DS9	17.11 $\pm$ 0.45	14.61 $\pm$ 0.76	13.91 $\pm$ 1.09	0.7	1.32	2.50	0.88
DS10	16.50 $\pm$ 0.31	14.19 $\pm$ 0.69	12.82 $\pm$ 0.46	1.37	0.82	2.31	0.75
DS11	14.22 $\pm$ 0.35	12.10 $\pm$ 0.70	10.46 $\pm$ 0.64	1.64	0.94	2.12	0.78
DS12	14.04 $\pm$ 0.36	11.86 $\pm$ 0.72	10.23 $\pm$ 0.60	1.63	0.93	2.18	0.80
DS13	18.55 $\pm$ 0.46	16.51 $\pm$ 0.78	12.80 $\pm$ 0.54	3.71	0.94	2.04	0.90
DS14	18.84 $\pm$ 0.94	17.33 $\pm$ 0.92	12.76 $\pm$ 0.39	4.57	0.99	1.51	1.31
DS15	18.77 $\pm$ 0.37	17.28 $\pm$ 0.53	13.65 $\pm$ 0.56	3.73	0.77	1.49	0.64
DS16	18.61 $\pm$ 0.71	17.39 $\pm$ 1.05	13.75 $\pm$ 0.83	3.64	1.33	1.22	1.26
DS17	15.68 $\pm$ 0.35	13.28 $\pm$ 0.87	11.76 $\pm$ 0.64	1.52	1.08	2.40	0.93
DS18	19.75 $\pm$ 0.95	17.49 $\pm$ 0.40	13.39 $\pm$ 0.54	4.10	0.67	2.26	1.03
DS19	19.55 $\pm$ 0.01	18.23 $\pm$ 0.64	13.95 $\pm$ 0.75	4.28	0.98	1.32	0.64
DS20	18.67 $\pm$ 0.15	15.81 $\pm$ 0.85	13.58 $\pm$ 0.72	2.23	1.11	2.86	0.86
DS21	20.23 $\pm$ 1.17	17.83 $\pm$ 1.01	12.12 $\pm$ 0.59	5.71	1.16	2.40	1.54
DS22	19.90 $\pm$ 1.21	17.40 $\pm$ 0.35	11.91 $\pm$ 0.54	5.49	0.65	2.57	1.25
DS23	18.65 $\pm$ 0.37	17.33 $\pm$ 0.59	14.73 $\pm$ 1.39	2.60	1.51	1.32	0.69
DS24	15.07 $\pm$ 0.40	13.05 $\pm$ 0.74	13.71 $\pm$ 1.65	-0.66	1.80	2.02	0.84
DS25	16.28 $\pm$ 0.30	14.49 $\pm$ 0.75	15.46 $\pm$ 1.34	-0.97	1.53	1.79	0.80
DS26	17.20 $\pm$ 0.62	15.64 $\pm$ 1.16	9.13 $\pm$ 0.59	6.51	1.30	1.56	1.31
DS27	14.83 $\pm$ 0.29	12.77 $\pm$ 0.61	12.08 $\pm$ 0.66	0.69	0.89	2.06	0.67
DS28	16.14 $\pm$ 0.27	15.80 $\pm$ 0.92	10.76 $\pm$ 0.42	5.04	1.01	0.34	0.95
DS29	16.17 $\pm$ 0.36	14.42 $\pm$ 0.86	16.29 $\pm$ 1.33	-1.87	1.58	1.75	0.93
DS30	15.67 $\pm$ 0.47	13.83 $\pm$ 0.74	10.92 $\pm$ 0.51	2.91	0.89	1.84	0.87
DS31	14.84 $\pm$ 0.29	12.97 $\pm$ 1.13	13.08 $\pm$ 2.06	-0.11	2.34	1.87	1.16
DS32	16.74 $\pm$ 0.32	15.02 $\pm$ 0.80	14.71 $\pm$ 0.93	0.31	1.22	1.72	0.86
DS33	18.39 $\pm$ 1.11	16.16 $\pm$ 0.62	9.92 $\pm$ 0.57	6.24	0.84	2.23	1.27

**Table 2.** Mean dereddened magnitudes of the DS sources analyzed in this work. We list the mean magnitude (see also Appendix B) and calculate the variance of the individual standard deviation. Hence, the uncertainty of the K-L and H-K colors is given by the square root of the variance and represent the total standard deviation.

a rather uniform arrangement, which is furthermore reflected in the Gaussian-like density probability displayed in Fig. 5. This figure shows the Gaussian distribution of the dusty sources around the geometrical center of the cluster as a function of the distance  $d$ , which is estimated with  $p_{(\text{geo})} = p_{(x,y)} - p_{\text{aver}(x,y)}$ . In the given relation,  $p_{(\text{geo})}$  is the geometrical center of the cluster,  $p_{\text{aver}(x,y)}$  the average distance of all cluster sources to Sgr A\*, and  $p_{(x,y)}$  the averaged distance of a single source between 2002 and 2018. With this, the presentation of the distribution of the DS sources shown in Fig. 5 does not reflect possible existing anomalies of the cluster. Despite the decreased surface density at about 0.6 arcsec indicated

in Fig. 5, we find a probability density consistent that resembles a Gaussian function as we would expect for a uniform cluster (Genzel et al. 2000). Because  $p_{(\text{geo})}$  does not necessarily have to be located at the highest stellar density, the Gaussian fit exhibits an offset from  $d = 0$  mas as illustrated Fig. 5. Therefore, we aim to expand the search for substructures and translate the estimated values in Table 3 into the anisotropy parameter  $\gamma_{TR}$  indicated by Eq. 5. In the first three plots displayed in Fig. 6, we show  $\gamma_{TR}$  as a function of distance from Sgr A\* for the E-stars, dusty sources, and all combined sources. The apparent continuous distribution of the data points for all sources illustrated in Fig. 4 and Fig.

ID	$r_{0,R.A.}$ (mas)	$r_{0,Dec.}$ (mas)	$v_{R.A.}$ (km/s)	$v_{Dec.}$ (km/s)	$\Delta r_{0,R.A.}$ (mas)	$\Delta r_{0,Dec.}$ (mas)	$\Delta v_{R.A.}$ (km/s)	$\Delta v_{Dec.}$ (km/s)
$\alpha$	-2677.0	-1479.1	87.4	51.6	3.2	1.9	18.9	11.5
$\beta$	-2890.0	-1246.0	73.4	115.4	3.0	4.1	16.2	21.8
$\gamma$	-3088.0	-1003.0	-73.0	170.2	3.4	3.2	18.5	7.8
$\delta$	-2903.6	-854.3	7.9	142.3	1.0	4.3	5.0	26.1
$\epsilon$	-2883.0	-1015.0	42.9	158.9	2.3	6.7	12.9	34.5
$\zeta$	-3150.8	-826.5	-128.9	203.5	5.5	7.7	31.0	42.7
$\eta$	-3104.0	-654.9	-27.8	68.0	1.2	2.7	6.6	14.8
$\vartheta$	-2700.0	-892.0	90.4	140.8	4.8	5.5	28.7	32.1
$\iota$	-3043.4	-1240.4	-54.2	81.9	3.4	4.3	18.7	23.8
1	-2795.0	-276.4	-74.0	-94.0	2.0	2.6	13.6	17.1
2	-2954.4	-175.8	9.2	248.0	4.6	10.5	26.4	60.9
3	-3070.9	-251.8	43.5	280.6	4.4	10.1	22.8	57.8
4	-2687.0	-480.3	21.2	-18.8	5.1	2.0	24.6	11.5
5	-2935.5	-408.9	-65.0	117.9	4.6	9.0	30.8	60.3
6	-3182.0	-421.7	-151.6	289.2	6.0	12.8	32.1	62.6
7	-3217.6	-531.3	-124.7	329.7	5.2	11.9	20.2	61.5
8	-3430.4	-636.4	-289.6	443.0	11.7	18.6	67.6	104.6
9	-3597.6	-435.1	31.1	-125.5	3.2	5.6	19.3	35.3
10	-3844.4	-387.9	152.5	-445.1	4.4	10.3	32.3	77.1
11	-2323.4	-891.0	12.3	-56.2	0.9	2.1	4.6	11.3
12	-2484.7	-830.9	175.1	-330.6	5.7	11.4	30.8	62.4
13	-3593.2	-723.4	-381.0	317.9	17.1	14.1	78.8	66.4
14	-3629.7	-867.4	-468.4	242.8	14.3	7.9	74.6	37.9
15	-3526.0	-917.0	-427.7	247.2	20.3	10.4	97.6	47.1
16	-3909.4	-767.9	-17.5	-106.5	3.3	5.5	21.9	33.8
17	-4106.0	-930.8	-61.6	62.1	3.9	2.8	19.6	16.2
18	-4267.0	-858.9	-191.4	-34.7	8.7	5.2	48.9	31.1
19	-4178.5	-956.4	-229.2	-100.4	13.4	7.2	67.2	35.4
20	-4017.9	-1125.5	-190.6	1.7	7.5	2.1	36.6	10.6
21	-3781.6	-1318.7	-327.4	69.3	12.9	2.8	64.7	15.6
22	-3383.1	-1021.1	-187.9	207.5	8.5	9.8	44.0	48.6
23	-2543.5	-1155.7	161.4	5.1	6.8	7.3	39.0	42.2
24	-2461.0	-1441.3	172.1	-93.8	7.8	6.4	38.8	34.1
25	-2410.6	-1687.7	152.6	5.2	5.9	2.6	30.5	13.0
26	-2801.4	-1750.3	103.3	28.9	4.7	2.0	29.5	11.5
27	-3404.0	-720.0	-51.6	-231.9	2.8	7.9	14.7	41.1
28	-2551.8	-1318.4	166.4	124.0	7.6	6.0	43.7	34.0
29	-2429.7	-1719.9	66.85	401.1	8.9	6.6	29.9	22.1
30	-2921.1	-2047.5	66.85	133.7	10.6	7.6	35.6	25.4
31	-2948.4	-1474.2	-200.5	200.5	10.7	5.4	35.6	17.5
32	-2730.0	-1064.7	-468.0	133.7	9.6	4.0	32.2	13.3
33	-2921.1	-1283.1	-200.5	-267.4	10.5	4.5	35.2	15.1
E1	-2935.0	-1637.2	-84.3	-280.0	4.9	10.9	25.4	55.9
E2	-3161.5	-1729.6	-145.2	-86.2	3.8	2.4	24.9	17.3
E3	-3171.0	-1521.0	-71.5	-135.2	3.5	5.4	19.4	27.9
E4	-3201.0	-1424.0	-182.2	23.2	8.4	6.8	38.5	36.7
E5.0	-3401.0	-1528.0	-110.6	45.4	5.2	3.9	31.1	22.0
E5.1	-3413.0	-1579.3	-317.4	-69.6	15.2	8.6	75.1	38.2
E7	-3549.0	-1260.0	148.3	-55.4	6.3	2.5	28.9	12.9

**Table 3.** Proper motions of the sources investigated in this work based on  $L$ -band observations carried out with NACO between 2002 and 2018. The uncertainties represent the standard deviation. The distance of the DS sources indicates the related position in 2002.



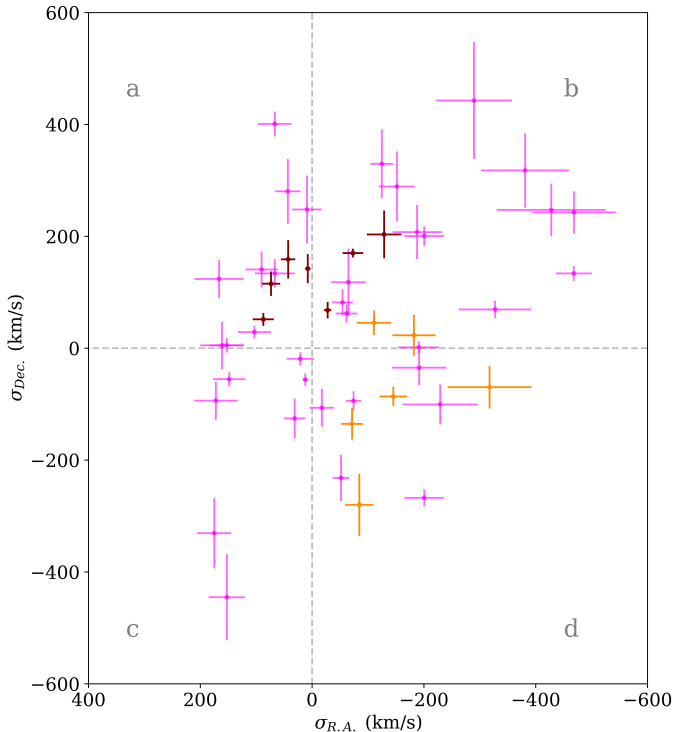


**Figure 4.** Proper motion of all observed IRS 13 sources (see Fig. 3). The E-stars (E1-E5) are orange colored, the brown data points represent the bright dusty sources ( $\alpha$ - $\eta$ ). We find a slight over and under density regarding the shown data points in the corresponding quadrant. Please see the text for details.

6 is expected due to the shared parameter. However, if we separate the distribution of the anisotropy parameter into four bins with a corresponding size of 0.5 each, we find indications for a slight overdensity close to  $\pm 1$ . In particular, we find:

- 1: 14 sources between 1.0 and 0.5
- 2: 6 sources between 0.5 and 0.0
- 3: 9 sources between 0.0 and -0.5
- 4: 19 sources between -0.5 and -1.0

We normalize the distribution to the total number of sources and estimate that about 30% of the sources are located in the 0.5 to 1.0 bin, while almost 40% can be found in the -0.5 to -1.0 bin, suggesting an overdensity of sources in bin 1 and bin 4. In particular, this overdensity is reflected in the lower right plot of Fig. 6. There, we show the normalized number of sources as a function of the anisotropy parameter  $\gamma_{TR}$ . In the same plot, we incorporate the theoretical probability distribution (PDF) with a constant anisotropy where adapt the

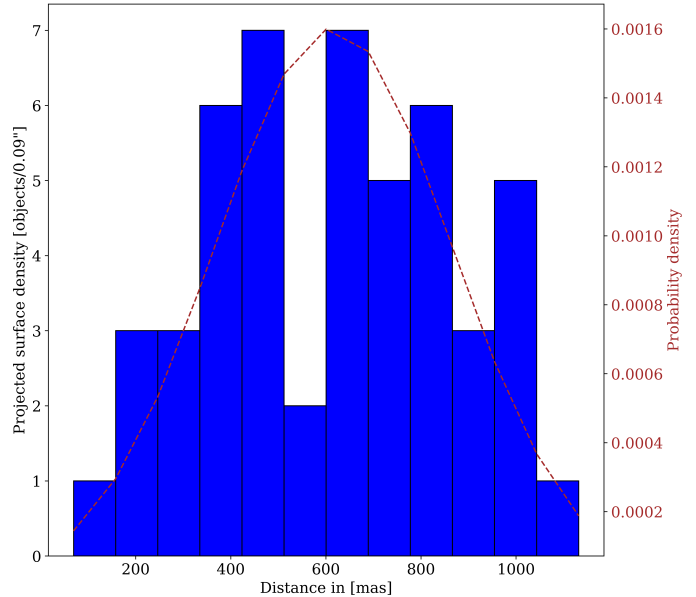


**Figure 5.** Gaussian distribution of the DS sources around the geometrical center of IRS 13. The blue-colored histogram shows the number of sources inside the bin of the size of  $0.09''$ . The brown dashed line represents a Gaussian fit to the blue-colored projected surface density. Since the geometrical center of the cluster is located in an empty region, the Gaussian probability density drops towards origin of the stellar distribution.

corresponding normalized function

$$\text{PDF}(\gamma_{TR})d\gamma_{TR} = \frac{n!(\sqrt{1 + \gamma_{TR}})^{2n-1}}{\pi(2n-1)!!\sqrt{1 - \gamma_{TR}}}d\gamma_{TR} \quad (6)$$

from Genzel et al. (2000). In the above equation,  $n$  refers to a power-law distribution index with  $\beta = 1/2 - n$ . We can now assume numerical values representing a constant anisotropy that classifies uniform clusters. For example, the magenta PDF in the lower right plot of Fig. 6 is calculated with Eq. 6 and a constant anisotropy of  $\beta = -3/2$  resembling the results of Genzel et al. (2000)<sup>3</sup>. From the data points representing the sources in IRS 13 shown in Fig. 6, it becomes directly obvious that the cluster is not uniform and shows anisotropy that peaks at  $\pm 1$  in strong agreement with Genzel et al. (2000). However, for the results displayed in Fig. 6, we picked only one numerical value for  $\beta$  to maintain clarity. To inspect the expected distribution of an anisotropic cluster, we use Monte Carlo simulations shown in Fig. 7. This figure strengthens our results which show a peak of  $\gamma_{TR}$  at  $\pm 1$  as well. In Figure 7, we simulate 10000 stars and find an overdensity at  $\gamma_{TR} \pm 1$  as for IRS13. Therefore, the investigated cluster that harbors

<sup>3</sup> Please refer to Fig. 9 in Genzel et al. (2000).

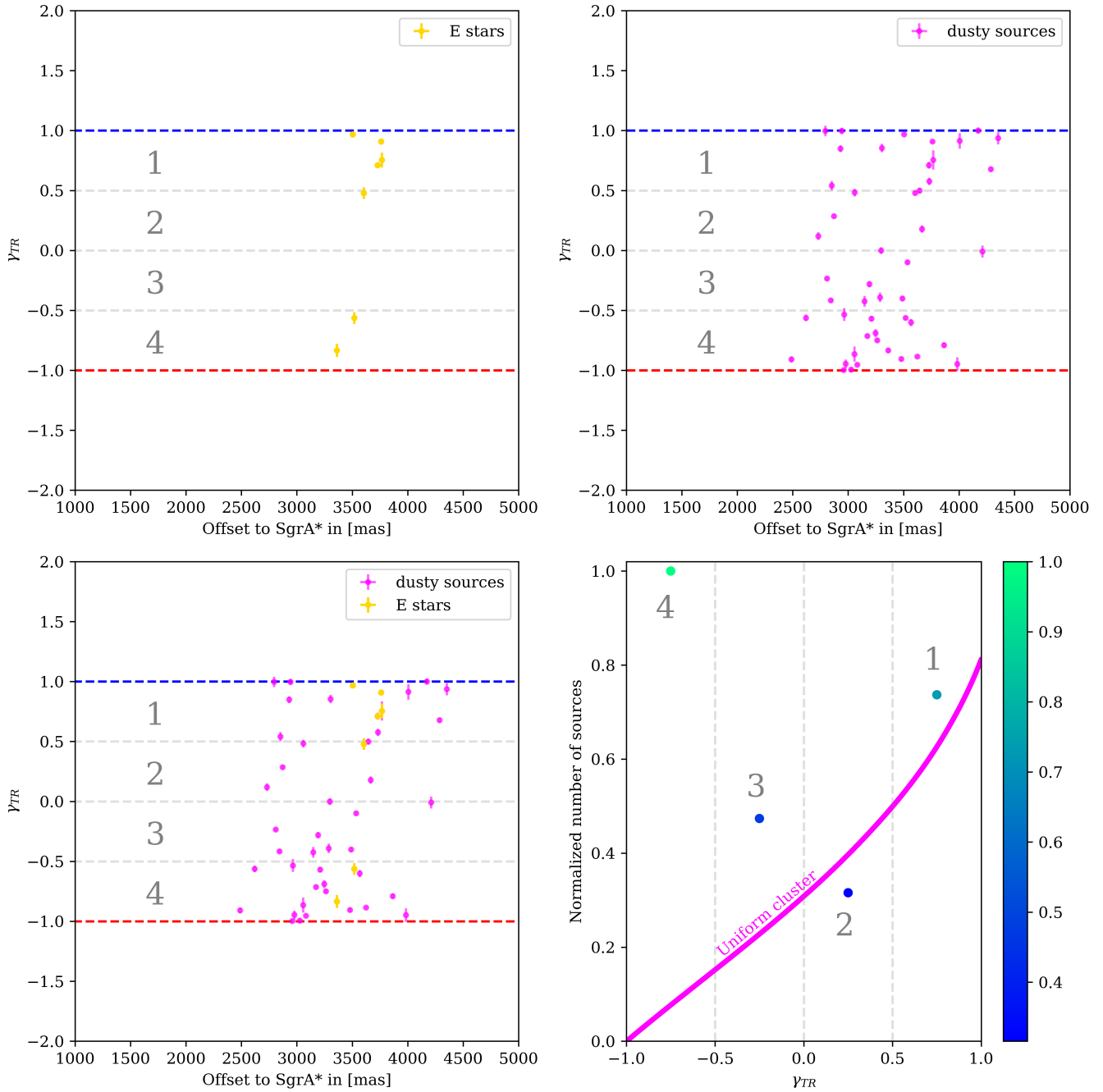


**Figure 6.** Anisotropy parameter  $\gamma_{TR}$  for the investigated sources in IRS 13. In the upper row, we illustrate  $\gamma_{TR}$  for the E-stars (left) and the dusty sources (r). Dividing the anisotropy parameter into four bins reveals an overdensity for some of the sources close to  $\gamma_{TR} \approx \pm 1$  implying the existence of substructures. In the lower-left plot, we show all investigated sources of the IRS 13 cluster. The uncertainties of the anisotropy parameters are determined with error propagation of the related standard deviation of the proper motion values (Appendix 3.2). The grey numbers and dashed vertical lines represent the related bin. The lower right plot shows the normalized number of sources for each bin as a function of  $\gamma_{TR}$ . The magenta-colored line represents the normalized theoretical probability distribution that one would expect for a uniform cluster. The comparison of the observed structure of IRS 13 with a uniform cluster suggests anomalies that are responsible for a non-uniform distribution.

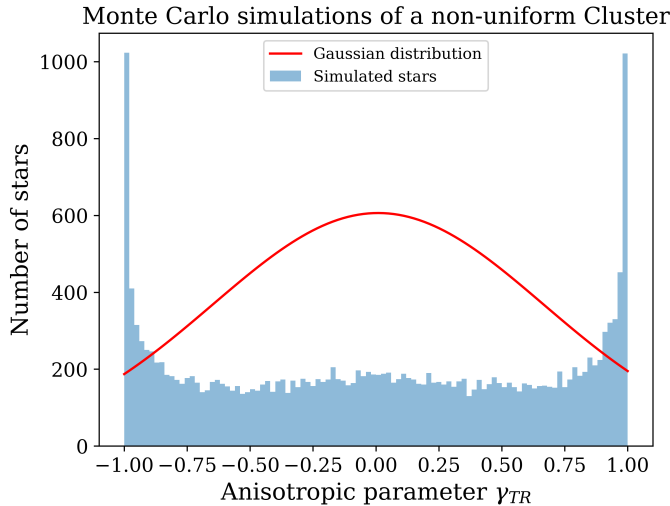


**Figure 7.** Monte Carlo simulations of  $\gamma_{TR}$  for 10000 stars. As we have shown in Fig. 6, the anisotropy parameter peaks at  $\pm 1$ , which indicates a non-uniform cluster. In comparison, we show a Gaussian distribution.

the dusty sources is not uniform. In addition, we estimate a velocity dispersion from the data listed in Table 3 and illustrated in Fig. 4 of  $128.86 \pm 0.14$  km/s for the cluster. From this we can directly derive the mass that is needed to bind the stars to the cluster. With  $M_{\text{IRS13}} = \langle v^2 \rangle \cdot R/G$  where  $R = 0.01$  pc donates the approximate size of the cluster and  $G$  the gravitational constant, we get  $\sim (3.9 \pm 0.1) \times 10^4 M_{\odot}$  in agreement with independently calculated literature values (see Schödel et al. 2005; Paumard et al. 2006; Tsuboi et al. 2017b, 2020b). This enclosed mass estimate can be used to calculate the Hill radius  $r_{\text{Hill}}$  to inspect the gravitational bounds of the IRS 13 cluster. We use

$$r_{\text{Hill}} = D(M_{\text{IRS13}}/3M_{\text{SgrA}^*})^{1/3}, \quad (7)$$

where  $D$  donates the distance to Sgr A\* and  $M_{\text{SgrA}^*}$  the related mass of the SMBH. We use  $D = 0.15$  pc and  $M_{\text{SgrA}^*} = 4 \times 10^6 M_{\odot}$  (Peißker et al. 2022; Event Horizon Telescope Collaboration et al. 2022) and get  $r_{\text{Hill}} = 0.022$  pc = 22 mpc. Since we investigate the complete IRS 13 region, including the E-stars and the dusty objects (Fig. 3),  $r_{\text{Hill}}$  is in remarkable agreement with the measured diameter of the cluster core region ( $\approx 45$  mpc, see Sec. 4).

### 3.3. Photometric analysis

We use a multiwavelength approach to investigate the nature of the brightest M-band dust objects in the IRS 13 cluster (Fig. 8). Starting from Fig. 8 in the M-band, we analyze the emission of the dust objects in the H-, K-, and L-band (see also Fig. 3). Since Viehmann et al.

(2006) analyzed an extensive amount of stellar sources in the environment of Sgr A\* in various bands (see also Bhat et al. 2022), we use the close-by star IRS 2L as a reference source (Table 4). Because Viehmann et al. used part of the here investigated data set, the choice of the reference star ensures a consistent photometric approach. Due to the dominant contribution of Wolf-Rayet

Filter	Magnitude [mag]	Flux $_{\lambda}$ [Jy]	A $_{\text{X}}$
H-band	14.26	0.13	4.37
K-band	10.60	0.48	2.80
L-band	6.4	2.98	1.45
M-band	5.5	3.98	0.58

**Table 4.** Derredened reference values for IRS 2L used in this work based on the analysis of Viehmann et al. (2006). The reddening vector  $A_{\text{X}}$  for the corresponding band is adapted from Viehmann (2007) assuming an optical extinction of  $A_{\text{V}} = 25$  mag (Scoville et al. 2003) using the extinction law from Rieke & Lebofsky (1985). We refer to Fritz et al. (2011) for a detailed discussion of the optical extinction  $A_{\text{V}}$ .

and O stars E1, E2, E3, and E4 (Maillard et al. 2004) in all the bands, we will use a high-pass filter to minimize the PSF wings. This process used is already described in detail in Sec. 2.4 and Peißker et al. (2022). The photometric robustness of high-pass filters compared to the raw data is further investigated in Ott et al. (1999). To inspect the validity of the proposed photometric robustness discussed in Ott et al., we compare the estimated L-band magnitudes of DS1 (Fig. 3) in the raw data with the results of the high-pass filtering. As listed in Table 5, we do not find a significant difference between the filter and non-filtered data in agreement with the analysis of Ott et al. (1999). We would like to emphasize that the analysis of the investigated dusty objects focuses on the colors defined as the difference between two magnitudes. The colors are not affected by systematic differences potentially induced by the applied high-pass filter because variations would be canceled out. However, using Eq. 1 with the magnitudes of reference star IRS2L (Table 4), we estimate the magnitudes for the dusty sources and the main-sequence stars E1-E7 (Fig. 8). Consult Table 6 for the related values, including the standard deviation.. From the H-K and K-L colors of the investigated sources, we do find a substantial difference between the two groups (dusty sources - E stars) of cluster members (Fig. 9). In addition to the sources investigated here, we also include magnitudes from the related publication of various other objects, such as DSO/G2 (Peißker et al. 2021c), X3 (Peißker et al. 2023b), and X7 (Peißker et al. 2021a). A complete list of all used sources analyzed for Fig. 9 is listed in Table 6. The findings presented in

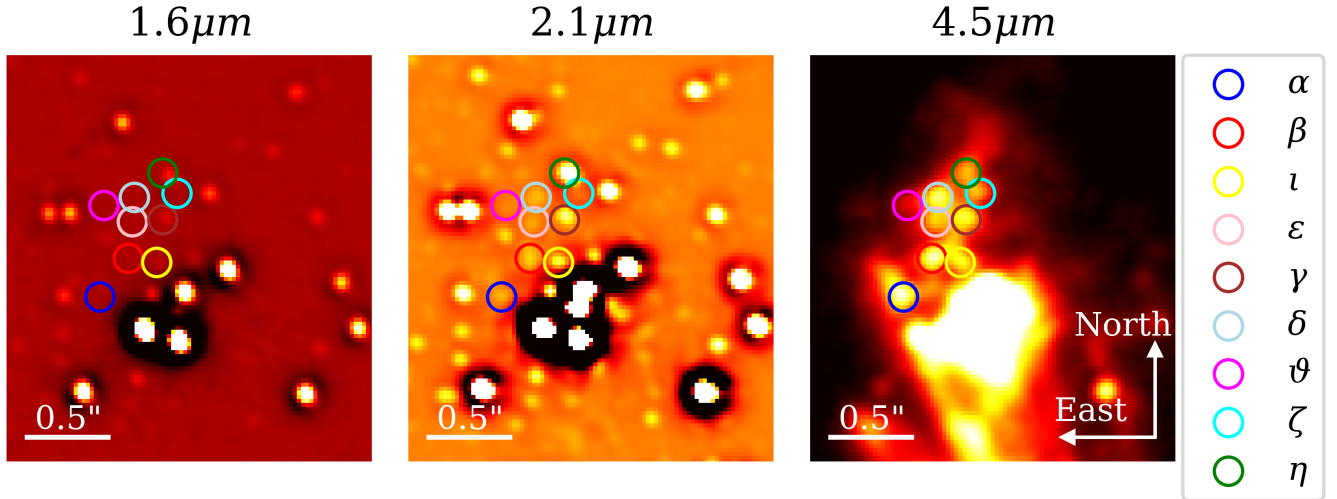


**Figure 8.** Multi-wavelength view toward IRS 13 observed with NACO. To minimize the influence of dominating PSF wings, we apply an image sharpener to the H- and K-band observed at  $1.6\ \mu\text{m}$  and  $2.1\ \mu\text{m}$ , respectively. The prominent dust features are revealed in the MIR (here:  $4.5\ \mu\text{m}$ ) and are not treated with any filter. Every image was normalized to its peak emission flux. The contrast was adjusted to visualize the presence of the dusty sources in the related band. However, the lower cutoff resulted in regions around bright stars with apparent missing flux. We note that sources such as E3 close to E4 (see Fig. 3) have an H-band emission but are suppressed due to the contrast settings.

Year	No filter	Filter	Mean	$\Delta$ Mean
2002	10.75	10.95	10.85	$\pm 0.10$
2003	10.70	10.85	10.77	$\pm 0.07$
2004	10.46	10.75	10.60	$\pm 0.15$
2005	10.50	10.68	10.59	$\pm 0.09$
2006	10.40	10.64	10.52	$\pm 0.11$
2007	10.27	10.36	10.31	$\pm 0.04$
2008	10.05	10.32	10.18	$\pm 0.13$
2009	10.13	10.34	10.23	$\pm 0.10$
2010	10.12	10.25	10.18	$\pm 0.06$
2011	9.88	10.09	9.98	$\pm 0.10$
2012	9.98	10.03	10.00	$\pm 0.02$
2013	10.09	10.21	10.15	$\pm 0.06$
2014	-	-	-	-
2015	-	-	-	-
2016	9.42	9.58	9.50	$\pm 0.08$
2017	9.88	10.19	10.03	$\pm 0.15$
2018	10.31	10.27	10.29	$\pm 0.02$
Average	10.19	10.36	10.27	0.08
Median	10.13	10.32	10.27	0.08

**Table 5.** Photometric comparison of the applied analysis tools for DS1 in the L-band. For the mean, we average the magnitude derived from the high-pass filtered and non-filtered data. The magnitude differences are marginal and smaller as the usual standard deviation as presented in Table 2.

Fig. 9 are in agreement with the studies and classifications presented in Peißker et al. (2020b) and will be

discussed in Sec. 4. Since we derived the magnitudes of the IRS 13 sources, we will estimate the related flux density and the corresponding uncertainties with Eq. 2. The flux density is useful to estimate the SED of the individual sources, which will be presented in the next section. Compared to the literature, we maximize the spectral coverage and include the radio data observed<sup>4</sup> with ALMA and previously analyzed, e.g., in Tsuboi et al. (2017b). Due to the science-ready character of the calibrated data, we list the corresponding flux values of the dusty sources in Table 7.

### 3.4. Spectral Energy Distribution

The spectral analysis of the O- and W-type stars of the IRS 13 cluster is well covered in the literature (Mailard et al. 2004). Despite bright emission in various bands, the dusty sources analyzed in the literature lack a detailed spectral analysis. We apply the 3D radiative transfer model implemented in the HYPERION code and incorporate the results listed in Table 6 and Table 7. These flux density values are used as input parameters from which HYPERION estimates the best-fit SED. The spectrum is renormalized and ensures a high synergy between the observations and the simulations. The uncertainties of the input flux density values (Table 6) estimated from the standard deviation do account for a variable background, close-by sources, and the stellar

<sup>4</sup> PI: Masato Tsuboi

ID	H-band		K-band		L-band		M-band		K-L	H-K
	[mag]	[mJy]	[mag]	[mJy]	[mag]	[Jy]	[mag]	[Jy]		
$\alpha$	20.68±0.85	0.35 <sup>+0.41</sup> <sub>-0.19</sub>	15.75±0.14	4.18 <sup>+0.57</sup> <sub>-0.50</sub>	9.48±0.30	0.17 <sup>+0.05</sup> <sub>-0.04</sub>	7.56±0.17	0.59 <sup>+0.10</sup> <sub>-0.08</sub>	6.27±0.29	4.93±0.29
$\beta$	19.74±0.04	0.83 <sup>+0.03</sup> <sub>-0.03</sub>	15.18±0.21	7.06 <sup>+1.50</sup> <sub>-1.24</sub>	8.79±0.78	0.32 <sup>+0.34</sup> <sub>-0.16</sub>	7.57±0.14	0.59 <sup>+0.08</sup> <sub>-0.07</sub>	6.39±0.29	4.56±0.13
$\gamma$	16.28±0.20	20.22 <sup>+4.09</sup> <sub>-3.40</sub>	14.19±0.30	17.58 <sup>+5.59</sup> <sub>-4.24</sub>	9.26±0.98	0.21 <sup>+0.31</sup> <sub>-0.12</sub>	7.91±0.29	0.43 <sup>+0.13</sup> <sub>-0.10</sub>	4.93±0.34	2.09±0.05
$\delta$	19.56±0.48	0.98 <sup>+0.54</sup> <sub>-0.35</sub>	15.90±0.28	3.64 <sup>+1.07</sup> <sub>-0.82</sub>	9.16±0.76	0.23 <sup>+0.23</sup> <sub>-0.11</sub>	7.70±0.17	0.52 <sup>+0.08</sup> <sub>-0.07</sub>	6.74±0.09	3.66±0.52
$\epsilon$	-	-	16.27±0.22	2.58 <sup>+0.58</sup> <sub>-0.47</sub>	9.50±1.16	0.17 <sup>+0.32</sup> <sub>-0.11</sub>	8.34±0.52	0.29 <sup>+0.17</sup> <sub>-0.11</sub>	6.77±0.69	-
$\zeta$	20.06±0.46	0.62 <sup>+0.32</sup> <sub>-0.21</sub>	16.01±0.62	3.29 <sup>+2.53</sup> <sub>-1.43</sub>	9.38±0.84	0.19 <sup>+0.22</sup> <sub>-0.10</sub>	8.12±0.29	0.35 <sup>+0.10</sup> <sub>-0.08</sub>	6.63±0.11	4.05±0.09
$\eta$	15.29±0.16	50.34 <sup>+7.99</sup> <sub>-6.89</sub>	12.80±0.19	63.27 <sup>+12.10</sup> <sub>-10.15</sub>	9.25±0.71	0.21 <sup>+0.19</sup> <sub>-0.10</sub>	8.11±0.23	0.35 <sup>+0.08</sup> <sub>-0.06</sub>	3.55±0.26	2.49±0.02
$\vartheta$	21.04±0.25	0.25 <sup>+0.06</sup> <sub>-0.05</sub>	-	-	10.29±1.22	0.08 <sup>+0.17</sup> <sub>-0.05</sub>	9.14±0.39	0.13 <sup>+0.06</sup> <sub>-0.04</sub>	-	-
$\iota$	16.67±0.21	14.12 <sup>+3.01</sup> <sub>-2.48</sub>	14.23±0.29	16.95 <sup>+5.19</sup> <sub>-3.97</sub>	9.71±1.62	0.14 <sup>+0.48</sup> <sub>-0.10</sub>	8.12±0.45	0.35 <sup>+0.18</sup> <sub>-0.12</sub>	4.52±0.66	2.44±0.25
	[mag]	[Jy]	[mag]	[Jy]	[mag]	[Jy]	[mag]	[Jy]		
E1	11.16±0.06	2.25 <sup>+0.12</sup> <sub>-0.12</sub>	9.19±0.17	1.75 <sup>+0.29</sup> <sub>-0.25</sub>	7.69±0.65	0.90 <sup>+0.74</sup> <sub>-0.40</sub>	6.96±0.33	1.03 <sup>+0.36</sup> <sub>-0.27</sub>	1.50±0.23	1.97±0.03
E2	11.31±0.08	1.96 <sup>+0.15</sup> <sub>-0.13</sub>	9.23±0.21	1.69 <sup>+0.36</sup> <sub>-0.29</sub>	7.07±0.64	1.60 <sup>+1.29</sup> <sub>-0.71</sub>	6.17±0.27	2.14 <sup>+0.60</sup> <sub>-0.47</sub>	2.16±0.21	2.08±0.02
E3	14.43±0.59	0.11 <sup>+0.08</sup> <sub>-0.04</sub>	10.79±0.67	2.66 <sup>+0.34</sup> <sub>-0.18</sub>	6.52±0.51	2.66 <sup>+1.59</sup> <sub>-1.00</sub>	5.17±0.01	5.39 <sup>+0.04</sup> <sub>-0.04</sub>	4.27±0.08	3.64±0.26
E4	12.62±0.15	0.58 <sup>+0.08</sup> <sub>-0.07</sub>	10.25±0.33	1.45 <sup>+0.23</sup> <sub>-0.17</sub>	7.18±0.65	1.45 <sup>+1.19</sup> <sub>-0.65</sub>	6.15±0.15	2.18 <sup>+0.32</sup> <sub>-0.28</sub>	2.77±0.31	2.37±0.08
E5.0	-	-	14.24±0.41	0.65 <sup>+0.01</sup> <sub>-0.01</sub>	8.04±0.99	0.65 <sup>+0.97</sup> <sub>-0.39</sub>	6.68±0.31	1.34 <sup>+0.44</sup> <sub>-0.33</sub>	6.20±0.70	-
E5.1	-	-	14.53±0.09	0.61 <sup>+0.01</sup> <sub>-0.01</sub>	8.11±0.87	0.61 <sup>+0.75</sup> <sub>-0.34</sub>	6.95±0.29	1.04 <sup>+0.32</sup> <sub>-0.24</sub>	6.42±0.48	-
E7	13.21±0.11	0.54 <sup>+0.02</sup> <sub>-0.02</sub>	10.61±0.11	0.32 <sup>+0.05</sup> <sub>-0.04</sub>	8.82±0.71	0.32 <sup>+0.29</sup> <sub>-0.15</sub>	8.92±0.85	0.17 <sup>+0.20</sup> <sub>-0.09</sub>	1.79±0.29	2.60±0.05
	[mag]	[Jy]	[mag]	[Jy]	[mag]	[Jy]	[mag]	[Jy]		
IRS3	14.68 ± 0.12	0.08 <sup>+0.02</sup> <sub>-0.01</sub>	9.66 ± 0.62	1.14 <sup>+0.88</sup> <sub>-0.49</sub>	6.03±0.03	4.19 <sup>+0.11</sup> <sub>-0.12</sub>	2.99 ± 0.14	40.16 <sup>+5.53</sup> <sub>-4.86</sub>	3.63±0.32	5.02±0.35
IRS7	9.26 ± 0.04	13.12 <sup>+0.36</sup> <sub>-0.60</sub>	6.50 ± 0.10	20.95 <sup>+2.02</sup> <sub>-1.85</sub>	6.01±0.05	4.26 <sup>+0.20</sup> <sub>-0.19</sub>	3.12 ± 0.49	35.63 <sup>+20.33</sup> <sub>-11.94</sub>	0.49±0.08	2.76±0.07

**Table 6.** Dereddened magnitude and flux estimates of the E-stars and the brightest dusty sources of the IRS 13 cluster (see Fig. 3). For comparison, we also list the measured values of IRS3 and IRS7. The indicated uncertainties of the magnitudes and fluxes for all objects are based on the standard deviation except for IRS3 and IRS7. The uncertainties for the two bright stars are adapted from published studies, namely Blum et al. (1996), Viehmann et al. (2006), and Pott et al. (2008). The used reference magnitudes for IRS 2L are listed in Table 4. For  $\epsilon$ , E5.0, and E5.1, we do not find H-band emission above the detection limit, which might be due to confusion. The uncertainties of the magnitudes and fluxes reflect the standard deviation. As pointed out by Fritz et al. (2010) and implied by the east-west elongation indicated in Eckart et al. (2004), E3 may be a collection of several less luminous stars. Controversially, Tsuboi et al. (2017b) associates E3 with the location of a possible IMBH.

density as well as the embedded structure (eminent in the L- and M-band) of the cluster.

To motivate the usage of HYPERION, which models the emission of YSOs, we refer to the color-color diagram shown in Fig. 9, which justifies our approach. Incorporating the derived flux and uncertainty values, we find a best-fit solution for the spectral energy distribution of the dusty sources, as shown in Fig. 11. We list related input parameters, such as, for example, stellar mass and luminosity, in Table 8. In agreement with the top-heavy mass function derived by Paumard et al. (2006) or Lu et al. (2013), we find several massive and high-mass YSOs in the IRS 13 cluster, in line with its exceptional high core density of  $\rho_{\text{core}} \geq 3 \times 10^8 M_{\odot} \text{pc}^{-3}$  (Paumard et al. 2006). Except for  $\eta$ , all investigated sources exhibit a stellar mass between 4.0 and 10.0  $M_{\odot}$ . Taking into account the stellar properties of the dusty sources in combination with the accretion rate (denoted as the infall rate in Table 8), we classify these objects as massive Herbig Ae/Be stars. Due to their nature, these dusty sources have an age of  $10^4 - 10^5$  yr and show a

strong photometric correlation (Fig. 9) with the recent discovery of the HMYSO X3 (Peifker et al. 2023b). Regarding  $\eta$ , more data is needed to classify the low-mass source. However, the shape of the related SED implies that  $\eta$  could be associated with a low-mass T Tauri star (Beckwith et al. 1990; Kenyon & Hartmann 1995).

## 4. DISCUSSION

In this Section, we will discuss the results presented above. We will introduce a new substructure of the IRS 13 cluster and motivate detailed upcoming observations in the mid-infrared. Taking into account the results presented, we will further suggest expanding the existing view towards the dimension of the IRS 13 cluster. It is suggested that the cluster shows an elongated tail that is caused by the gravitational interaction of Sgr A\* with IRS 13.

### 4.1. Stellar content of the system

NACO L-band observations of IRS 13 revealed 33 unknown objects in addition to previously investigated

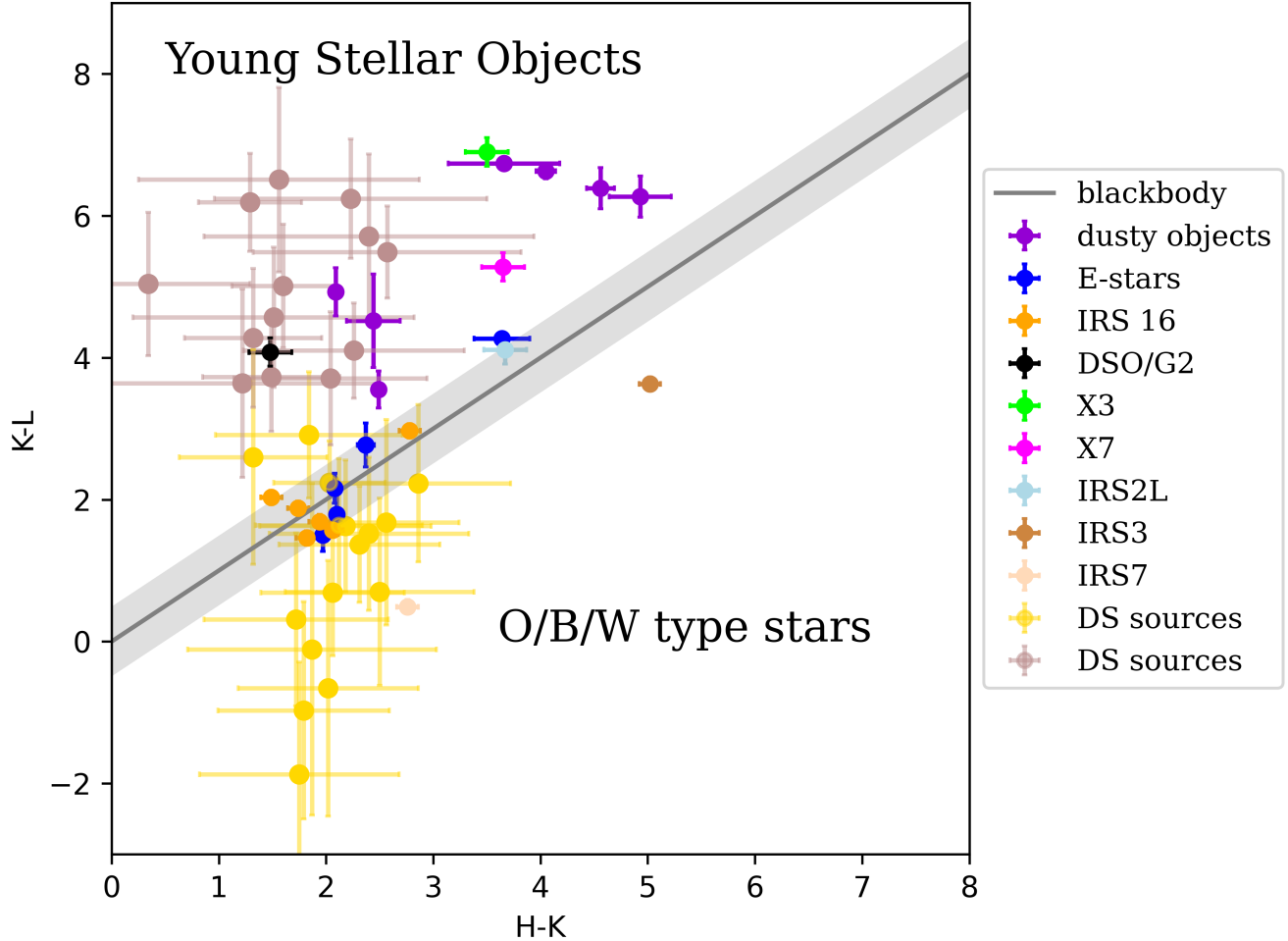


**Figure 9.** Color-color diagram for some prominent stellar objects in the *inner parsec*. The linear gray line represents a one-component black body with increasing temperature and separates known evolved and embedded early-type stars from candidate YSOs (see also Ishii et al. 1998; Eckart et al. 2004). Based on this classification, the photometric data implies two generations of dusty sources, namely YSOs (brown) and main-sequence stars (yellow). Please note that the photometric uncertainty of two DS sources, DS23 and DS30, forbids a strong statement about their exact nature. Overall, the uncertainties represent the standard deviation of the estimated colors listed in Table 6. Here, IRS 16 refers to the stars indicated in Fig. 3.

dust and stellar sources (Table 13; see Maillard et al. 2004; Eckart et al. 2013). The brightest sources, denoted with greek letters, can be observed in various bands ranging from the infrared to the radio/submm domain. Since the majority of the studied MIR dust sources exhibit K- and H-band NIR counterparts (see Appendix D and Appendix E), a stellar nature is inevitable. Compared to the main-sequence E-stars (O/WR-type), the K-L and H-K colors of the dusty sources are represented by two to three times higher numerical values. These high infrared H-K and K-L colors suggest, together with the survey of Ishii et al. (1998), a YSO classification for the bright dusty objects of IRS 13. Further studies of YSOs were carried out by Lada & Adams (1992), who used J-H and H-K colors for their classification. Al-

though the geometrical composition of the circumstellar components influences the NIR emission of YSOs, our derived H-K colors are in agreement with studies of intermediate and high-mass YSOs (see also Berrilli et al. 1992). A further indicator that underlines the classification of the dusty sources as YSOs is illustrated in Fig. 11. The flux density values, covering a spectral range between the IR and the submm/radio, are fitted with a model representing the typical emission of Class I YSOs. Why the best-fit models presented in Fig. 11 do not necessarily exclude other interpretations of the flux density distribution of the dusty sources, it is still a strong footprint of YSOs. Observations with the JWST and MIRI will potentially reveal typical emission lines that are associated with YSOs (see Sec. 4.6). We note that there

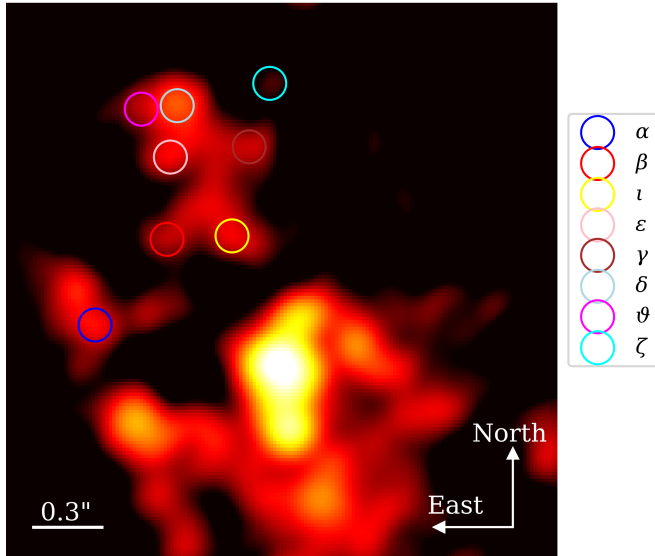


**Figure 10.** Observation of the IRS 13 cluster with ALMA. The data was observed at 343 GHz and corresponds to CO ( $v=0$ ). The location of the bright dusty sources that are observed in the infrared is indicated by colored circles. Like the E-stars, the projected location of the dusty sources implies clustering. The related flux of the individual sources is listed in Table 7.

ID	CO ( $v=0$ ), 343 GHz [mJy]
$\alpha$	$1.43 \pm 0.5$
$\beta$	$1.05 \pm 0.5$
$\gamma$	$1.09 \pm 0.5$
$\delta$	$1.91 \pm 0.5$
$\epsilon$	$1.38 \pm 0.5$
$\zeta$	$0.61 \pm 0.5$
$\eta$	$(0.19 \pm 0.5)^*$
$\vartheta$	$(1.15 \pm 0.5)^{**}$
$\iota$	$1.29 \pm 0.5$
IRS3	$129.1 \pm 55.1$
IRS7	$34.4 \pm 0.4$

**Table 7.** Flux density values for the dusty objects derived from CO ALMA observations. Please see Fig. 10 for the related source identification. For  $\eta$ , we only estimate an upper limit, whereas  $\vartheta$  seems to be confused with  $\delta$ . We use IRS 13E3 as a reference source with a corresponding peak flux of  $10.5 \pm 0.5$  mJy and adapt the uncertainty as proposed in Tsuboi et al. (2017a). These submm/radio flux values in combination with the IR values listed in Table 6 are used for the input spectrum of HYPERION.

is increased confusion and noise level when investigating J-band NACO observations, which requires a detailed data processing method such as the Lucy-Richardson deconvolution algorithm (Lucy 1974). However, these analysis steps exceed the scope of this work and will be part of a future publication. It should be noted that the classification of the brightest L-band sources in our sample exhibits a flux density distribution that agrees very well with class I YSOs except for  $\eta$ . The SED of this source shows similarities to a low-mass T Tauri star (Chiang & Goldreich 1997; Scoville & Burkert 2013). Hence, we will focus on the rather ambiguous classification of  $\eta$  using the J-H and H-K colors. Despite the challenges with respect to the J-band analysis of the dusty sources of IRS 13, we identify  $\eta$  without confusion about noise (Fig. 12), and infer a related magnitude of  $\text{mag}_J = 18.8 \pm 0.6$  that results in J-H = 3.5 with H-K = 2.5 (Table 6). Taking into account the color-color analysis of Lada & Adams (1992), Ito et al. (2008), and Ojha et al. (2009),  $\eta$  appears to be a low-mass class I YSO that conflicts with the results of the radiative transfer model presented in Sec. 3.4 due to the missing envelope. We can only speculate on possible explanations for the interplay of the missing envelope with the photometric footprint of a Class I YSO candidate. One option could be the intrinsic orientation of the system towards the observer. As implied by the SED results present in Fig. 11, the inclination does have a considerably large impact on the shape of the distribution. Another option could be an evolutionary transition to the class II stage or a partial detachment of the envelope, as is already suggested for the class I YSO L1489 IRS (Brinch et al. 2007). Despite the exact classification, the global interpretation as a low-mass YSO is still plausible. Since DSO/G2 (Peißker et al. 2021c) is also classified as a low-mass YSO (see Zajaček et al. 2017), it is implied that both sources share a common nature. In summary, the general trend suggests that sources above the solid line illustrated in Fig. 9 can be classified as YSOs, which implies that IRS 13 harbors two generations of stellar objects.

#### 4.2. Validity of the radiative transfer model

Here we want to take a critical look at the results regarding the classification of the dusty sources as YSOs. In Eckart et al. (2004), the authors proposed for the first time the idea of associating the dusty sources of IRS 13 using a color-color diagram such as the one displayed in Fig. 9. In agreement with Eckart et al. (2004) and the analysis of X3 presented in Peißker et al. (2023b), we found distinguishing colors compared to known main-sequence stars such as IRS3 (Pott et al. 2008). To ex-

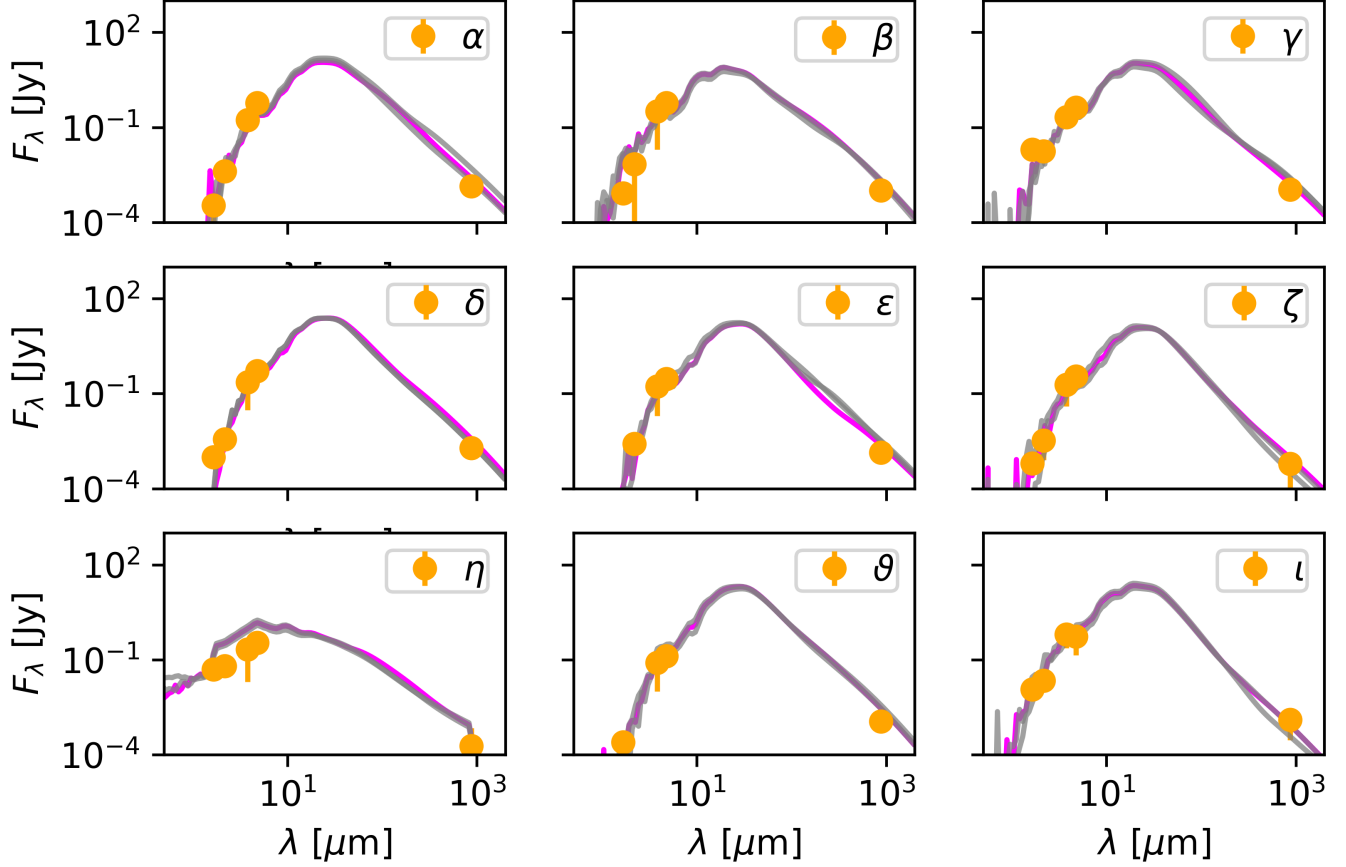


**Figure 11.** Best-fit SED of the brightest dusty sources in the IRS 13 cluster representing the YSO parameters given in Table 8. The input spectrum is constructed using the flux density values listed in Table 6 and Table 7. The associated numerical flux density values, including their related uncertainty, are implemented in the SED plots to emphasize the validity of the resulting best-fit parameters. For almost every source, the solution in magenta represents the best fit and is associated with an inclination of about  $90^\circ$ , while the gray SED is related to the maximum and minimum uncertainty indicated in Table 8. The inclination for the SED, including the related uncertainties of the source  $\eta$ , equals  $70^\circ$ .

ID	Mass [ $M_\odot$ ]	Luminosity [ $10^3 \times L_\odot$ ]	Infall rate [ $10^{-6} \times \dot{M}_\odot$ ]	Radius [ $R_\odot$ ]	Disk mass [ $M_\odot$ ]	Disk size [AU]	Envelope size [AU]
$\alpha$	$5.0 \pm 1.0$	$9 \pm 1$	$5 \pm 1$	$2 \pm 0.5$	$0.1 \pm 0.01$	0.06-200	0.09-500
$\beta$	$8.0 \pm 1.0$	$10 \pm$	$0.3 \pm 1$	$3 \pm 0.5$	$0.01 \pm 0.005$	0.04-200	0.09-350
$\gamma$	$6.0 \pm 1.0$	$9 \pm 1$	$0.3 \pm 0.1$	$4 \pm 1$	$0.05 \pm 0.01$	0.04-200	0.09-500
$\delta$	$10.0 \pm 2.0$	$11 \pm 1$	$0.5 \pm 0.1$	$3 \pm 1$	$0.01 \pm 0.001$	0.04-200	0.09-700
$\epsilon$	$7.0 \pm 2.0$	$7 \pm 2$	$0.5 \pm 0.1$	$3 \pm 2$	$0.1 \pm 0.01$	0.04-200	0.09-700
$\zeta$	$4.0 \pm 1.0$	$7 \pm 1$	$0.3 \pm 0.1$	$3 \pm 1$	$0.06 \pm 0.01$	0.04-100	0.09-500
$\eta$	$0.5 \pm 0.2$	$2 \pm 0.5$	-	$0.8 \pm 0.2$	$0.005 \pm 0.002$	0.13-50	-
$\vartheta$	$7.0 \pm 1.5$	$8 \pm 1$	$0.5 \pm 0.1$	$3 \pm 1$	$0.01 \pm 0.02$	0.04-200	0.04-700
$\iota$	$10 \pm 2.0$	$12 \pm 2$	$0.05 \pm 0.01$	$7 \pm 2$	$0.5 \pm 0.1$	0.02-100	0.04-700

**Table 8.** Best fit parameters describing the flux density distribution of the dusty sources of IRS 13 indicating their stellar nature using the radiative transfer model HYPERION. We motivate the application of the radiative transfer model describing YSOs by the clear color-color classification shown in Fig. 9. Considering the pronounced slope of the NIR/MIR SED and their related position in the color-color diagram, it is suggested that the nature of these sources allows the classification as candidates YSOs (class I) (Lada 1987). For a demonstration of HYPERION's feedback after incorporating the estimated flux density values for IRS 3, please refer to Section 4.2.



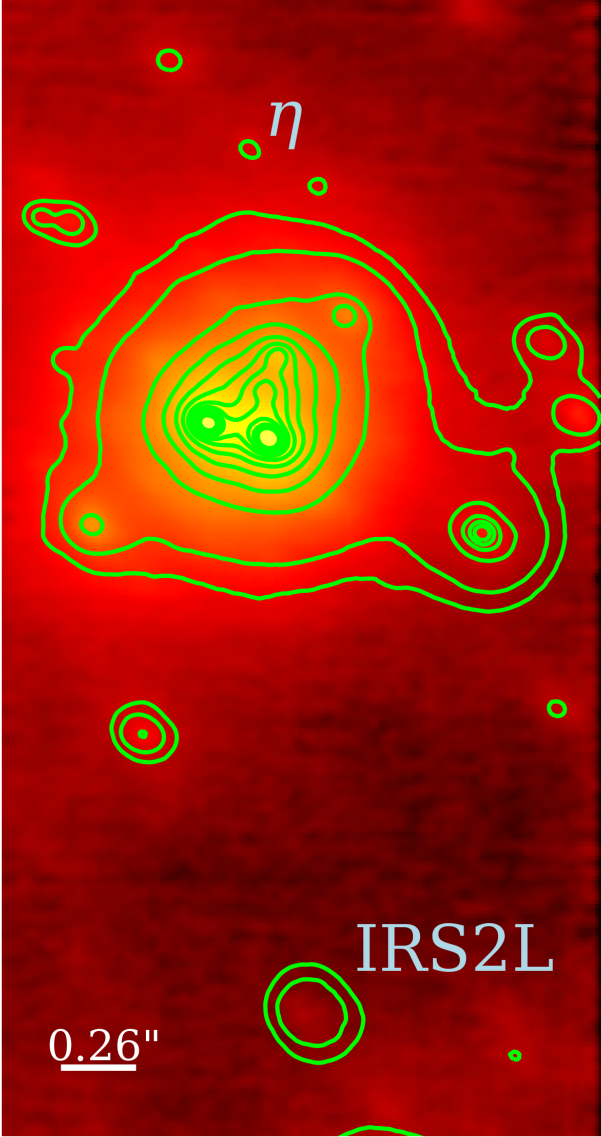


**Figure 12.** J-band observation of IRS 13 with NACO in 2013. We overlaid lime-colored contour lines adopted from the K-band observations of the same epoch and instrument. The contour levels represent 0.75%, 1%, 2%, 3%, 4%, 5%, 6%, 7%, 8%, 9%, and 10% of the normalized K-band NACO data. The faint emission of IRS2L is labeled at the corresponding K- and L-band position whereas the bright emission is associated with IRS 13. We further indicate the position of the low-mass class I YSO  $\eta$ . Here, North is up, East is to the left.

pand the color-color analysis of the dusty sources, we decided to apply the radiative transfer code HYPERION (Robitaille 2011, 2017) to the flux density values listed in Table 6. Although we find satisfying solutions to the flux density values in combination with the colors of the dusty sources (Fig. 11), the outcome of the ra-

diative transfer model could be biased since we already assumed a YSO classification. Therefore, we want to investigate the validity of this approach by using the class I model used for the SED shown in Fig. 11 with the flux density values of the embedded and cool carbon star IRS 3. This star is most probably in the helium-core burning phase with a related stellar temperature of 3000 K based on the interferometric observations carried out with MIDI/VLTI (Leinert et al. 2003; Pott et al. 2008). For the stellar analysis of IRS3 presented in Pott et al., the authors used the one-dimensional radiative transfer code DUSTY (Ivezic et al. 1999), which is developed for AGB stars exhibiting radiatively driven winds. The NIR and MIR flux density values for IRS3 listed in Table 6 are in reasonable agreement with the results presented in Figure 16 in Pott et al. (2008). Deviations between our estimated flux values and the ones derived by Pott et al. are reflected by the uncertainties given in Table 6 and the error bars shown in Fig. 13. Using the estimated stellar properties of Pott et al. (2008) results in the magenta-colored SED displayed in Fig. 13. Comparing the magenta-colored result with the measured flux density of IRS3 reveals that HYPERION is not suitable to reflect the SED of the star. Using the upper limit of Pott et al. for a hot C-rich star with an amorphous carbon grain-dominated circumstellar dust distribution produces the brown-colored SED shown in Fig. 13. In

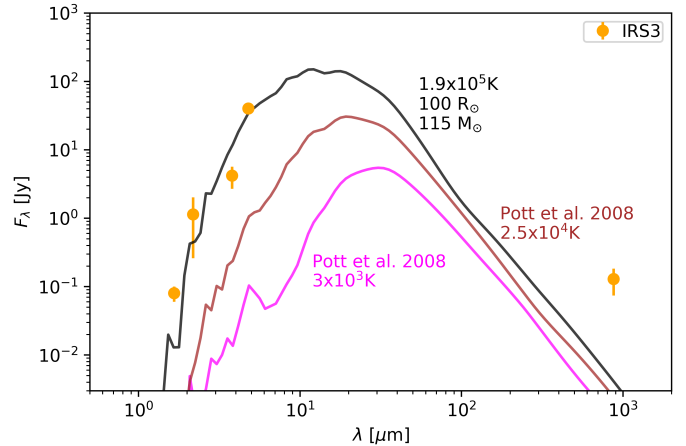


**Figure 13.** Comparison of different input parameters for the flux density values (orange colored dots) estimated for IRS3 (Table 6). Please note that the magenta and brown-colored SED is based on the stellar parameters derived by the interferometric broadband analysis by Pott et al. (2008). Assuming a hypothetical YSO association with IRS3 results in unsatisfying outcomes of the radiative transfer model fit. Only a speculative stellar temperature of  $1.9 \times 10^5 K$  seems to reproduce the NIR and MIR flux. The submm/radio emission is not fitted by any of the presented SED solutions. Please see the text for details.

summary, the authors of Pott et al. conclude that IRS3 is a cool carbon AGB star. However, we speculatively implement a stellar temperature of  $1.9 \times 10^5 K$  in our radiative transfer model and find that this setting reflects the NIR and MIR emission. Neither of the presented SED solutions for IRS3 using HYPERION does fit the submm/radio flux. Taking into account the silicate absorption feature of IRS3 observed in the N-band (Pott et al. 2008), we can safely conclude that our speculative solution (black SED, Fig. 13) is not valid. It is further well-known that the existence of silicates requires a stellar temperature of a few 1000 K (Kozasa & Sogawa 1999; Tsuchikawa et al. 2021) in line with the established results for IRS3 of the literature. Therefore, we conclude that the SED solution displayed in Fig. 11 is a strong indication for the classification of the dusty sources as YSOs. The radiative transfer model HYPERION is not suitable for embedded main sequence stars, which emphasizes the color-color results presented in Fig. 9.

#### 4.3. Formation scenarios for the IRS13 cluster

Due to the complexity of possible formation scenarios for the IRS 13 cluster, we refer to Paper II. However, we briefly want to outline the basic idea to explain the findings presented in this work. As proposed by Wang et al. (2020)<sup>5</sup>, the resulting trajectory of the young cluster that spirals in towards the inner parsec could have resulted in the bow shock formation caused by the supersonic motion of the cluster, cluster stellar wind, NSC winds, and the ISM. The dense region in the bow-shock shell would then be the birthplace of the second generation of IRS 13 stars (see Table 9). We note that the S-

	1. Generation	2. Generation
Approx. age [Myr]	4	< 1
Birth place	CND	Bow-shock shell
Current location inside IRS 13	Core	Tip
Mean $K-L$ index	2.49	5.72

**Table 9.** Generation of stars inside the IRS 13 cluster with their related origin and current location. In addition, we list the mean  $K-L$  color of the sources listed in Table 6. We exclude E5.0 and E5.1 from the mean colors due to their missing H-band counterpart, which may be related to confusion or their nature. The majority of the sources considered in this list can be categorized as high-mass objects. See Fig. 14 for the location of the sources.

cluster (Eckart & Genzel 1996) exhibits a similar compo-

sition of stellar objects as listed in Table 9 (Habibi et al. 2017; Peißker et al. 2020b; Ciurlo et al. 2020; Peißker et al. 2021c, 2023a). However, one would naturally expect a certain degree of elongation for an extended structure that gravitationally interacts with an SMBH such as Sgr A\* (see simulations of Hobbs & Nayakshin 2009; Jalali et al. 2014). While the dimensions and nature of IRS 13 will be the focus of Paper II, we want to note that the [FeIII] emission of the cluster implies a larger structure as it is known from the literature. Considering the forbidden [FeIII] line distribution presented in Lutz et al. (1993), we find that the peak emission of the iron line clearly envelopes the IRS 13 and the IRS 2 region suggesting a combined setup of the northern and southern cluster region (see Fig. 14). It is already known that IRS 2C is a foreground star while IRS 2L and IRS 2S are embedded in the dust feature which is associated with IRS 13 (Buchholz et al. 2013). However, our proposed interpretation of the dimensions of the cluster is in line with the polarization measurements of Buchholz et al. (2013) and Roche et al. (2018). The polarimetric and magnetic field line analysis of Roche et al. reveals that the dust feature, which envelopes IRS 13 and IRS 2L/2C, is a coherent structure. The line distribution of [FeIII] but also the MIR dust emission matches the size of the polarization region of IRS 13 in Buchholz et al. (2013) and Roche et al. (2018) underlying the proposed dimensions of the cluster in this work. In Paper II, we will present N-body simulations of an inspiralling cluster towards the inner parsec and investigate the possibility of such an event.

#### 4.4. IRS 13 and the (counter-)clockwise disk

As we have shown in Fig. 6, the investigated cluster member sample shows a non-uniform distribution. In addition, most of the stars in the NSC follow this non-isotropic kinematic pattern, which historically resulted in the finding of a counter- and clockwise disk, abbreviated as CCWS and CWS, respectively (Genzel et al. 1996; Paumard et al. 2006). The mentioned velocity pattern is characterized by the normalized angular momentum  $j$ , which is defined by Genzel et al. (2003) as

$$j = (xv_y - yv_x)/pv_p \quad (8)$$

where  $x$ ,  $v_x$ ,  $y$ ,  $v_y$  refer to RA and DEC coordinates and their related components of proper motion, respectively, while the total distance and proper motion are given by  $p$  and  $v_p$ . With the above equation and the numerical values given in Table 3, we find the same distribution (Fig. 15) for IRS 13 sources as shown in Paumard et al. (2006). In analogy to the anisotropy parameter shown in Fig. 6, we divide the data presented in Fig. 15 into four

<sup>5</sup> See their Fig. 10.

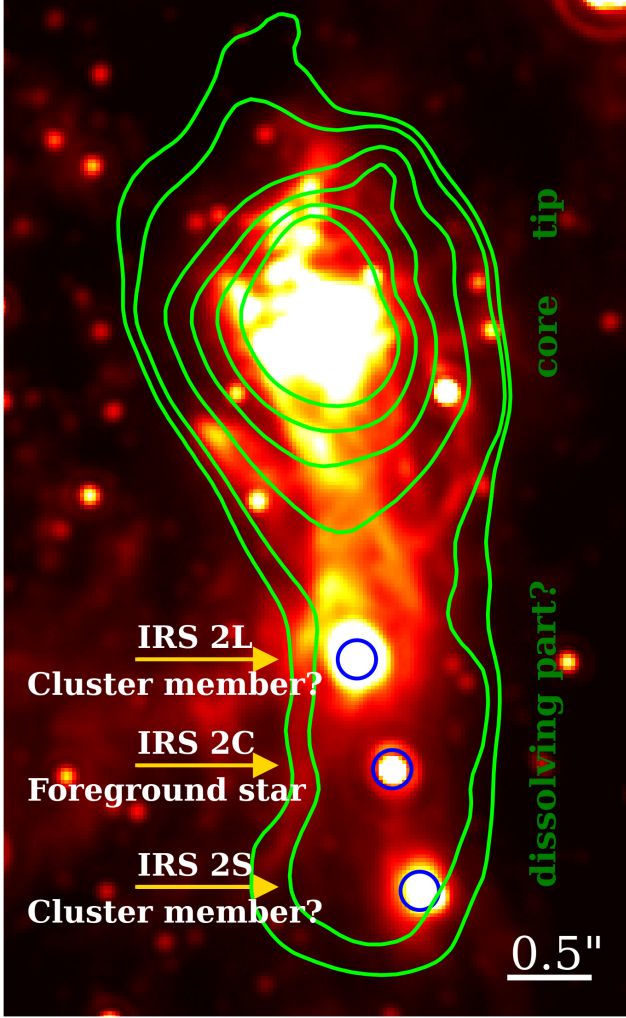


**Figure 14.** L-band NACO observation of IRS 13 in 2004 overlaid with [FeIII]  $2.218 \mu\text{m } ^3G_5 \rightarrow ^3H_6$  contour lines extracted from a SINFONI 3d data cube. The contour lines represent the 26%, 30%, 40%, 50%, 60%, and 70% level whereas the peak emission is at  $2.5 \times 10^{-10} \text{ergs}^{-1} \text{cm}^{-2} \mu\text{m}^{-1}$ . The 70% contour line centered on the core region of IRS 13 resembles the projected size of the Hill radius ( $\approx 22 \text{mpc}$ ) estimated with Eq. 7 in Sec. 3.2. In addition, the 30% contour lines enclose the southern region with respect to the core and tip components of the IRS 13 cluster. As indicated, we mark the two embedded sources IRS2L and IRS2S that might be former members of the core region of IRS 13. The compact source IRS2C is also known as AF/AHH (Allen et al. 1990; Blum et al. 1996) and could be a foreground star based on the polarimetric analysis of Buchholz et al. (2013).

bins. We estimate that the bin with  $j \in \{0.5, 1.0\}$  contains 22% of the sources, for  $j \in \{0.0, 0.5\}$ , we get 8%, for  $j \in \{0.0, -0.5\}$ , there are 10% of the sources, and finally for  $j \in \{-0.5, -1.0\}$  we obtain 60%. Therefore,

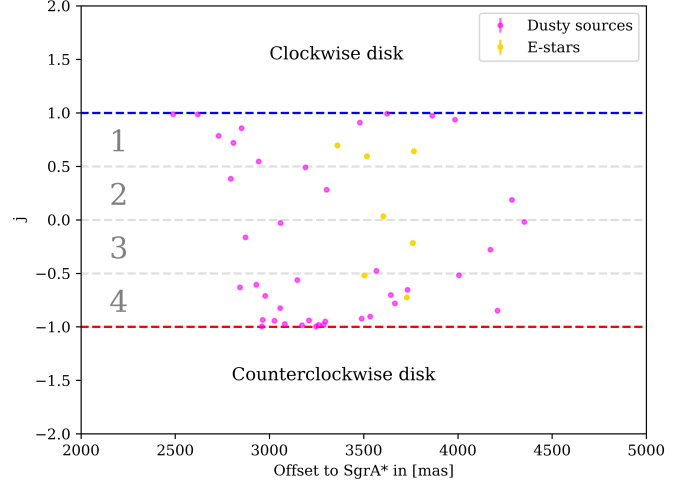


**Figure 15.** Normalized angular momentum  $j$  as a function of distance from Sgr A\* for all the here investigated IRS 13 cluster members. We find a stellar distribution similar to the one derived by Paumard et al. (2006) for the majority of the NSC stars (see also von Fellenberg et al. 2022). Here, most of the investigated objects peak at  $j=-1$ , suggesting a CCW disk membership. Magenta circles represent the dusty sources analyzed in this work, the gold-filled ones indicate the E-stars (Fig. 3). The size of the individual data points covers up the uncertainties calculated with error propagation.

we find an overdensity in bin 4, which strengthen our result presented in Fig. 6. Since a non-uniform cluster is supposed to peak at  $\gamma_{TR} = \pm 1$  as shown in Fig. 7<sup>6</sup>, it is expected to find anisotropic structures in the angular momentum plot displayed in Fig. 15. For our sample, we clearly identify an overdensity at  $j = -1$  (Fig. 15) suggesting a CCW disk membership (Paumard et al. 2006; Ali et al. 2020; von Fellenberg et al. 2022). Based on this finding, we propose three different scenarios:

- [a ] The (C)CWS characterization of stars in the *inner parsec* is valid for all (gravitationally bound) sub-regions,
- [b ] The stellar overdensity of the IRS 13 cluster is the result of the intercepting disks of the CCW and CW systems,
- [c ] The IRS 13 cluster shows the imprint of the CCW and CW systems.

Concerning [a], we want to highlight the theoretical work of Hobbs & Nayakshin (2009), who predict two warped stellar discs/distributions for infalling molecular clouds.

<sup>6</sup> In addition, Genzel et al. (2000) shows Monte Carlo simulations that demonstrate in agreement with our results that non-uniform cluster exhibits an overdensity of stars at  $\gamma_{TR} = \pm 1$ .

In addition, [Ali et al. \(2020\)](#) find a similar distribution for the S-stars, which suggests that a two-disk or even a multi-disk structure is present for other sub-regions as well, presumably those that are gravitationally bound to the SMBH or an IMBH. It needs to be verified by  $N$ -body numerical simulations how long the original disk-like stellar structure that bears imprints of the formation mechanism can survive within the NSC. As mentioned before, the results presented in [Fig. 15](#) do reveal that the majority of investigated cluster members ( $> 50\%$ ) are part of at least one disk, presumably the CCW disk. In addition, [Paumard et al. \(2006\)](#) suggested that the IRS 13 cluster may result from the interaction of the CCW and CW disks, i.e. scenario [b]. Although this scenario cannot be excluded, it implies an underlining rotation pattern that may have been created by infalling clouds in the first place (see [a] and [Hobbs & Nayakshin, 2009](#)). Since the E-stars seem to be members of both distributions ([Fig. 6](#), upper left plot), the scenario seems plausible. However, we will investigate this particular point in more detail in Paper II because it would exceed the scope of this work. For the last scenario [c], the IRS 13 cluster serves as a tracer for the underlining disk pattern. The infalling cluster IRS 13 may have intercepted the CCW and CW disks, which led to compressed gas densities that triggered star formation. Likewise, for [b], we will focus on this point in Paper II. Independent of the exact relation between IRS 13 and the (C)CW disks, we want to stress that [Hansen & Milosavljević \(2003\)](#) demanded a second black hole of  $\approx 10^4 M_\odot$  in order to explain the unusually young age of the S-cluster stars ([Morris 1993](#); [Ghez et al. 2003](#); [Habibi et al. 2017](#)). The mass estimate is in the same order as the estimated enclosed mass for IRS 13 of  $3.9 \times 10^4 M_\odot$ . Due to the age of the S-cluster members, IRS 13 is most certainly not a suitable candidate for process explaining the presence of young stars close to Sgr A\*. But it is an interesting scientific question to explore and maybe even link possible large-scale imprints on molecular clouds in the CNB from the enclosed mass of the IRS 13 cluster.

#### 4.5. Multiplicity fraction of the IRS13 cluster

Considering the young age of the IRS13 cluster members, we should have detected an increased multiplicity and companion fraction ([Portegies Zwart et al. 2010](#)). Surprisingly, only one binary system close to IRS13 is known ([Pfuhl et al. 2014](#)) which might not be related to the cluster in the first place. Taking into account the important role of binaries, especially for the evolution of massive stars ([Sana et al. 2012](#)), we expect frequent updates on the detection of binary systems in the IRS13 cluster, particularly with the upcoming Extremely Large

Telescope (ELT).

For example, [Gautam et al. \(2019\)](#) identified more than a dozen possible periodic systems. Due to resolution limitations, observation of visual binaries remains unlikely, damping the number of methods to detect such systems. Therefore, high-cadence observations with the scientific goal of identifying magnitude or LOS variations will remain the sufficient approach for multiplicity analysis.

However, given the number of sources investigated in this work, we speculatively expect at least one binary system among the sample. From the analysis, we observed minor position fluctuations of  $\gamma$  and  $\zeta$ . These uncertainties may result from a confusion problem due to the high source density ([Paumard et al. 2006](#)).

Assuming that the above-mentioned uncertainties cannot be explained by source confusion, we will use the definition of [Reipurth & Zinnecker \(1993\)](#) and [Duchêne et al. \(2001\)](#) for the multiplicity fraction (MF) and the related companion fraction (CF). Consequently, MF is defined as

$$\text{MF} = \frac{\text{B} + \text{T} + \text{Q} + \dots}{\text{S} + \text{B} + \text{T} + \text{Q} + \dots} \quad (9)$$

where S defines the number of single stars and B is the number of binary star systems. Triple and quadruple star systems are defined by T and Q letters in the above equation. In addition, CF can be written as

$$\text{CF} = \frac{2\text{B} + 3\text{T} + 4\text{Q} + \dots}{\text{S} + 2\text{B} + 3\text{T} + 4\text{Q} + \dots} \quad (10)$$

and defines the ratio of stars with a companion. For simplicity, we assume that  $\gamma$  and  $\zeta$  are two binary systems. In total, we derived seven orbital solutions for the brightest sources of the sample. These boundary conditions are translated to  $\text{MF} \sim 28\%$  and  $\text{CF} \sim 44\%$  using [Eq. 9](#) and [Eq. 10](#), respectively. If we assume a rough cluster age of  $4 \pm 1$  Myr based on the most evolved E-stars ([Maillard et al. 2004](#); [Paumard et al. 2006](#); [Zhu et al. 2020](#)), we find similar MF and CF values in other clusters with a comparable age, such as RCW 108 ([Comerón et al. 2005](#); [Comerón & Schneider 2007](#)) or the SMC cluster NGC 330 ([Bodensteiner et al. 2021](#)). If these numbers hold, it would demonstrate comparable star formation channels between different (galactic) clusters. We want to note that we assumed for the above discussion the presence of two unconfirmed binaries. However, we anticipate multiple opportunities for upcoming instruments and observation campaigns covering the IRS 13 cluster.

#### 4.6. Observations with the James Webb Space Telescope

Despite strong indications for the nature of the dusty objects, the data lack detailed spectroscopic analysis. For YSOs of type I, we would typically use tracers such as  $H_2$  (Glassgold et al. 2004),  $H_2O$  (Gibb et al. 2000), and HCN (Lahuis et al. 2006) to confirm the classification. Considering the recent start of the scientific operations of the James Webb Space Telescope, the upcoming GTO observations<sup>7</sup> of the GC will minimize the uncertainties of the YSO classification for the dusty sources. We note that there is publicly available archive<sup>8</sup> data ob-

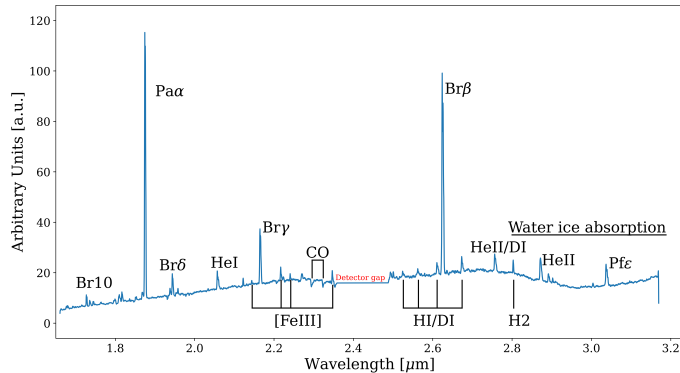


**Figure 16.** NIRSPEC spectrum of the inner parsec observed with the James Webb Space Telescope in 2022 (PI: Jessica Lu, Proposal ID: 1939). The NIRSPEC observation agrees with the water ice identification by, e.g., Moulta et al. (2015). Around  $2.4\mu\text{m}$ , the detector gap of NIRSPEC is marked.

served with NIRSPEC in 2023. Consequently, we used this dataset to inspect the spectral NIR emission and parts of the  $L$ -band (MIR) for the presence of individual line tracers. Due to the absence of telluric emission/absorption lines, we find an unaffected  $\text{Pa}\alpha$  line but also strong water absorption features (Moulta et al. 2015). With a nominal resolution power of  $\sim 2700$  with the G235H/F170LP setting, we identify several single emission and absorption lines (e.g.,  $\text{Br}\delta$ , HeI,  $\text{Br}\gamma$ , and CO band heads) in the  $H + K$ -band that are well known from SINFONI observations of the same region (PeiBker et al. 2020c, 2021a, 2023b). Considering the recent identification of snowlines in the spectrum of HH 48 NE, we expect similar findings in the GC with NIRSPEC in addition to YSO tracers that could potentially be identified with MIRI. Although the spatial  $L$ -band resolution of NACO and MIRI (JWST) is sufficiently comparable, a stable PSF and longer on-source integration times could result into new insights into the IRS13 cluster. With

the demonstrated capabilities of the JWST (Fig. 16), we will search for tracers associated with YSOs (PeiBker et al. 2023b). Since some dusty sources are close to the E-stars, we aim to increase the number of cluster samples to verify our findings on the warped disk structure of IRS 13. In addition to the continuum detections presented in this work, we expect an increase in the number of line-emitting sources such as G2/DSO (PeiBker et al. 2021c) observed with the MIRI and NIRSPEC IFU data.

## 5. CONCLUSIONS

We analyzed the IRS 13 cluster that resides at a projected distance of  $\sim 0.15$  pc from Sgr A\*. Based on the here presented work, we found a significantly higher number of cluster members of IRS 13 compared to previous studies. Using multi-wavelength observations resulting in a comprehensive color-color diagram classification, we applied a ray-tracing radiative transfer model to investigate the nature of the brightest dusty sources and found compelling evidence that points towards a YSO characterization. The DS sources share a comparable footprint with the bright dusty sources suggesting a YSO classification. In the following, we list our key findings:

- The nature of the dusty objects can be described as MYSOs and HMYSOs in agreement with the classification of X3a,
- Despite the low-mass YSO  $\eta$ , we classify all other investigated bright dusty sources as massive class I YSOs,
- The majority of investigated sources in this work are arranged in a significant disk structure, presumably the CCW disk,
- This non-uniform arrangement of the IRS 13 cluster is in remarkable agreement with previous normalized angular momentum studies of the NSC,
- From the kinematics of the cluster members, we estimate a minimum mass of  $4 \times 10^4 M_\odot$  that is required for a tidally stable system,
- The derived tidal (Hill) radius shows a strong correlation with the dimensions of the peak emission distribution ( $\text{dust}/[\text{FeIII}]$ ) of IRS 13 (Fig. 14),
- The tidally stable core of IRS 13 harbors massive O/WR stars but also HMYSOs,
- In total, we find two generations of stellar objects that can be distinguished by their age.

<sup>7</sup> Prog. Id: GTO 1266

<sup>8</sup> Downloaded from the Barbara A. Mikulski Archive for Space Telescopes (MAST).

In the future, we expect to identify more objects as the analyzed DS objects or the bow-shock source X3 which might be associated with the IRS 13 cluster. The large-scale MIRI (JWST) and ERIS (VLT) observations providing IFU data will enhance the characterization and the related precise stellar age determination of individual sources in the IRS 13 cluster.

We thank an anonymous referee for a constructive and encouraging report that helped to improve the manuscript. This work was supported in part by the Deutsche Forschungsgemeinschaft (DFG) via the Cologne Bonn Graduate School (BCGS), the Max Planck Society through the International Max Planck Research School (IMPRS) for Astronomy and Astrophysics as well as special funds through the University of Cologne. Conditions and Impact of Star Formation is carried out within the Collaborative Research Centre 956, sub-project [A02], funded by the Deutsche Forschungsgemeinschaft (DFG) – project ID 184018867. B.Sh. acknowledges financial support from the State Agency for Research of the Spanish MCIU through the “Center of Excellence Severo Ochoa” award for the Instituto de Astrofísica de Andalucía (SEV-2017- 0709). MZ acknowledges the GAČR-LA grant No. GF23-04053L for financial support. Part of this work was supported by fruitful discussions with members of the European Union funded COST Action MP0905: Black Holes in a Violent Universe and the Czech Science Foundation (No. 21-06825X). VK has been partially supported by the Czech Ministry of Education, Youth and Sports Research Infrastructure (LM2023047). AP, JC, SE, and GB contributed useful points to the discussion. A.E. and F.P. acknowledge support through the German Space Agency DLR 50OS1501 and DLR 50OS2001 from 2015 to 2023. We also would like to thank the members of the SINFONI/NACO/VISIR and ESO’s Paranal/Chile team for their support and collaboration. This paper makes use of the following ALMA data: ADS/JAO.ALMA#2015.1.01080.S and ADS/JAO.ALMA#2012.1.00543.S. ALMA is a partnership of ESO (representing its member states), NSF (USA) and NINS (Japan), together with NRC (Canada), MOST and ASIAA (Taiwan), and KASI (Republic of Korea), in cooperation with the Republic of Chile. The Joint ALMA Observatory is operated by ESO, AUI/NRAO and NAOJ.

*Facilities:* VLT (SINFONI and NACO), ALMA (Band 7)

*Software:* astropy (Astropy Collaboration et al. 2013, 2018, 2022), SciPy (Virtanen et al. 2020), Hyperrion (Robitaille 2011, 2017), DPuser (Ott 2013)

## REFERENCES

- Ali, B., Paul, D., Eckart, A., et al. 2020, ApJ, 896, 100, doi: [10.3847/1538-4357/ab93ae](https://doi.org/10.3847/1538-4357/ab93ae)
- Allen, D. A., Hyland, A. R., & Hillier, D. J. 1990, MNRAS, 244, 706

- Astropy Collaboration, Robitaille, T. P., Tollerud, E. J., et al. 2013, *A&A*, 558, A33, doi: [10.1051/0004-6361/201322068](https://doi.org/10.1051/0004-6361/201322068)
- Astropy Collaboration, Price-Whelan, A. M., Sipőcz, B. M., et al. 2018, *AJ*, 156, 123, doi: [10.3847/1538-3881/aabc4f](https://doi.org/10.3847/1538-3881/aabc4f)
- Astropy Collaboration, Price-Whelan, A. M., Lim, P. L., et al. 2022, *ApJ*, 935, 167, doi: [10.3847/1538-4357/ac7c74](https://doi.org/10.3847/1538-4357/ac7c74)
- Baumgardt, H., Amaro-Seoane, P., & Schödel, R. 2018, *A&A*, 609, A28, doi: [10.1051/0004-6361/201730462](https://doi.org/10.1051/0004-6361/201730462)
- Beckwith, S. V. W., Sargent, A. I., Chini, R. S., & Guesten, R. 1990, *AJ*, 99, 924, doi: [10.1086/115385](https://doi.org/10.1086/115385)
- Berrilli, F., Corciulo, G., Ingrassio, G., et al. 1992, *ApJ*, 398, 254, doi: [10.1086/171853](https://doi.org/10.1086/171853)
- Bhat, H. K., Sabha, N. B., Zajaček, M., et al. 2022, *ApJ*, 929, 178, doi: [10.3847/1538-4357/ac6106](https://doi.org/10.3847/1538-4357/ac6106)
- Blum, R. D., Sellgren, K., & Depoy, D. L. 1996, *ApJ*, 470, 864, doi: [10.1086/177917](https://doi.org/10.1086/177917)
- Bodensteiner, J., Sana, H., Wang, C., et al. 2021, *A&A*, 652, A70, doi: [10.1051/0004-6361/202140507](https://doi.org/10.1051/0004-6361/202140507)
- Bonnet, H., Abuter, R., Baker, A., et al. 2004, *The Messenger*, 117, 17
- Brinch, C., Crapsi, A., Hogerheijde, M. R., & Jørgensen, J. K. 2007, *A&A*, 461, 1037, doi: [10.1051/0004-6361:20065473](https://doi.org/10.1051/0004-6361:20065473)
- Buchholz, R. M., Witzel, G., Schödel, R., & Eckart, A. 2013, *A&A*, 557, A82, doi: [10.1051/0004-6361/201220338](https://doi.org/10.1051/0004-6361/201220338)
- CASA Team, Bean, B., Bhatnagar, S., et al. 2022, *PASP*, 134, 114501, doi: [10.1088/1538-3873/ac9642](https://doi.org/10.1088/1538-3873/ac9642)
- Chiang, E. I., & Goldreich, P. 1997, *ApJ*, 490, 368, doi: [10.1086/304869](https://doi.org/10.1086/304869)
- Ciurlo, A., Campbell, R. D., Morris, M. R., et al. 2020, *Nature*, 577, 337, doi: [10.1038/s41586-019-1883-y](https://doi.org/10.1038/s41586-019-1883-y)
- Clénet, Y., Rouan, D., Gratadour, D., Gendron, E., & Lacombe, F. 2003, in *SF2A-2003: Semaine de l’Astrophysique Française*, ed. F. Combes, D. Barret, T. Contini, & L. Pagani, 163
- Clénet, Y., Rouan, D., Gratadour, D., Gendron, E., & Lacombe, F. 2005, in *Science with Adaptive Optics*, ed. W. Brandner & M. E. Kasper (Berlin, Heidelberg: Springer Berlin Heidelberg), 286–290
- Comerón, F., & Schneider, N. 2007, *A&A*, 473, 149, doi: [10.1051/0004-6361:20077733](https://doi.org/10.1051/0004-6361:20077733)
- Comerón, F., Schneider, N., & Russeil, D. 2005, *A&A*, 433, 955, doi: [10.1051/0004-6361:20041586](https://doi.org/10.1051/0004-6361:20041586)
- Davies, R., Esposito, S., Schmid, H. M., et al. 2018, in *Society of Photo-Optical Instrumentation Engineers (SPIE) Conference Series*, Vol. 10702, *Ground-based and Airborne Instrumentation for Astronomy VII*, ed. C. J. Evans, L. Simard, & H. Takami, 1070209, doi: [10.1117/12.2311480](https://doi.org/10.1117/12.2311480)
- Do, T., Hees, A., Ghez, A., et al. 2019, *Science*, 365, 664, doi: [10.1126/science.aav8137](https://doi.org/10.1126/science.aav8137)
- Draine, B. T. 2003, *ARA&A*, 41, 241, doi: [10.1146/annurev.astro.41.011802.094840](https://doi.org/10.1146/annurev.astro.41.011802.094840)
- Duchêne, G., Simon, T., Eisloffel, J., & Bouvier, J. 2001, *A&A*, 379, 147, doi: [10.1051/0004-6361:20011305](https://doi.org/10.1051/0004-6361:20011305)
- Eckart, A., & Genzel, R. 1996, *Nature*, 383, 415, doi: [10.1038/383415a0](https://doi.org/10.1038/383415a0)
- . 1997, *MNRAS*, 284, 576, doi: [10.1093/mnras/284.3.576](https://doi.org/10.1093/mnras/284.3.576)
- Eckart, A., Moulataka, J., Viehmann, T., Straubmeier, C., & Mouawad, N. 2004, *ApJ*, 602, 760, doi: [10.1086/381178](https://doi.org/10.1086/381178)
- Eckart, A., Mužić, K., Yazici, S., et al. 2013, *aap*, 551, A18, doi: [10.1051/0004-6361/201219994](https://doi.org/10.1051/0004-6361/201219994)
- Eckart, A., Hüttemann, A., Kiefer, C., et al. 2017, *Foundations of Physics*, 47, 553, doi: [10.1007/s10701-017-0079-2](https://doi.org/10.1007/s10701-017-0079-2)
- Eisenhauer, F., Abuter, R., Bickert, K., et al. 2003, in *Proc. SPIE*, Vol. 4841, *Instrument Design and Performance for Optical/Infrared Ground-based Telescopes*, ed. M. Iye & A. F. M. Moorwood, 1548–1561, doi: [10.1117/12.459468](https://doi.org/10.1117/12.459468)
- Event Horizon Telescope Collaboration, Akiyama, K., Alberdi, A., et al. 2022, *ApJL*, 930, L12, doi: [10.3847/2041-8213/ac6674](https://doi.org/10.3847/2041-8213/ac6674)
- Fritz, T. K., Gillessen, S., Dodds-Eden, K., et al. 2010, *ApJ*, 721, 395, doi: [10.1088/0004-637X/721/1/395](https://doi.org/10.1088/0004-637X/721/1/395)
- . 2011, *ApJ*, 737, 73, doi: [10.1088/0004-637X/737/2/73](https://doi.org/10.1088/0004-637X/737/2/73)
- Gautam, A. K., Do, T., Ghez, A. M., et al. 2019, *ApJ*, 871, 103, doi: [10.3847/1538-4357/aaf103](https://doi.org/10.3847/1538-4357/aaf103)
- Genzel, R. 2022, *Reviews of Modern Physics*, 94, 020501, doi: [10.1103/RevModPhys.94.020501](https://doi.org/10.1103/RevModPhys.94.020501)
- Genzel, R., Pichon, C., Eckart, A., Gerhard, O. E., & Ott, T. 2000, *MNRAS*, 317, 348, doi: [10.1046/j.1365-8711.2000.03582.x](https://doi.org/10.1046/j.1365-8711.2000.03582.x)
- Genzel, R., Thatte, N., Krabbe, A., Kroker, H., & Tacconi-Garman, L. E. 1996, *ApJ*, 472, 153, doi: [10.1086/178051](https://doi.org/10.1086/178051)
- Genzel, R., Schödel, R., Ott, T., et al. 2003, *ApJ*, 594, 812, doi: [10.1086/377127](https://doi.org/10.1086/377127)
- Ghez, A. M., Duchêne, G., Matthews, K., et al. 2003, *ApJL*, 586, L127, doi: [10.1086/374804](https://doi.org/10.1086/374804)
- Gibb, E. L., Whittet, D. C. B., Schutte, W. A., et al. 2000, *ApJ*, 536, 347, doi: [10.1086/308940](https://doi.org/10.1086/308940)
- Gillessen, S., Genzel, R., Fritz, T. K., et al. 2012, *Nature*, 481, 51, doi: [10.1038/nature10652](https://doi.org/10.1038/nature10652)
- Glassgold, A. E., Najita, J., & Igea, J. 2004, *apj*, 615, 972, doi: [10.1086/424509](https://doi.org/10.1086/424509)
- Gravity Collaboration, Abuter, R., Amorim, A., et al. 2018, *A&A*, 615, L15, doi: [10.1051/0004-6361/201833718](https://doi.org/10.1051/0004-6361/201833718)

- Habibi, M., Gillessen, S., Martins, F., et al. 2017, *ApJ*, 847, 120, doi: [10.3847/1538-4357/aa876f](https://doi.org/10.3847/1538-4357/aa876f)
- Hansen, B. M. S., & Milosavljević, M. 2003, *ApJL*, 593, L77, doi: [10.1086/378182](https://doi.org/10.1086/378182)
- Hobbs, A., & Nayakshin, S. 2009, *MNRAS*, 394, 191, doi: [10.1111/j.1365-2966.2008.14359.x](https://doi.org/10.1111/j.1365-2966.2008.14359.x)
- Höfner, S., & Freytag, B. 2019, *A&A*, 623, A158, doi: [10.1051/0004-6361/201834799](https://doi.org/10.1051/0004-6361/201834799)
- Hosseini, S. E., Zajaček, M., Eckart, A., Sabha, N. B., & Labadie, L. 2020, *A&A*, 644, A105, doi: [10.1051/0004-6361/202037724](https://doi.org/10.1051/0004-6361/202037724)
- Ishii, M., Nagata, T., Sato, S., et al. 1998, *AJ*, 116, 868, doi: [10.1086/300467](https://doi.org/10.1086/300467)
- Ito, M., Yamashita, T., Sako, S., et al. 2008, *ApJ*, 672, 398, doi: [10.1086/523808](https://doi.org/10.1086/523808)
- Ivezic, Z., Nenkova, M., & Elitzur, M. 1999, *DUSTY: Radiation transport in a dusty environment*, Astrophysics Source Code Library, record ascl:9911.001. <http://ascl.net/9911.001>
- Jalali, B., Pelupessy, F. I., Eckart, A., et al. 2014, *MNRAS*, 444, 1205, doi: [10.1093/mnras/stu1483](https://doi.org/10.1093/mnras/stu1483)
- Kenyon, S. J., & Hartmann, L. 1995, *ApJS*, 101, 117, doi: [10.1086/192235](https://doi.org/10.1086/192235)
- Kozasa, T., & Sogawa, H. 1999, in *Asymptotic Giant Branch Stars*, ed. T. Le Bertre, A. Lebre, & C. Waelkens, Vol. 191, 239
- Lada, C. J. 1987, in *IAU Symposium*, Vol. 115, *Star Forming Regions*, ed. M. Peimbert & J. Jugaku, 1
- Lada, C. J., & Adams, F. C. 1992, *ApJ*, 393, 278, doi: [10.1086/171505](https://doi.org/10.1086/171505)
- Lahuis, F., van Dishoeck, E. F., Boogert, A. C. A., et al. 2006, *ApJL*, 636, L145, doi: [10.1086/500084](https://doi.org/10.1086/500084)
- Leinert, C., Graser, U., Przygodda, F., et al. 2003, *Ap&SS*, 286, 73, doi: [10.1023/A:1026158127732](https://doi.org/10.1023/A:1026158127732)
- Lenzen, R., Hartung, M., Brandner, W., et al. 2003, in *Proc. SPIE*, Vol. 4841, *Instrument Design and Performance for Optical/Infrared Ground-based Telescopes*, ed. M. Iye & A. F. M. Moorwood, 944–952, doi: [10.1117/12.460044](https://doi.org/10.1117/12.460044)
- Lu, J. R., Do, T., Ghez, A. M., et al. 2013, *ApJ*, 764, 155, doi: [10.1088/0004-637X/764/2/155](https://doi.org/10.1088/0004-637X/764/2/155)
- Lucy, L. B. 1974, *AJ*, 79, 745, doi: [10.1086/111605](https://doi.org/10.1086/111605)
- Lutz, D., Krabbe, A., & Genzel, R. 1993, *ApJ*, 418, 244, doi: [10.1086/173386](https://doi.org/10.1086/173386)
- Maillard, J. P., Paumard, T., Stolovy, S. R., & Rigaut, F. 2004, *A&A*, 423, 155, doi: [10.1051/0004-6361:20034147](https://doi.org/10.1051/0004-6361:20034147)
- Martín, S., Martín-Pintado, J., Montero-Castaño, M., Ho, P. T. P., & Blundell, R. 2012, *A&A*, 539, A29, doi: [10.1051/0004-6361/201117268](https://doi.org/10.1051/0004-6361/201117268)
- Menten, K. M., Reid, M. J., Eckart, A., & Genzel, R. 1997, *ApJL*, 475, L111, doi: [10.1086/310472](https://doi.org/10.1086/310472)
- Moneti, A., Cernicharo, J., & Pardo, J. R. 2001, *ApJL*, 549, L203, doi: [10.1086/319168](https://doi.org/10.1086/319168)
- Morris, M. 1993, *ApJ*, 408, 496, doi: [10.1086/172607](https://doi.org/10.1086/172607)
- Moser, L., Sánchez-Monge, Á., Eckart, A., et al. 2017, *A&A*, 603, A68, doi: [10.1051/0004-6361/201628385](https://doi.org/10.1051/0004-6361/201628385)
- Moultaka, J., Eckart, A., & Mužić, K. 2015, *ApJ*, 806, 202, doi: [10.1088/0004-637X/806/2/202](https://doi.org/10.1088/0004-637X/806/2/202)
- Murray-Clay, R. A., & Loeb, A. 2012, *Nature Communications*, 3, 1049, doi: [10.1038/ncomms2044](https://doi.org/10.1038/ncomms2044)
- Mužić, K., Eckart, A., Schödel, R., et al. 2010, *A&A*, 521, A13, doi: [10.1051/0004-6361/200913087](https://doi.org/10.1051/0004-6361/200913087)
- Mužić, K., Schödel, R., Eckart, A., Meyer, L., & Zensus, A. 2008, *A&A*, 482, 173, doi: [10.1051/0004-6361:20078352](https://doi.org/10.1051/0004-6361:20078352)
- Ojha, D. K., Tamura, M., Nakajima, Y., et al. 2009, *ApJ*, 693, 634, doi: [10.1088/0004-637X/693/1/634](https://doi.org/10.1088/0004-637X/693/1/634)
- Ott, T. 2013, *DPUSER: Interactive language for image analysis*. <http://ascl.net/1303.025>
- Ott, T., Eckart, A., & Genzel, R. 1999, *ApJ*, 523, 248, doi: [10.1086/307712](https://doi.org/10.1086/307712)
- Parsa, M., Eckart, A., Shahzamanian, B., et al. 2017, *ApJ*, 845, 22, doi: [10.3847/1538-4357/aa7bf0](https://doi.org/10.3847/1538-4357/aa7bf0)
- Paumard, T., Genzel, R., Martins, F., et al. 2006, *The Astrophysical Journal*, 643, 1011. <http://stacks.iop.org/0004-637X/643/i=2/a=1011>
- Peißker, F., Eckart, A., Sabha, N. B., Zajaček, M., & Bhat, H. 2020c, *ApJ*, 897, 28, doi: [10.3847/1538-4357/ab9826](https://doi.org/10.3847/1538-4357/ab9826)
- Peißker, F., Eckart, A., Zajaček, M., & Britzen, S. 2022, *ApJ*, 933, 49, doi: [10.3847/1538-4357/ac752f](https://doi.org/10.3847/1538-4357/ac752f)
- Peißker, F., Hosseini, S. E., Zajaček, M., et al. 2020b, *A&A*, 634, A35, doi: [10.1051/0004-6361/201935953](https://doi.org/10.1051/0004-6361/201935953)
- Peißker, F., Zajaček, M., Eckart, A., et al. 2019, *A&A*, 624, A97, doi: [10.1051/0004-6361/201834947](https://doi.org/10.1051/0004-6361/201834947)
- Peißker, F., Ali, B., Zajaček, M., et al. 2021a, *ApJ*, 909, 62, doi: [10.3847/1538-4357/abd9c6](https://doi.org/10.3847/1538-4357/abd9c6)
- Peißker, F., Zajaček, M., Eckart, A., et al. 2021c, *ApJ*, 923, 69, doi: [10.3847/1538-4357/ac23df](https://doi.org/10.3847/1538-4357/ac23df)
- . 2023a, *ApJ*, 943, 183, doi: [10.3847/1538-4357/acb435](https://doi.org/10.3847/1538-4357/acb435)
- Peißker, F., Zajaček, M., Sabha, N. B., et al. 2023b, *ApJ*, 944, 231, doi: [10.3847/1538-4357/aca977](https://doi.org/10.3847/1538-4357/aca977)
- Pfuhl, O., Alexander, T., Gillessen, S., et al. 2014, *ApJ*, 782, 101, doi: [10.1088/0004-637X/782/2/101](https://doi.org/10.1088/0004-637X/782/2/101)
- Portegies Zwart, S. F., & McMillan, S. L. W. 2002, *ApJ*, 576, 899, doi: [10.1086/341798](https://doi.org/10.1086/341798)
- Portegies Zwart, S. F., McMillan, S. L. W., & Gieles, M. 2010, *ARA&A*, 48, 431, doi: [10.1146/annurev-astro-081309-130834](https://doi.org/10.1146/annurev-astro-081309-130834)
- Pott, J. U., Eckart, A., Glindemann, A., et al. 2008, *A&A*, 480, 115, doi: [10.1051/0004-6361:20066733](https://doi.org/10.1051/0004-6361:20066733)



- Reipurth, B., & Zinnecker, H. 1993, *A&A*, 278, 81
- Rieke, G. H., & Lebofsky, M. J. 1985, *ApJ*, 288, 618, doi: [10.1086/162827](https://doi.org/10.1086/162827)
- Robitaille, T. P. 2011, *A&A*, 536, A79, doi: [10.1051/0004-6361/201117150](https://doi.org/10.1051/0004-6361/201117150)
- . 2017, *A&A*, 600, A11, doi: [10.1051/0004-6361/201425486](https://doi.org/10.1051/0004-6361/201425486)
- Roche, P. F., Lopez-Rodriguez, E., Telesco, C. M., Schödel, R., & Packham, C. 2018, *MNRAS*, 476, 235, doi: [10.1093/mnras/sty129](https://doi.org/10.1093/mnras/sty129)
- Rousset, G., Lacombe, F., Puget, P., et al. 2003, in *Proc. SPIE*, Vol. 4839, *Adaptive Optical System Technologies II*, ed. P. L. Wizinowich & D. Bonaccini, 140–149, doi: [10.1117/12.459332](https://doi.org/10.1117/12.459332)
- Sana, H., de Mink, S. E., de Koter, A., et al. 2012, *Science*, 337, 444, doi: [10.1126/science.1223344](https://doi.org/10.1126/science.1223344)
- Schödel, R., Eckart, A., Iserlohe, C., Genzel, R., & Ott, T. 2005, *ApJL*, 625, L111, doi: [10.1086/431307](https://doi.org/10.1086/431307)
- Schödel, R., Merritt, D., & Eckart, A. 2009, *A&A*, 502, 91, doi: [10.1051/0004-6361/200810922](https://doi.org/10.1051/0004-6361/200810922)
- Schödel, R., Morris, M. R., Muzic, K., et al. 2011, *A&A*, 532, A83, doi: [10.1051/0004-6361/201116994](https://doi.org/10.1051/0004-6361/201116994)
- Scoville, N., & Burkert, A. 2013, *apj*, 768, 108, doi: [10.1088/0004-637X/768/2/108](https://doi.org/10.1088/0004-637X/768/2/108)
- Scoville, N. Z., Stolovy, S. R., Rieke, M., Christopher, M., & Yusef-Zadeh, F. 2003, *ApJ*, 594, 294, doi: [10.1086/376790](https://doi.org/10.1086/376790)
- Shahzamanian, B., Schödel, R., Noguerras-Lara, F., et al. 2022, *A&A*, 662, A11, doi: [10.1051/0004-6361/202142687](https://doi.org/10.1051/0004-6361/202142687)
- Shahzamanian, B., Eckart, A., Zajaček, M., et al. 2016, *A&A*, 593, A131, doi: [10.1051/0004-6361/201628994](https://doi.org/10.1051/0004-6361/201628994)
- Sicilia-Aguilar, A., Banzatti, A., Carmona, A., et al. 2016, *PASA*, 33, e059, doi: [10.1017/pasa.2016.56](https://doi.org/10.1017/pasa.2016.56)
- Stewart, P. N., Tuthill, P. G., Monnier, J. D., et al. 2016, *MNRAS*, 455, 3102, doi: [10.1093/mnras/stv2454](https://doi.org/10.1093/mnras/stv2454)
- Tsuboi, M., Kitamura, Y., Tsutsumi, T., et al. 2019, *PASJ*, 71, 105, doi: [10.1093/pasj/psz089](https://doi.org/10.1093/pasj/psz089)
- . 2020a, *PASJ*, 72, 36, doi: [10.1093/pasj/psaa013](https://doi.org/10.1093/pasj/psaa013)
- . 2020b, *PASJ*, 72, L5, doi: [10.1093/pasj/psaa016](https://doi.org/10.1093/pasj/psaa016)
- . 2017a, *ApJL*, 850, L5, doi: [10.3847/2041-8213/aa97d3](https://doi.org/10.3847/2041-8213/aa97d3)
- Tsuboi, M., Kitamura, Y., Uehara, K., et al. 2017b, *ApJ*, 842, 94, doi: [10.3847/1538-4357/aa74e3](https://doi.org/10.3847/1538-4357/aa74e3)
- Tsuchikawa, T., Kaneda, H., Oyabu, S., et al. 2021, *A&A*, 651, A117, doi: [10.1051/0004-6361/202140483](https://doi.org/10.1051/0004-6361/202140483)
- Tursunov, A., Zajaček, M., Eckart, A., et al. 2020, *ApJ*, 897, 99, doi: [10.3847/1538-4357/ab980e](https://doi.org/10.3847/1538-4357/ab980e)
- Ulrich, R. K. 1976, *ApJ*, 210, 377, doi: [10.1086/154840](https://doi.org/10.1086/154840)
- Viehmann, T. 2007, PhD thesis, Andreas Eckart University of Cologne, Germany
- Viehmann, T., Eckart, A., Schödel, R., Pott, J. U., & Moulataka, J. 2006, *ApJ*, 642, 861, doi: [10.1086/501345](https://doi.org/10.1086/501345)
- Virtanen, P., Gommers, R., Oliphant, T. E., et al. 2020, *Nature Methods*, 17, 261, doi: [10.1038/s41592-019-0686-2](https://doi.org/10.1038/s41592-019-0686-2)
- von Fellenberg, S. D., Gillessen, S., Stadler, J., et al. 2022, *ApJL*, 932, L6, doi: [10.3847/2041-8213/ac68ef](https://doi.org/10.3847/2041-8213/ac68ef)
- Wang, Q. D., Li, J., Russell, C. M. P., & Cuadra, J. 2020, *MNRAS*, 492, 2481, doi: [10.1093/mnras/stz3624](https://doi.org/10.1093/mnras/stz3624)
- Weingartner, J. C., & Draine, B. T. 2001, *ApJS*, 134, 263, doi: [10.1086/320852](https://doi.org/10.1086/320852)
- Witzel, G., Ghez, A. M., Morris, M. R., et al. 2014, *ApJL*, 796, L8, doi: [10.1088/2041-8205/796/1/L8](https://doi.org/10.1088/2041-8205/796/1/L8)
- Zajaček, M., Britzen, S., Eckart, A., et al. 2017, *A&A*, 602, A121, doi: [10.1051/0004-6361/201730532](https://doi.org/10.1051/0004-6361/201730532)
- Zajaček, M., Karas, V., & Eckart, A. 2014, *A&A*, 565, A17, doi: [10.1051/0004-6361/201322713](https://doi.org/10.1051/0004-6361/201322713)
- Zhu, Z., Li, Z., Ciurlo, A., et al. 2020, *ApJ*, 897, 135, doi: [10.3847/1538-4357/ab980d](https://doi.org/10.3847/1538-4357/ab980d)
- Zubko, V., Dwek, E., & Arendt, R. G. 2004, *ApJS*, 152, 211, doi: [10.1086/382351](https://doi.org/10.1086/382351)

## APPENDIX

In this Appendix, we list the data used for the analysis. In addition, we compare the number of dusty sources of this work with the literature. We furthermore indicate the related proper motion of the sources investigated.

## A. DATA

In Table 10, we list the K-band data used in this work. Although the source confusion in the IRS 13 cluster is increased due to its high density, we identify K-band positions of the dusty objects in most epochs of the listed data. In addition, the prominent MIR emission of these dusty sources enables us to incorporate all investigated epochs of the listed L-band data observed with NACO (see Table 11). The ID of the GC observation in the H+K-band with SINFONI in 2014 is listed in Table 12.

## B. DUSTY OBJECTS

Here, we provide an overview of the sources investigated in this work compared to previous investigations in the literature. Table 13 exhibits all unknown and known dusty objects of the IRS 13 region with the corresponding id of the related publication. To cross-identify all sources in the literature with this work, we visually compare finding charts of the related publication listed in Table 13. We expect that future higher-resolution observations will most certainly establish a new nomenclature as it is commonly done for GC sources (please compare the analysis of Eckart et al. (2013) with Ciurlo et al. (2020)).

## C. INDIVIDUAL DETECTIONS OF THE DUSTY SOURCES

Here, we list all individual relative locations of the dusty sources investigated in this work. The related position of S2 is indicated. With the orbital elements of Do et al. (2019) and Gravity Collaboration et al. (2018), the position of Sgr A\* can be estimated, which can be transferred to the absolute location of the dusty sources. The positions of the DS sources listed in Table 14-27 are determined using a Gaussian fit. In addition, this fit provides an uncertainty which is indicated after the related numerical R.A. and DEC. value. From these tables, the bulk motion of IRS13 can be analyzed. Since this exceeds the scope of this work, we refer to Paper II for an extended analysis. Due to the consistency of the data set which transforms into a lowered confusion, we list the L-band positions in Table 14-27.

## D. K-BAND COUNTERPART OF THE DUSTY SOURCES

Here, we display the K-band counterparts for dusty sources analyzed in this work. The K-band data presented in Fig. 17 was observed in 2009 with NACO. Because of the proper motion of the DS sources, the detectability may be hindered for individual objects. Single detections of these objects, including light curves, are presented in Appendix F.

## E. H-BAND COUNTERPART OF THE DUSTY SOURCES

Near-infrared NACO observations of the DS sources in the H-band. The observations were carried out in 2004 and show the same FOV as it is presented in Fig. 3 and Fig. 17. The detection of some sources in Fig. 18 may be infected by confusion and interference, which is why we present individual detections in Appendix F.

## F. MULTI-WAVELENGTH IDENTIFICATION OF THE DUSTY SOURCES

We use the L-band emission presented in Fig. 3 as a starting point to identify the here discussed dusty sources (abbreviated with DS). Whenever feasible, we use the continuum data without any applied high-pass filter to detect the DS sources in the H-, K-, and L- bands. For the photometric analysis, we use IRS 2L and S65 with an L-band magnitude of  $10.59 \pm 0.03$  (Hosseini et al. 2020; Peißker et al. 2021a) as a calibrator. To determine the impact of the high-pass filter on the photometric analysis, we will compare the L-band magnitude of one of the brightest dusty sources, DS1, with and without the applied smooth-subtract algorithm.

As it is demonstrated in Table 5, the impact on the magnitude after applying a high-pass filter is negligible. This result is expected since Ott et al. (1999) investigated the impact of applying different high-pass filters to the data in detail. The authors found no trend regarding a specific filter for almost 30 individual sources in agreement with the comparison presented in Table 5. Although individual sources may be affected by confusion, which is translated to brighter/fainter magnitude values, we note that non-filtered data is exposed to crowding problems.

NACO K-band		
Date	Observation ID	number of exposures
2002.07.31	60.A-9026(A)	61
2003.06.13	713-0078(A)	253
2004.07.06	073.B-0775(A)	344
2004.07.08	073.B-0775(A)	285
2005.07.25	271.B-5019(A)	330
2005.07.27	075.B-0093(C)	158
2005.07.29	075.B-0093(C)	101
2005.07.30	075.B-0093(C)	187
2005.07.30	075.B-0093(C)	266
2005.08.02	075.B-0093(C)	80
2006.08.02	077.B-0014(D)	48
2006.09.23	077.B-0014(F)	48
2006.09.24	077.B-0014(F)	53
2006.10.03	077.B-0014(F)	48
2006.10.20	078.B-0136(A)	47
2007.03.04	078.B-0136(B)	48
2007.03.20	078.B-0136(B)	96
2007.04.04	179.B-0261(A)	63
2007.05.15	079.B-0018(A)	116
2008.02.23	179.B-0261(L)	72
2008.03.13	179.B-0261(L)	96
2008.04.08	179.B-0261(M)	96
2009.04.21	178.B-0261(W)	96
2009.05.03	183.B-0100(G)	144
2009.05.16	183.B-0100(G)	78
2009.07.03	183.B-0100(D)	80
2009.07.04	183.B-0100(D)	80
2009.07.05	183.B-0100(D)	139
2009.07.05	183.B-0100(D)	224
2009.07.06	183.B-0100(D)	56
2009.07.06	183.B-0100(D)	104
2009.08.10	183.B-0100(I)	62
2009.08.12	183.B-0100(I)	101
2010.03.29	183.B-0100(L)	96
2010.05.09	183.B-0100(T)	12
2010.05.09	183.B-0100(T)	24
2010.06.12	183.B-0100(T)	24
2010.06.16	183.B-0100(U)	48
2011.05.27	087.B-0017(A)	305
2012.05.17	089.B-0145(A)	169
2013.06.28	091.B-0183(A)	112
2017.06.16	598.B-0043(L)	36
2018.04.24	101.B-0052(B)	120

**Table 10.** K-band data observed with NACO between 2002 and 2018.

NACO L-band		
Date	Observation ID	number of exposures
2002.08.30	060.A-9026(A)	80
2003.05.10	071.B-0077(A)	56
2004.07.06	073.B-0775(A)	217
2005.05.13	073.B-0085(E)	108
2005.06.20	073.B-0085(F)	100
2006.05.28	077.B-0552(A)	46
2006.06.01	077.B-0552(A)	244
2007.03.17	078.B-0136(B)	78
2007.04.01	179.B-0261(A)	96
2007.04.02	179.B-0261(A)	150
2007.04.02	179.B-0261(A)	72
2007.04.06	179.B-0261(A)	175
2007.06.09	179.B-0261(H)	40
2008.05.28	081.B-0648(A)	58
2008.08.05	179.B-0261(N)	64
2008.09.14	179.B-0261(U)	49
2009.03.29	179.B-0261(X)	32
2009.03.31	179.B-0261(X)	32
2009.04.03	082.B-0952(A)	42
2009.04.05	082.B-0952(A)	12
2009.09.19	183.B-0100(J)	132
2009.09.20	183.B-0100(J)	80
2010.07.02	183.B-0100(Q)	485
2011.05.25	087.B-0017(A)	29
2012.05.16	089.B-0145(A)	30
2013.05.09	091.C-0159(A)	30
2015.09.21	594.B-0498(G)	420
2016.03.23	096.B-0174(A)	60
2017.03.23	098.B-0214(B)	30
2018.04.22	0101.B-0065(A)	68
2018.04.24	0101.B-0065(A)	50

**Table 11.** L-band data observed with NACO between 2002 and 2018.

Date (YYYY:MM:DD)	Observation ID	Exp. Time (s)	Band	Instrument/Telescope
2014.08.30	093.B-0218(B)	2700	H+K	SINFONI/VLT

**Table 12.** SINFONI data used in this work for the identification of the iron line (see Fig. 14). We applied the standard reduction steps provided by the ESO pipeline to create the final mosaic.

### F.1. DS1

The source DS1 is one of the brightest H- and K-band object of the here presented sample. In Fig. 19, we show a confusion-free detection of DS1 in 2004 including the light curve based on the H-, K-, and L-band NACO data observed between 2002 and 2018. In Table 28, we list the mean and median magnitude with the related standard deviation based on the here analyzed data set.

ID	Maillard et al. (2004)	Schödel et al. (2005)	Mužić et al. (2008)	Fritz et al. (2010)	Eckart et al. (2013)
$\alpha$			×		8
$\beta$			×		9
$\gamma$			×		22
$\delta$			×		17
$\epsilon$			×		13
$\zeta$			×		34
$\eta$	15	×	×		19
$\theta$					
$\iota$		×			10
1		×	×		
2					
3					
4		×			
5					
6					
7					
8					
9		×			
10		×			
11	14	×	×		15
12	13	×	×		16
13					
14					
15					
16					
17	20	×	×		
18					
19					
20		×			
21					
22					23
23					
24	18	×			
25		×			
26			×		7
27	16		×		20
28					
29					
30					
31					
32					
33					
E1	×	×	×	×	1
E2	×	×	×	×	2
E3	×	×	×	×	3
E4	×	×		×	4
E5.0	×		×	×	5
E5.1				×	
E7	5	×	×	×	25

**Table 13.** Identification of all the sources investigated in this work. As listed, the nomenclature is not consistent throughout the literature. A  $\times$  symbol indicates the detection in the related publication. If the sources were labeled with an alternative ID, we additionally list the corresponding number.

Epoch	S2 R.A.	S2 err R.A.	S2 Dec.	S2 err Dec.	$\alpha$ R.A.	$\alpha$ err R.A.	$\alpha$ Dec.	$\alpha$ err Dec.	$\beta$ R.A.	$\beta$ err R.A.	$\beta$ Dec.	$\beta$ err Dec.
2002-08-29	685.59	0.02	764.57	0.02	785.34	0.16	709.63	0.2	793.34	0.06	718.19	0.03
2002-08-30	1121.1	0.03	787.88	0.03	1221	0.12	733.01	0.13	1229.2	0.08	741.59	0.04
2003-05-10	873.79	0.04	743.43	0.04	974.42	0.1	686.39	0.1	982.09	0.04	695.06	0.03
2004-04-25	678.01	0.07	640.11	0.05	778.16	0.1	580.8	0.14	785.78	0.04	589.59	0.03
2004-04-26	678.09	0.04	640.29	0.04	778.08	0.1	580.86	0.15	785.91	0.06	589.73	0.05
2005-05-13	788.84	0.06	776.4	0.05	888.24	0.1	717.19	0.1	895.85	0.04	725.98	0.03
2006-05-29	744.23	0.04	747.74	0.05	843.14	0.2	687.49	0.3	850.76	0.03	696.36	0.03
2007-04-01	1043.3	0.02	1050.8	0.02	1141.9	0.1	990.24	0.11	1149.7	0.05	999.13	0.04
2007-05-15	1040.2	0.06	1052.2	0.05	1138.7	0.1	991.3	0.1	1146.7	0.04	1000.1	0.04
2007-05-16	1011.6	0.04	1074.3	0.04	1110.1	0.1	1013.9	0.2	1118.2	0.04	1022.7	0.04
2007-05-17	1038.9	0.08	1061.1	0.08	1137.5	0.1	1000.6	0.1	1145.4	0.04	1009.3	0.04
2007-05-18	1050.3	0.02	1051	0.02	1148.5	0.11	990.64	0.13	1156.8	0.06	999.32	0.04
2007-05-19	972.05	0.05	1042.4	0.04	1070.7	0.1	981.88	0.11	1078.7	0.04	991.04	0.03
2007-05-22	808.75	0.02	812.64	0.02	907.15	0.2	752.18	0.23	915.17	0.04	760.98	0.03
2007-05-23	1057	0.03	1082.6	0.03	1155.5	0.09	1022.2	0.13	1163.4	0.04	1031	0.03
2008-05-26	1020	0.1	1110.9	0.1	1117.9	0.1	1049.4	0.1	1125.8	0.1	1058.3	0.1
2008-05-30	988.24	0.1	1100.9	0.1	1086.1	0.1	1039.5	0.1	1094	0.1	1048.4	0.1
2008-05-31	1049.2	0.1	1070.8	0.1	1147.2	0.1	1009.5	0.1	1155.2	0.1	1018.4	0.1
2008-06-02	1056.8	0.1	1071.1	0.1	1154.6	0.1	1009.9	0.2	1162.8	0.1	1018.7	0.1
2008-06-03	1060.4	0.1	1072.2	0.1	1158.4	0.1	1010.6	0.1	1166.3	0.1	1019.6	0.1
2011-05-25	866.21	0.02	850.86	0.02	962.21	0.1	790.05	0.11	970.45	0.04	799.06	0.03
2012-05-16	867.6	0.04	787.45	0.04	963.27	0.15	727.04	0.17	971.41	0.03	736.26	0.03
2013-05-09	870.72	0.08	786.15	0.07	966.26	0.1	725.86	0.13	974.18	0.03	735.16	0.03
2016-03-23	847.81	0.05	826.22	0.04	943.31	0.13	769.88	0.13	951.02	0.04	779.4	0.03
2018-04-22	850.83	0.03	761.76	0.06	947.89	0.0846	709.41	0.13	956.11	0.04	718.83	0.06
2018-04-24	852.93	0.03	758.05	0.04	950.43	0.11	704.96	0.13	958.33	0.05	714.66	0.05

**Table 14.** Relative pixel positions of S2 and the dusty sources. From the position of S2, the location of Sgr A\* can be estimated. With this, the absolute positions of the dusty sources can be calculated. The uncertainties represent the Gaussian fit error.

### F.2. DS2 & DS3

In Figure 20, we show the detection of DS2 and DS3. We do not detect a K- and H-band counterpart above the noise level for both sources, which is due to the high level of crowding. However, NACO K-band data of 2018 reveals some promising candidates that might be associated with DS2 and DS3. However, both faint sources demonstrate the challenges of the analysis and the need for high-resolution IFU data. We list the related L-band magnitude in Table 29.

### F.3. DS4

In Fig. 21, we present the multi-wavelength identification of DS4. Despite the close distance to DS1, the object DS4 can be observed without confusion. This object is a prime example of magnitude-confusion susceptibility; if the investigated object is bright enough, the close distance to a brighter object does not impact the observability. An example of a toxic magnitude-confusion susceptibility is displayed in Fig. 20. Table 30 lists the magnitude of DS4 in several IR bands.

### F.4. DS5

The L-band detection of DS5 close to DS1. As for DS2 and DS3, the magnitude-confusion susceptibility is high, which might be the reason for the non-detection of DS5 in the H- and K-band. The classification of a core-less dust blob is rather unlikely because of evaporation time scales in a radiative-dominated environment. For example, Stewart et al. (2016) and Höfner & Freytag (2019) report variations of dust clouds close to stars on time scales of a few years. As before, we list the corresponding L-band magnitude for DS5 in Table 31.

Epoch	$\gamma$ R.A.	$\gamma$ err R.A.	$\gamma$ Dec.	$\gamma$ err Dec.	$\delta$ R.A.	$\delta$ err R.A.	$\delta$ Dec.	$\delta$ err Dec.	$\epsilon$ R.A.	$\epsilon$ err R.A.	$\epsilon$ Dec.	$\epsilon$ err Dec.
2002-08-29	800.82	0.06	726.94	0.04	793.93	0.05	732.58	0.04	793.15	0.12	726.72	0.07
2002-08-30	1236.5	0.05	750.27	0.03	1229.6	0.05	755.81	0.03	1228.5	0.08	749.47	0.04
2003-05-10	989.62	0.07	704.04	0.05	982.75	0.04	709.72	0.03	981.74	0.1	703.63	0.07
2004-04-25	793.5	0.09	598.65	0.07	786.52	0.05	604.21	0.04	785.46	0.09	598	0.06
2004-04-26	793.4	0.1	598.63	0.09	786.37	0.09	604.21	0.07	785.41	0.09	598.06	0.06
2005-05-13	903.59	0.09	735.11	0.08	896.47	0.1	740.59	0.08	895.55	0.16	734.65	0.1
2006-05-29	858.64	0.07	705.52	0.06	851.56	0.05	710.96	0.04	850.61	0.1	705.13	0.07
2007-04-01	1157.6	0.1	1008.4	0.07	1150.5	0.05	1013.8	0.04	1149.6	0.1	1007.9	0.06
2007-05-15	1154.7	0.08	1009.5	0.06	1147.4	0.07	1014.8	0.06	1146.6	0.15	1008.8	0.09
2007-05-16	1126	0.08	1032	0.06	1118.7	0.0875	1037	0.08	1118.1	0.09	1031.3	0.05
2007-05-17	1153.5	0.07	1018.7	0.05	1146.3	0.046	1024	0.03	1145.4	0.1	1018.3	0.07
2007-05-18	1164.7	0.07	1008.6	0.06	1157.6	0.05	1013.9	0.04	1157	0.15	1008.1	0.09
2007-05-19	1086.1	0.1	1000.3	0.09	1079.2	0.077	1005.3	0.07	1078.7	0.09	999.5	0.05
2007-05-22	923.04	0.1	770.31	0.08	916.05	0.069	775.61	0.04	915.35	0.1	770.08	0.08
2007-05-23	1171.6	0.07	1040.3	0.06	1164.3	0.06	1045.7	0.06	1163.6	0.1	1040.2	0.08
2008-05-26	1134	0.1	1067.7	0.1	1126.8	0.1	1073	0.1	1125.9	0.1	1067.1	0.1
2008-05-30	1102.2	0.1	1057.8	0.1	1095	0.1	1063.2	0.1	1093.9	0.4	1057.3	0.3
2008-05-31	1162.6	0.1	1027.9	0.1	1155.9	0.1	1032.7	0.1	1155	1	1027	1
2008-06-02	1170.7	0.1	1027.8	0.1	1163.3	0.1	1033.2	0.1	1162.8	0.2	1028	0.1
2008-06-03	1174.4	0.1	1028.9	0.1	1167.1	0.1	1034.2	0.1	1166.2	0.1	1028.4	0.1
2011-05-25	978.62	0.1	808.46	0.07	971.39	0.08	813.73	0.07	970.59	0.1	808.14	0.08
2012-05-16	979.97	0.07	745.73	0.04	972.58	0.05	750.91	0.03	971.4	0.1	745.04	0.09
2013-05-09	983.08	0.08	744.71	0.05	975.51	0.05	750.03	0.04	974.07	0.06	743.83	0.04
2016-03-23	960.02	0.11	788.97	0.06	952.31	0.06	794.27	0.05	951.13	0.16	788.2	0.11
2018-04-22	965.78	0.07	728.52	0.05	957.58	0.07	733.43	0.09	956.17	0.05	728.13	0.05
2018-04-24	968.05	0.07	724.28	0.04	959.85	0.04	729.56	0.04	958.42	0.08	723.63	0.06

**Table 15.** Relative pixel positions of the dusty sources extracted from the NACO observations between 2002 and 2018.

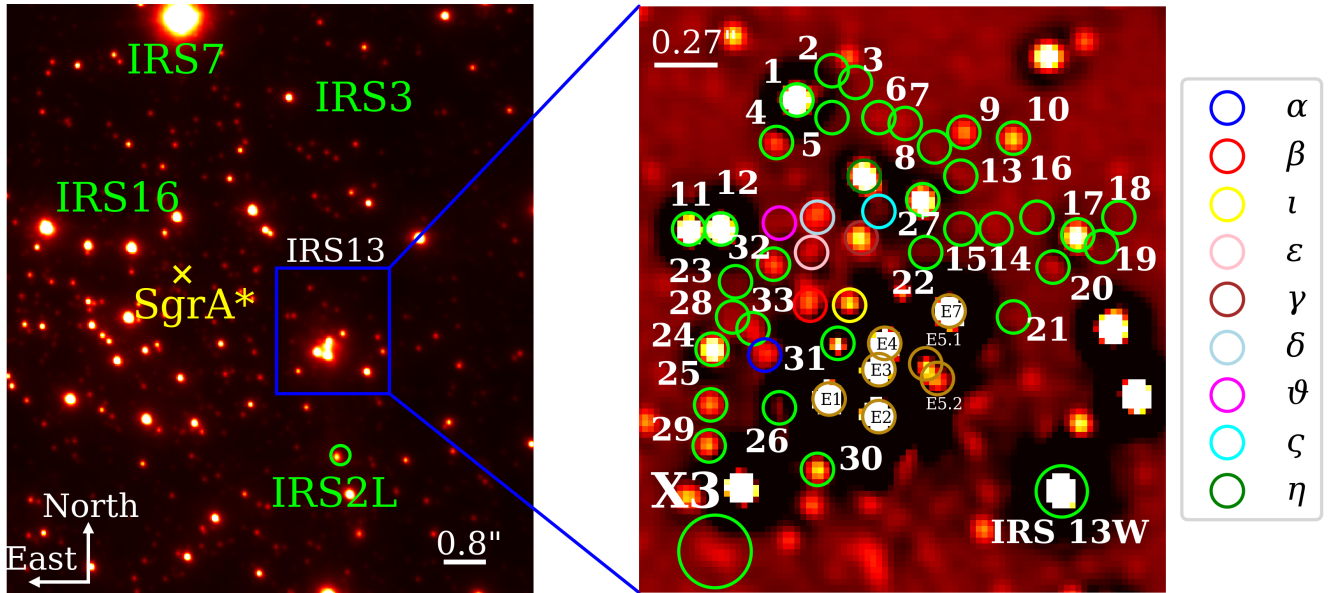


**Figure 17.** K-band observation of IRS 13 in 2009.

Epoch	$\zeta$ R.A.	$\zeta$ err R.A.	$\zeta$ Dec.	$\zeta$ err Dec.	$\eta$ R.A.	$\eta$ err R.A.	$\eta$ Dec.	$\eta$ err Dec.	$\vartheta$ R.A.	$\vartheta$ err R.A.	$\vartheta$ Dec.	$\vartheta$ err Dec.
2002-08-29	803.01	0.09	733.65	0.06	801.27	0.03	739.99	0.03	786.13	0.09	731.19	0.06
2002-08-30	1238.8	0.1	756.91	0.08	1237	0.04	763.2	0.03	1222.4	0.1	754.51	0.05
2003-05-10	991.94	0.09	710.72	0.06	990.16	0.04	716.98	0.05	974.93	0.1	708.16	0.07
2004-04-25	795.87	0.12	605.23	0.09	793.97	0.04	611.38	0.04	778.81	0.1	602.59	0.07
2004-04-26	795.66	0.1	605.28	0.05	793.92	0.04	611.47	0.04	778.52	0.09	602.73	0.06
2005-05-13	906.12	0.09	741.69	0.08	903.98	0.05	747.74	0.06	888.56	0.1	738.99	0.07
2006-05-29	861.22	0.12	712.07	0.1	859.04	0.07	718.03	0.09	843.51	0.08	709.32	0.07
2007-04-01	1160.3	0.06	1014.9	0.04	1158.1	0.05	1020.9	0.06	1143.1	0.15	1012.4	0.09
2007-05-15	1157.2	0.12	1016	0.07	1155	0.05	1021.8	0.06	1139.5	0.14	1013.5	0.08
2007-05-16	1128.7	0.05	1038.5	0.04	1126.4	0.03	1044.2	0.04	1111.1	0.09	1035.9	0.06
2007-05-17	1156	0.07	1025.2	0.04	1153.7	0.048	1030.9	0.1	1138.6	0.13	1022.6	0.09
2007-05-18	1167.3	0.12	1015.2	0.1	1165.1	0.08	1021	0.1	1149.7	0.11	1012.6	0.08
2007-05-19	1088.9	0.12	1006.8	0.12	1086.8	0.06	1012.5	0.08	1070.4	0.11	1004.3	0.1
2007-05-22	925.42	0.17	776.96	0.1	923.49	0.06	782.63	0.06	907.89	0.13	774.07	0.11
2007-05-23	1174	0.24	1047.1	0.23	1171.8	0.08	1052.6	0.1	1157.1	0.11	1044.3	0.06
2008-05-26	1136.4	0.2	1074.4	0.1	1134.4	0.1	1079.9	0.1	1119	0.16	1071.5	0.1
2008-05-30	1104.6	0.2	1064.5	0.1	1102.5	0.1	1070	0.1	1087	0.11	1061.7	0.09
2008-05-31	1165.5	0.1	1034.8	0.1	1163.4	0.1	1039.8	0.1	1148.6	0.12	1031.8	0.04
2008-06-02	1173.2	0.2	1034.7	0.1	1171.1	0.1	1040.3	0.1	1155.9	0.12	1032	0.07
2008-06-03	1176.8	0.3	1035.6	0.1	1174.7	0.1	1041.1	0.1	1159.4	0.12	1032.8	0.08
2011-05-25	981.74	0.07	815.22	0.05	979.19	0.1	820.33	0.2	964.22	0.15	812.44	0.06
2012-05-16	983.01	0.14	752.27	0.11	980.26	0.05	757.52	0.07	964.18	0.12	749.43	0.07
2013-05-09	986.26	0.13	751.34	0.08	983.42	0.05	756.57	0.06	966.74	0.09	748.38	0.09
2016-03-23	963.58	0.08	795.97	0.05	960.2	0.06	800.61	0.07	943.94	0.13	792.8	0.12
2018-04-22	968.33	0.07	735.81	0.06	965.51	0.1	740.08	0.36	948.5	0.08	732.21	0.09
2018-04-24	971	0.03	731.33	0.03	967.68	0.05	735.7	0.07	950.88	0.12	728.01	0.08

**Table 16.** Relative pixel positions of the bright dusty sources observed with NACO.

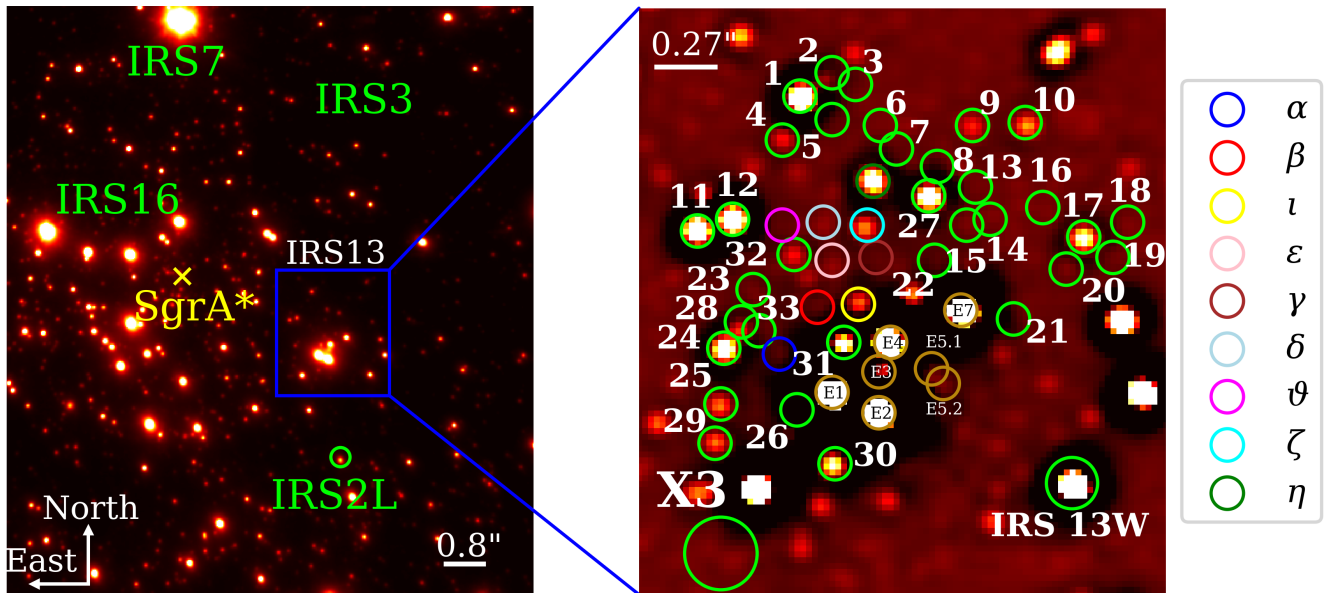


**Figure 18.** H-band observation of IRS 13 in 2004.



Epoch	$\iota$ R.A.	$\iota$ err	R.A. $\iota$ Dec.	$\iota$ err	Dec.DS1	R.A.DS1	err	R.A.DS1	Dec.DS1	err	Dec.DS2	R.A.DS2	err	R.A.DS2	Dec.DS2	err	Dec.
2002-08-29	799	2	718	2	789.83	0.0238	753.91	0.0204	795	0.5	757	0.5					
2002-08-30	1234	2	742	2	1225.6	0.0356	777.13	0.0205	1230.9	0.148	780.14	0.538					
2003-05-10	987.93	0.21	695.36	0.14	978.63	0.0343	730.78	0.0319	983.96	0.196	735.33	0.392					
2004-04-25	791.77	0.25	589.55	0.16	782.56	0.0382	625.02	0.0357	787.93	0.123	629.95	0.332					
2004-04-26	791.93	0.47	589.48	0.21	782.55	0.0239	625.1	0.0238	788.13	0.102	629.32	0.304					
2005-05-13	902.22	0.3	725.79	0.24	892.69	0.0329	761.31	0.0318	897.99	0.882	765.92	0.628					
2006-05-29	856.87	0.65	696.53	0.22	847.72	0.0245	731.44	0.0247	853.87	0.481	735.49	0.536					
2007-04-01	1156.6	0.81	998.79	0.24	1146.9	0.0285	1034.1	0.0262	1153	1	1039	1					
2007-05-15	1152.7	0.21	1000.4	0.12	1143.7	0.0278	1035.1	0.0231	1149.5	0.675	1040.6	0.388					
2007-05-16	1123.6	0.25	1023.4	0.15	1115.2	0.0305	1057.6	0.0294	1121.2	0.203	1062.3	0.255					
2007-05-17	1151.3	0.52	1010.5	0.44	1142.6	0.0365	1044.3	0.0348	1148.6	0.231	1049.2	0.248					
2007-05-18	1162.8	0.36	1000.1	0.26	1153.9	0.0396	1034.3	0.0488	1160	0.141	1038.9	0.233					
2007-05-19	1084.5	0.53	991.75	0.22	1075.6	0.0702	1025.9	0.0615	1084	1	1030	1					
2007-05-22	921.52	0.48	760.89	0.2	912.37	0.0359	795.98	0.0404	918.13	0.127	801.47	0.237					
2007-05-23	1169.8	0.3	1031.4	0.14	1160.7	0.0383	1066	0.0346	1167	0.0871	1071.4	0.182					
2008-05-26	1132.4	0.465	1058	0.22	1123.2	0.0221	1093	0.0222	1130.2	0.2	1098.5	0.2					
2008-05-30	1100.3	0.35	1048.5	0.146	1091.4	0.0197	1083.2	0.0179	1096.7	0.254	1089.7	0.375					
2008-05-31	1161	1	1018	1	1152.5	0.0378	1053.2	0.0333	1158.2	0.472	1058.9	0.266					
2008-06-02	1169	0.25	1018.7	0.15	1160.2	0.029	1053.5	0.0257	1165.5	0.481	1058.7	0.262					
2008-06-03	1173	0.13	1019.2	0.09	1163.6	0.0191	1054.4	0.0187	1169.4	0.231	1160.7	0.348					
2011-05-25	977.02	0.34	798.65	0.72	968.29	0.0306	833.15	0.027	973.42	0.148	839.71	0.237					
2012-05-16	978.49	0.3	735.83	0.15	969.27	0.0197	770.03	0.012	974.07	0.235	776.99	0.225					
2013-05-09	981.34	0.15	734.86	0.1	972.36	0.0188	768.86	0.018	976.74	0.119	777.78	0.0601					
2016-03-23	958.67	0.3	778.97	0.2	949.45	0.0165	812.33	0.0128	953.76	0.181	820.78	0.275					
2018-04-22	963.45	0.08	718.82	0.07	954.77	0.0235	751.35	0.0287	959.57	0.295	760.04	0.247					
2018-04-24	965.84	0.1	714.21	0.057	956.77	0.0292	747.19	0.0254	961.3	0.155	755.96	0.331					

**Table 17.** Dusty sources DS1-DS2 observed with NACO.F.5. *DS6 & DS7*

In Fig. 23, we present the identification of DS6 in the H-, K-, and L-band. Close to DS6, a bright star is observable in the H- and K-band with no L-band counterpart, demonstrating the challenges of the multi-wavelength analysis. In addition, Fig. 23 indicates the location of the L-band source DS7. Table 32 lists the corresponding DS6 and DS7 magnitudes.

F.6. *DS8*

Like other fainter sources, the observation of DS8 is challenging because of the surrounding stars as it is shown in Fig. 24. While the L-band emission exhibits a low level of confusion, the detection of DS8 in the NIR bands is hindered due to the presence of close-by stars. The related L-, K-, and H-band magnitude is displayed in Fig. 24 and listed in Table 33.

F.7. *DS9 & DS10*

Due to their colors presented in Fig. 9, DS9 and DS10 are most likely embedded stars such as IRS3. In Fig. 25, we show the multi-wavelength detection of the stars. Because of cosmetic reasons, we use the K-band observation of 2009 which translates in a minor offset compared to the H- and L-band data from 2004. This apparent misalignment is not in conflict with the overall identification of the two stars. Both stars show comparable magnitude values in different bands as shown in Fig. 25 and listed in Table 34

Epoch	DS3				DS4				DS5						
	R.A.	err	R.A.	Dec. err	Dec.	R.A.	err	R.A.	Dec. err	Dec.	R.A.	err	R.A.	Dec. err	Dec.
2002-08-29	799	0.5	755	0.5	786	0.5	746	0.5	795	0.5	749	0.5			
2002-08-30	1234.6	0.0727	778.65	0.0376	1222.2	0.39	769.76	0.24	1231	0.2	772.64	0.249			
2003-05-10	988.54	0.145	723.11	0.0782	975.07	0.64	723.28	0.431	984.09	0.0576	725.65	0.0811			
2004-04-25	792.24	0.0762	626.57	0.0397	778.86	0.196	617.58	0.109	787.84	0.165	620.1	0.32			
2004-04-26	792.84	0.0743	626.51	0.0588	778.57	0.248	617.72	0.088	787.78	0.314	620.6	0.479			
2005-05-13	902	0.112	763.41	0.084	888.09	0.417	754.14	0.334	897.58	0.366	756.33	0.45			
2006-05-29	858.13	0.155	733.36	0.117	844.18	0.501	724.17	0.158	853.01	0.181	726.97	0.246			
2007-04-01	1156	1	1037	1	1142.1	0.198	1026.7	0.0923	1152	0.388	1030.8	0.567			
2007-05-15	1153.9	0.235	1037.5	0.074	1140.4	0.339	1027.9	0.309	1149.2	0.157	1032.1	0.39			
2007-05-16	1125.3	0.214	1059.5	0.325	1110.5	0.325	1050.2	0.201	1120	0.5	1054	0.5			
2007-05-17	1152.5	0.159	1046.3	0.463	1137.5	0.228	1036.9	0.0974	1147.5	0.239	1040.2	0.15			
2007-05-18	1164.4	0.142	1036.2	0.375	1148.4	0.363	1027.1	0.208	1159	0.5	1031	0.5			
2007-05-19	1086	0.5	1028	0.5	1072	1	1018	1	1080	1	1021	1			
2007-05-22	922.28	0.0658	798.13	0.0572	907.78	0.123	788.53	0.0738	918	0.5	793	0.5			
2007-05-23	1170.4	0.188	1068.4	0.0806	1156	0.124	1058.7	0.0698	1165.3	0.363	1062.2	0.185			
2008-05-26	1133	1	1097	1	1118.9	0.2	1085.8	0.08	1128.5	0.07	1089	0.11			
2008-05-30	1100.6	0.0907	1086.3	0.0893	1086.9	0.115	1076	0.0979	1096.2	0.275	1079.6	0.168			
2008-05-31	1163.3	0.234	1055.1	0.0875	1148.3	0.415	1046	0.0983	1157.9	0.127	1049.4	0.281			
2008-06-02	1169.7	0.216	1057.1	0.931	1154.7	0.212	1046.3	0.0859	1165.4	0.356	1051.1	0.752			
2008-06-03	1173.7	0.104	1057	0.0659	1159.2	0.144	1047.1	0.0724	1168.4	0.514	1049.8	0.352			
2011-05-25	977.7	0.225	837.07	0.419	962.98	0.194	826.46	0.125	972.83	0.315	830.35	0.448			
2012-05-16	978.41	0.0598	774.5	0.059	964.72	0.0619	763.64	0.0698	973.8	0.387	766.15	0.42			
2013-05-09	981.05	0.207	773.85	0.211	967.74	0.22	762.16	0.134	977.75	0.406	766.15	0.804			
2016-03-23	957.71	0.0873	818.43	0.0413	944.44	0.239	805.76	0.152	-	-	-	-			
2018-04-22	962.9	0.0404	757.89	0.0258	948.69	0.815	745.21	0.808	-	-	-	-			
2018-04-24	965.33	0.33	753.46	0.386	951.7	0.193	740.42	0.186	960	1	747	1			

**Table 18.** Dusty sources DS3-DS5 observed with NACO.F.8. *DS11 & DS12*

As for DS9 and DS10, we use K-band data of 2009 to complement the observations in the H- and L-band of 2004. Both sources, DS11 and DS12, can be most likely classified as stellar sources encircled by a dusty envelope. We present the related identification in Fig. 26 and list the magnitudes in Table 35.

F.9. *DS13*

For DS13, we note an increased magnitude-confusion susceptibility throughout the accessible IR bands. The observation of fainter DS sources is even more challenging due to the high stellar density. In Fig. 27, we exhibit the detection of DS8 in the NIR and MIR. Table 36 lists the related magnitude values.

F.10. *DS14 & DS15*

Both sources, DS14 and DS15, are detected in the H-, K-, and L-band but suffer from increased confusion. In Fig. 28, we show data observed in 2004 (H- and L-band) and 2009 (K-band). Especially the K-band detection of DS15 is exposed to the dominant emission of close-by stars, including their respective PSF wings. Despite these challenges, we managed to estimate the K-band magnitude of DS15 for several epochs as indicated in the light curve presented in Fig. 28. The related magnitudes are listed in Table 37.

F.11. *DS16 & DS17*

While Fig. 29 indicates a confusion-free detection of DS17, the close-by and fainter object DS16 experiences the dominant imprint surrounding stars. As for DS14 and DS15, we use data from 2004 (H- and L-band) and 2009

Epoch	DS6				DS7				DS8									
	R.A.	err	R.A.	Dec.	err	Dec.	R.A.	err	R.A.	Dec.	err	Dec.	R.A.	err	R.A.	Dec.	err	Dec.
2002-08-29	804.21	0.122	748.7	0.332	805	0.5	745	0.5	812.61	0.08	738.53	0.136						
2002-08-30	1240.2	0.0891	771.37	0.221	1241	0.5	768	0.5	1247.7	0.535	761.85	0.621						
2003-05-10	992.89	0.128	725.53	0.138	994.67	0.168	721.76	0.135	994.98	0.0835	721.57	0.115						
2004-04-25	796.74	0.323	619.99	0.328	798.56	0.333	616.42	0.335	806.32	0.193	613.13	0.271						
2004-04-26	797	0.5	620	0.5	798	0.5	617	0.5	806.51	0.129	612.94	0.156						
2005-05-13	907.2	0.0847	756.52	0.0934	909.03	0.116	752.49	0.136	916.92	0.107	749.95	0.134						
2006-05-29	861.78	0.213	728.96	0.239	863.53	0.765	724.09	0.339	871.96	0.166	720.41	0.21						
2007-04-01	1161.6	0.2	1030.4	0.984	1163	0.148	1026.1	0.101	1171.1	0.0548	1023.2	0.0627						
2007-05-15	1158.7	0.34	1031.7	17899	1159.4	0.157	1027.1	0.0619	1168.1	0.0398	1024.5	0.0427						
2007-05-16	1130	0.5	1054	0.5	1131	0.5	1051	0.5	1140	0.123	1046.9	0.131						
2007-05-17	1157.4	0.125	1040.1	0.515	1158.4	0.158	1036.4	0.119	1167.3	0.0408	1033.7	0.0578						
2007-05-18	1168.1	0.144	1032.6	0.168	1169.6	0.699	1027.9	0.298	1179	0.118	1023.8	0.12						
2007-05-19	1090	0.764	1023.2	0.69	1090.4	0.0898	1019.3	0.124	-	-	-	-						
2007-05-22	927	0.5	792	0.5	928	1	790	1	936.99	0.0386	785.18	0.0479						
2007-05-23	1175.1	0.25	1062.1	0.25	1176.1	0.251	1058.5	0.288	1185.3	0.0327	1055.2	0.0447						
2008-05-26	1134.4	0.0414	1080.2	0.04	1136.2	0.2	1074.5	0.07	1147.6	0.05	1082.5	0.07						
2008-05-30	1106.1	0.215	1079.8	0.571	1107.3	0.0848	1076	0.0642	1116	0.0446	1072.4	0.166						
2008-05-31	1167.2	0.201	1049.4	0.29	1168.4	0.0693	1045.9	0.0588	1176.5	0.176	1043.2	0.107						
2008-06-02	1175	1	1050	1	1176	1	1047	1	1184.6	0.0547	1043.2	0.0502						
2008-06-03	1178.3	0.122	1050.4	0.47	1179.6	0.0842	1046.8	0.158	1188.3	0.052	1043.9	0.0551						
2011-05-25	983.31	0.0809	830.56	0.238	984.15	0.105	826.74	0.289	993.23	0.0803	824.08	0.115						
2012-05-16	983.65	0.864	769	1	985.23	0.174	764.03	0.274	994.96	0.0706	761.31	0.0853						
2013-05-09	987.23	0.376	768	1	997.67	0.0474	732.72	0.0755	994.38	0.0732	751.09	0.0947						
2016-03-23	964.59	0.162	811.7	0.22	965.77	0.559	808.1	0.266	974.83	0.211	805.25	0.193						
2018-04-22	970	1	752	1	971.13	0.076	748.82	0.134	981	1	745	1						
2018-04-24	972.71	0.278	747.36	0.484	973.13	0.921	744.03	0.77	980.42	0.0492	741.86	0.133						

**Table 19.** Dusty sources DS6-DS8 observed with NACO.

(K-band) for cosmetic reasons. Especially the detection of DS16 demonstrates the challenges of this analysis. While the observation of DS16 is confusion-free in the L-band, the detection in the NIR bands requires the astrometric identification in the MIR band to avoid a false association. Please see Table 38.

#### F.12. *DS18 & DS19*

The observation of DS18 and DS19 is presented in Fig. 30. Due to the close distance to the bright star DS17 (see Fig. 29), the detection of DS18 and DS19 is hindered. Hence, the magnitude-confusion susceptibility is increased. However, we list the related magnitudes for DS18 and DS19 based on the NACO data set observed between 2002 and 2018 in Table 39.

#### F.13. *DS20*

For DS20, we do not find increased confusion due to crowding (Fig. 31). The magnitude-confusion susceptibility is lowered. We list the related multi-wavelength magnitudes in Table 40.

#### F.14. *DS21*

The source DS21 is located close to the E-star E7. Because of the bright emission of the E-stars, the source suffers from blending and dominant PSF wings, although DS21 seems isolated (Fig. 32). Despite the challenges of the identification related to DS21, we identify the source in several epochs and list the magnitude in Table 41.

Epoch	DS9				DS10				DS11					
	R.A.	err	R.A.	Dec. err	Dec.	R.A.	err	R.A.	Dec. err	Dec.	R.A.	err	R.A.	Dec. err
2002-08-29	819.57	0.102	747.94	0.0753	828.36	0.036	749.57	0.036	772.44	0.0615	731.23	0.023		
2002-08-30	1255.3	0.0857	771.47	0.0882	1264.3	0.0153	773.08	0.0141	1208.2	0.0402	754.51	0.0119		
2003-05-10	1008.3	0.254	725.37	0.487	1017.1	0.0386	726.26	0.0362	961.09	0.0171	708.15	0.018		
2004-04-25	812.07	0.11	619.2	0.139	820.87	0.047	620.17	0.0446	764.93	0.0364	602.42	0.0362		
2004-04-26	812.06	0.103	619.42	0.115	820.88	0.0466	620.23	0.0433	764.96	0.0207	602.49	0.0194		
2005-05-13	921.92	0.067	755.87	0.068	930.68	0.0483	756.29	0.038	875.12	0.0346	738.58	0.0219		
2006-05-29	877.02	0.088	725.63	0.087	885.65	0.0353	726.07	0.0355	830.01	0.0375	708.81	0.0371		
2007-04-01	1176.1	0.0599	1028.1	0.0811	1184.7	0.0347	1028.6	0.0339	1129.3	0.0312	1011.6	0.0234		
2007-05-15	1173.2	0.0924	1028.5	0.217	1182.2	0.0555	1029.6	0.0408	1126	0.0619	1012.4	0.0231		
2007-05-16	1144	0.0903	1051.1	0.0603	1153	0.0608	1051.8	0.0718	1097.3	0.0452	1035.1	0.0263		
2007-05-17	1171.6	0.0442	1038.3	0.0411	1180.3	0.018	1038.8	0.02	1124.7	0.0186	1021.8	0.00854		
2007-05-18	1183	0.0931	1028.1	0.087	1191.7	0.0183	1028.7	0.0172	1136.2	0.0194	1011.8	0.0114		
2007-05-19	-	-	-	-	-	-	-	-	-	-	-	-		
2007-05-22	941.33	0.0916	789.78	0.0719	950.02	0.0209	790.41	0.0215	894.57	0.0232	773.37	0.0115		
2007-05-23	1189.8	0.062	1059.7	0.118	1198.3	0.0168	1060.4	0.0155	1143	0.0259	1043.4	0.0191		
2008-05-26	1152.4	0.29	1087	0.297	1160.7	0.04	1086.9	0.04	1105.2	0.0244	1070.6	0.024		
2008-05-30	1120.6	0.186	1077.2	0.184	1128.9	0.0204	1077.1	0.0202	1073.5	0.0518	1060.8	0.0644		
2008-05-31	1180.6	45261	1047.1	0.231	1190.1	0.0642	1047.3	0.0362	1134.5	0.0784	1030.8	0.0309		
2008-06-02	1189	0.488	1047.1	0.294	1198.1	0.0545	1047.5	0.0337	1142.1	0.0383	1031	0.0108		
2008-06-03	1192.7	0.141	1048.2	0.147	1201.2	0.0271	1048.3	0.0263	1145.6	0.0373	1031.9	0.0173		
2011-05-25	997.37	0.181	826.41	0.291	1004.9	0.124	826.06	0.114	950.12	0.0364	810.77	0.0112		
2012-05-16	-	-	-	-	1005.7	0.0337	762.54	0.066	951.12	0.0441	747.82	0.0176		
2013-05-09	1008.4	0.0761	760.85	0.106	1008.3	0.0415	760.71	0.049	954.01	0.0662	746.58	0.0246		
2016-03-23	977.83	0.235	806.76	0.188	984	1	803	1	930.94	0.108	790.04	0.0606		
2018-04-22	982	1	746	1	988.41	0.392	743	0.737	936.61	0.698	729.79	0.559		
2018-04-24	983.32	1	740.96	0.174	984.41	0.355	741.18	0.144	938.45	0.214	724.95	0.059		

**Table 20.** Dusty sources DS9-DS11 observed with NACO.F.15. *DS22*

The detection of DS22 in the H- and K-band is challenging due to the close distance of several surrounding stars (Fig. 33). As demonstrated for DS20 (Fig. 31), the close distance of bright stars does not have to result in lowered detectability. However, due to the low K- and H-band magnitude of DS22, the detection of the source is limited to a few epochs (Fig. 33). The related magnitude is indicated in Table 42.

F.16. *DS23*

Like DS22 (Fig. 33), the source DS23 suffers from close-by stars and increased confusion. The magnitude of the source is listed in Table 43.

F.17. *DS24*

The bright source is located at the eastern edge of the IRS 13 cluster and, therefore, is not affected by the dominant crowding of the inner core region. We detect DS24 without confusion in various epochs (Fig. 35) and list the related magnitude in Table 44.

F.18. *DS25*

Like DS24 (Fig. 35), the source DS25 is located at the edge of the cluster. The chance for confusion is lowered, which is why we detect the source in all analyzed bands (Fig. 36). The related magnitude is listed in Table 45.

Epoch	DS12				DS13				DS14					
	R.A.	err	R.A.	Dec. err	Dec.	R.A.	err	R.A.	Dec. err	Dec.	R.A.	err	R.A.	Dec. err
2002-08-29	778.39	0.0164	733.27	0.0157	819.89	0.0795	737.12	0.0646	820.37	0.0745	732.08	0.035		
2002-08-30	1214.2	0.0204	756.54	0.0141	1255	0.542	761.28	0.352	1256.2	0.0897	755.17	0.103		
2003-05-10	967.2	0.0317	710.15	0.0308	1008.5	0.0983	714.64	0.118	1009.8	0.106	709.02	0.0552		
2004-04-25	770.9	0.0618	604.19	0.0603	812.4	0.0786	609.41	0.0854	814.2	0.0982	603.68	0.0748		
2004-04-26	770.77	0.0226	604.26	0.0214	812.83	0.173	609	0.251	813.83	0.091	603.75	0.0619		
2005-05-13	880.82	0.0318	740.16	0.0304	923.13	0.0847	745.92	0.0698	924.83	0.19	740.44	0.304		
2006-05-29	835.58	0.03	710.14	0.0282	878.05	0.0644	716.71	0.075	880.13	0.0905	710.83	0.0688		
2007-04-01	1134.4	0.0324	1012.6	0.0227	1177.5	0.0228	1019.4	0.032	1179.4	0.0527	1013.7	0.0454		
2007-05-15	1131.4	0.0522	1013.6	0.0243	1174.2	0.109	1020.2	0.0821	1176.4	0.145	1014.4	0.296		
2007-05-16	1102.5	0.0377	1036	0.0239	1145.6	0.113	1043.1	0.118	1147.8	0.0696	1037.6	0.0669		
2007-05-17	1130.2	0.0826	1022.8	0.0333	1173.2	0.0451	1029.7	0.0422	1175.5	0.419	1023.9	0.14		
2007-05-18	1141.3	0.0611	1012.8	0.0258	1184.6	0.048	1019.6	0.0456	1186.4	0.198	1014.3	0.161		
2007-05-19	-	-	-	-	-	-	-	-	-	-	-	-		
2007-05-22	899.67	0.0245	774.34	0.0212	943.27	0.0582	781.19	0.0655	945.31	45047	775.97	0.229		
2007-05-23	1147.9	0.0323	1044.3	0.0274	1191.4	0.0907	1051.2	0.102	1192.8	0.57	1045.8	0.36		
2008-05-26	1110.6	0.025	1071.4	0.024	1154.3	0.089	1078.6	0.09	1156.1	0.06	1072.7	0.06		
2008-05-30	1078.6	0.0395	1061.5	0.0237	1122.6	0.0715	1068.7	0.0719	1124.3	0.0484	1062.9	0.0411		
2008-05-31	1139.2	0.0223	1031.4	0.014	1183.9	0.093	1038.6	0.124	1185.9	0.0352	1033.7	0.045		
2008-06-02	1147	0.0764	1031.7	0.0236	1191.2	0.0631	1039.2	0.0753	1192.9	0.0489	1033.4	0.0477		
2008-06-03	1150.7	0.0221	1032.6	0.0283	1194.8	0.158	1039.7	0.185	1196.4	0.0975	1034	0.0564		
2011-05-25	954.56	0.0407	810.77	0.0395	999.97	0.0261	820.07	0.0278	1002	0.466	814.64	0.237		
2012-05-16	955.18	0.0535	747.54	0.0862	1001.8	0.117	757.12	0.103	1003.4	0.0804	751.12	0.118		
2013-05-09	958.17	0.0493	746.09	0.052	1004.8	0.0492	756.16	0.0371	1007.2	0.0803	750.21	0.166		
2016-03-23	935.18	0.0916	788.87	0.0446	981.95	0.59	800.84	0.806	985.3	0.107	795.28	0.0828		
2018-04-22	939.86	0.591	726.99	0.601	988.94	0.015	741.21	0.0189	991.5	0.047	734.61	0.082		
2018-04-24	942.11	0.095	723.05	0.058	990.97	0.0481	737.03	0.0252	993.38	0.022	730.18	0.02		

**Table 21.** Dusty sources DS12-DS14 observed with NACO.F.19. *DS26*

The source DS26 is affected by the dominant PSF wings of E1, the O supergiant in the core of IRS 13. Therefore, the detection of DS26 is limited to a few epochs (Fig. 37). Please consult Table 46 for the related magnitude values of DS26.

F.20. *DS27*

The bright source DS27 can be observed without confusion in the available data set covering the epochs between 2002 and 2018. The related magnitude is listed in Table 47.

F.21. *DS28*

The source DS28 is located at the northern tip of an apparent elongated L-band feature (Fig. 39) consisting of DS31 and DS33. We detect DS28 without confusion in several bands and epochs. The estimated magnitude is listed in Table 48.

F.22. *DS29*

The source DS29 is located on a north-south axis with DS24 (Fig. 35) and DS25 (Fig. 36). Like the former two sources, DS29 is located at the edge of the IRS 13 cluster and north of X3 (Peißker et al. 2023b). We detect DS29 without confusion (Fig. 40) and indicate the related magnitude in Table 40.

Epoch	DS15				DS16				DS17									
	R.A.	err	R.A.	Dec.	err	Dec.	R.A.	err	R.A.	Dec.	err	Dec.	R.A.	err	R.A.	Dec.	err	Dec.
2002-08-29	-	-	-	-	-	-	831.09	0.0448	735.79	0.0558	838.69	0.0737	729.72	0.0619				
2002-08-30	-	-	-	-	-	-	1266.8	0.0254	759.13	0.0205	1274.1	0.0822	753.06	0.257				
2003-05-10	-	-	-	-	-	-	1019.8	0.0523	712.91	0.055	1027.4	0.0287	706.69	0.0225				
2004-04-25	810.08	0.279	602.35	0.281			823.42	0.0815	607.19	0.081	830.81	0.0639	601.06	0.0476				
2004-04-26	-	-	-	-	-	-	823.81	0.0652	606.89	0.0579	830.81	0.0947	601.16	0.178				
2005-05-13	921	1	739	1			934.02	0.073	743	0.133	941.49	0.0541	737.59	0.0497				
2006-05-29	875.92	0.196	708.92	0.116			888.65	0.0371	713.36	0.0637	896.01	0.108	707.86	0.0866				
2007-04-01	1175	0.0569	1011.6	0.077			1187.7	0.0345	1016	0.033	1194.8	0.277	1010.6	0.444				
2007-05-15	1172.3	0.0565	1012.6	0.0747			1184.7	0.0283	1016.6	0.0432	1191.9	0.061	1011.7	0.178				
2007-05-16	-	-	-	-	-	-	1156.4	0.0783	1038.8	0.0623	1163.5	0.155	1034.6	0.274				
2007-05-17	1171.8	0.0745	1022.9	0.059			1183.5	0.0171	1025.6	0.0282	1190.6	0.123	1021.4	0.278				
2007-05-18	1182.3	0.172	1012.2	0.115			1194.9	0.0239	1016.1	0.0233	1202	0.268	1011	0.159				
2007-05-19	-	-	-	-	-	-	-	-	-	-	-	-	-	-				
2007-05-22	941.45	0.0965	774.18	0.061			953.41	0.0221	777.85	0.0309	960.39	0.078	772.62	0.175				
2007-05-23	1191	1	1044	1			1201.5	0.0165	1047.5	0.0302	1208.9	0.0646	1043.3	0.251				
2008-05-26	1151.4	0.13	1070.6	0.162			1164.2	0.134	1074.6	0.202	1171.3	0.0893	1069.5	0.092				
2008-05-30	1119.8	0.206	1060.8	0.485			1132.3	0.0133	1064.8	0.0182	1139.7	0.0265	1059.6	0.0241				
2008-05-31	-	-	-	-	-	-	1193.6	0.12	1034.1	0.0957	1200.6	0.151	1029.6	0.135				
2008-06-02	1191	1	1032	1			1200.3	0.0544	1035.6	0.0484	1208	0.184	1030.1	0.185				
2008-06-03	1191.7	0.522	1031.7	0.248			1204.4	0.0439	1036.1	0.0668	1211.7	0.116	1031.7	0.132				
2011-05-25	-	-	-	-	-	-	1008.9	0.0563	814.4	0.0856	1016	0.232	810.04	0.13				
2012-05-16	999.73	0.0372	749.53	0.0256			1010	0.0557	751.7	0.0511	1017.2	0.265	747.16	0.136				
2013-05-09	1002.9	0.398	748.4	0.363			1013.7	0.0517	750.74	0.0649	1020.5	0.0227	745.97	0.0193				
2016-03-23	981.45	0.21	793.37	0.158			989.71	0.228	794.81	0.421	997.8	0.0261	790.36	0.0236				
2018-04-22	-	-	-	-	-	-	995.56	1	734.33	0.34	1003.1	0.021	729.85	0.03				
2018-04-24	988.89	0.101	728.67	0.145			-	-	-	-	1005.4	0.021	725.45	0.023				

**Table 22.** Dusty sources DS15-DS17 observed with NACO.F.23. *DS30*

Like DS26 (Fig. 37), the source DS30 is located close to the E-star E1. Due to the brightness of DS30, we detect the source without confusion in various epochs (Fig. 41). In Table 50, we list the related magnitude.

F.24. *DS31*

The source DS31 suffers, like, for example, DS26 (Fig. 37), from the toxic imprint of the core stars of the IRS 13 cluster. This is reflected by a variation of the magnitude in various bands as indicated in Fig. 42. The significance of the detection is lowered since the variation of the individual magnitude values is partially outside of the range of the standard deviation. The related magnitudes are listed in Table 51.

F.25. *DS32*

The source DS32 is located close to the brighter dusty sources of the IRS 13 cluster. Although the chance of confusion is increased due to the amount of close by stars, we detect DS32 in all epochs between 2002 and 2018 (Fig. 43). The related magnitude of DS32 is listed in Table 52.

F.26. *DS33*

As mentioned before, the location of DS33 can be associated with an elongated L-band feature (DS28, Fig. 39). However, this feature is most likely a chance association because we identify the individual components as DS sources (Fig. 44). Please consult Table 53 for the related NIR and MIR magnitudes.

Epoch	DS18				DS19				DS20						
	R.A.	err	R.A.	Dec. err	Dec.	R.A.	err	R.A.	Dec. err	Dec.	R.A.	err	R.A.	Dec. err	Dec.
2002-08-29	844.88		42005	733.7	0.823	0	0	0	0	835.43	0.0321	722.83	0.042		
2002-08-30	1280.1	0.246	755.86	0.612	1275	1	753	1	1271.3	0.0282	746	0.0303			
2003-05-10	1033.3	0.0362	709.79	0.0408	1029	1	706	1	1024.2	0.0343	699.47	0.0461			
2004-04-25	837.46	0.129	603.93	0.382	835.02	0.237	599.78	0.368	828.12	0.0615	593.73	0.0868			
2004-04-26	836.89	0.247	604.02	0.3	832	1	600	1	827.71	0.0695	593.68	0.0881			
2005-05-13	947.73	0.0539	740.28	0.122	-	-	-	-	938.22	0.125	730.57	0.107			
2006-05-29	902.6	0.193	710.4	0.418	899.33	0.252	706.19	0.188	893.45	0.0872	700.51	0.102			
2007-04-01	1201.9	552	1013.1	45231	1198.6	0.175	1009.1	0.219	1192.2	0.063	1003.2	0.0722			
2007-05-15	1198.3	0.0542	1013.4	0.109	1196.1	0.44	1009.2	0.513	1189.5	0.0861	1004.3	0.104			
2007-05-16	1169.7	0.144	1035.6	0.13	1166.3	0.662	1031.7	0.213	1160.9	0.106	1026.9	0.115			
2007-05-17	1196.7	0.0812	1022.4	0.165	1193.8	0.159	1019.5	0.0768	1187.9	0.0834	1013.6	0.1			
2007-05-18	1208.6	0.455	1012.7	0.553	1205.6	0.143	1009.2	0.106	1199.5	0.0517	1003.5	0.0506			
2007-05-19	-	-	-	-	-	-	-	-	-	-	-	-			
2007-05-22	966.77	0.366	774.83	0.483	964.25	0.0853	771.08	0.0695	958.09	0.0442	765.18	0.0563			
2007-05-23	1215.5	0.403	1045	45017	1212.8	0.399	1041.1	0.18	1206.2	0.0299	1035.2	0.0497			
2008-05-26	1178.2	0.2	1071.8	0.4	1176	1	1067	2	1168.7	0.141	1062	0.112			
2008-05-30	1146.3	0.582	1061.1	0.823	-	-	-	-	1136.7	0.0487	1052.2	0.0598			
2008-05-31	1208.4	0.528	1032.4	0.81	1203.9	0.58	1026.8	45079	1198.2	0.079	1022.1	0.0489			
2008-06-02	1216.7	0.052	1040.5	0.0531	1213.8	0.0614	1030.4	0.109	1205.5	0.0934	1022.3	0.111			
2008-06-03	1218	1	1032.9	1	1215.5	0.209	1028.8	0.104	1209.2	0.0432	1023.2	0.0478			
2011-05-25	1023.1	0.756	811.3	0.221	1019.8	0.207	807.49	0.504	1014.2	0.304	802.77	0.104			
2012-05-16	1024.7	0.0532	748.97	0.165	1021.7	0.104	745.13	0.0894	1014.9	0.0545	739.29	0.0486			
2013-05-09	1028	1	747	1	1026	1	742	1	1018.3	0.0678	737.92	0.0563			
2016-03-23	1005.4	0.0491	792.05	0.0802	1002.5	0.0776	787.07	0.117	996.28	0.0443	782.35	0.0276			
2018-04-22	1011.7	1	732.4	1	1008.4	0.249	726.21	0.331	1001.8	0.043	721.75	0.053			
2018-04-24	1013.2	0.125	726.97	0.168	1010.4	0.125	722.29	0.194	1004.2	0.015	717.51	0.015			

**Table 23.** Dusty sources DS18-DS20 observed with NACO.

Epoch	DS21				DS22				DS23						
	R.A.	err	R.A.	Dec. err	Dec.	R.A.	err	R.A.	Dec. err	Dec.	R.A.	err	R.A.	Dec. err	Dec.
2002-08-29	826.01	0.116	715.61	0.0884	811.52	0.182	726.4	0.0594	780.03	0.16	721.22	0.286			
2002-08-30	1262	0.131	738.9	0.13	1247.5	0.189	749.76	0.0447	1216.5	0.36	744.14	0.45			
2003-05-10	1015.4	0.14	692.3	0.111	1000.7	0.155	703.49	0.061	969.52	0.0683	698.48	0.132			
2004-04-25	818.38	0.184	586.9	0.106	804.19	0.206	597.79	0.207	773.4	0.0905	593	0.107			
2004-04-26	819.06	0.206	587.05	0.0998	804.26	0.178	598.14	0.0704	772.94	0.147	592.75	0.177			
2005-05-13	929.3	0.203	723.24	0.121	914.48	0.257	734.44	0.141	883.21	0.214	729.35	0.193			
2006-05-29	884.49	0.267	693.62	0.109	869.5	0.602	705.11	0.645	838.17	0.131	699.84	0.203			
2007-04-01	1184.4	0.0869	996.26	0.0471	1168.7	0.275	1008	0.0585	1136.7	0.133	1001.8	0.391			
2007-05-15	1181.2	0.121	997.32	0.0656	1165.7	0.115	1008.9	0.117	1132.9	0.256	1002	0.58			
2007-05-16	1153.5	0.125	1019.8	0.118	1138	0.151	1031.6	0.0804	1103.6	0.277	1025.1	0.586			
2007-05-17	1180.4	0.159	1006.5	0.0866	1165.3	0.171	1018.2	0.112	1132.3	0.267	1012.1	0.82			
2007-05-18	1191.8	0.113	996.49	0.0701	1176.3	0.156	1008.1	0.0456	1143.4	0.181	1001.2	0.785			
2007-05-19	-	-	-	-	-	-	-	-	-	-	-	-			
2007-05-22	949.79	0.104	758.26	0.117	934.54	0.117	769.99	0.047	901.72	0.369	763.48	0.946			
2007-05-23	1198.4	0.0849	1028.2	0.0776	1182.8	0.101	1039.7	0.136	1150	1	1032	1			
2008-05-26	1160.9	0.15	1055.1	0.08	1145.2	0.3	1066.8	0.118	1113.1	0.142	1061.6	0.22			
2008-05-30	1129.5	0.117	1045.4	0.0845	1113.6	0.124	1057.1	0.0951	1080.6	0.132	1051	0.375			
2008-05-31	1190.7	0.212	1015.4	0.0718	1174.5	0.168	1027.7	0.0941	1140.6	0.844	1019.8	0.45			
2008-06-02	1198.5	0.0969	1015.5	0.0765	1182.5	0.355	1027.6	0.0862	1148.6	0.276	1020.6	0.828			
2008-06-03	1201.6	0.109	1016.5	0.0673	1186	0.101	1028.3	0.052	1152.4	0.333	1020.1	1			
2011-05-25	1006.6	0.0764	796.04	0.0765	991.08	0.143	807.95	0.0719	956.75	0.56	801	1			
2012-05-16	1007.2	0.222	733.16	0.111	992.11	0.153	745.49	0.0667	957.69	0.555	739.01	1			
2013-05-09	1011.1	0.0696	731.87	0.0409	994.87	0.242	744.18	0.1	960.97	0.474	737.12	0.367			
2016-03-23	988.95	0.0444	776.23	0.0318	972.45	0.233	789.01	0.0742	937.27	0.349	781.06	0.44			
2018-04-22	994.91	0.095	715.37	0.27	978.32	0.161	728.42	0.15	941.9	1	718.62	2			
2018-04-24	997.04	0.079	711.32	0.165	980.13	0.251	724.09	0.107	945.45	0.483	717.15	0.47			

**Table 24.** Dusty sources DS21-DS23 observed with NACO.



Epoch	DS24				DS25				DS26						
	R.A.	err	R.A.	Dec. err	Dec.	R.A.	err	R.A.	Dec. err	Dec.	R.A.	err	R.A.	Dec. err	Dec.
2002-08-29	-	-	-	-	-	776.07	18629	701.27	0.951	790.11	0.118	699.64	0.127		
2002-08-30	1213	0.456	733.99	0.516	1211	1	725	1	1225.9	0.15	722.78	0.133			
2003-05-10	966	0.5	687	0.5	964.53	0.0737	678.91	0.0643	979.01	0.506	676.56	0.0989			
2004-04-25	769.59	0.203	581.31	0.317	768.23	0.168	573.24	0.12	782.48	0.0989	570.97	0.0644			
2004-04-26	770	0.5	582	0.5	767.77	0.0881	573.24	0.114	782.22	0.245	570.94	0.105			
2005-05-13	879.27	0.327	716.87	0.624	878.57	0.128	709.17	0.207	892.41	0.299	707.26	0.117			
2006-05-29	834.43	0.0807	688.04	0.134	833.31	0.315	679.98	0.385	847.54	0.047	677.17	0.0361			
2007-04-01	1133.9	0.164	991.25	0.155	1131.5	0.0739	982.25	0.108	1146.3	0.0469	980.14	0.0297			
2007-05-15	1130.6	0.115	992.38	0.206	1128.7	0.0627	983.15	0.124	1143.5	0.242	981.26	0.063			
2007-05-16	1102.7	0.768	1015	0.672	1100	0.5	1006	0.5	1114.3	0.843	1004.4	0.341			
2007-05-17	1129.4	0.0922	1001.5	0.0933	1127.7	0.0793	992.56	0.0634	1147.7	0.0671	993.41	0.148			
2007-05-18	1140.3	0.693	990.59	0.315	1139.1	0.516	982.14	0.189	1153.7	0.345	980.13	0.125			
2007-05-19	-	-	-	-	-	-	-	-	-	-	-	-			
2007-05-22	900	1	753	1	896.92	0.14	744.04	0.0981	911.9	0.0775	742.02	0.0343			
2007-05-23	1148	1	1023	1	1146	0.875	1014.1	0.761	1159.4	0.4	1012.3	0.292			
2008-05-26	1109	0.065	1049.4	0.1	1107.9	0.12	1041.4	0.14	1122.3	0.0938	1039.4	0.0984			
2008-05-30	1077.8	0.186	1040.3	0.178	1076.1	0.372	1031.8	0.183	1090.6	0.0572	1029.3	0.0314			
2008-05-31	1138.4	0.468	1010.9	0.205	1137.1	0.117	1001.7	0.322	1151.5	0.248	999.39	0.0841			
2008-06-02	1145.9	0.686	1010.9	0.444	1144.2	0.187	1001.8	0.327	1159.8	0.331	999.35	0.0898			
2008-06-03	1150.5	0.0997	1012.1	0.105	1147.6	0.0938	1002.7	0.0901	1162.8	0.227	1000.5	0.068			
2011-05-25	954	1	790	1	952.16	0.144	781.95	0.0778	967.08	0.17	779.59	0.0859			
2012-05-16	954.87	0.0961	727.35	0.126	952.72	0.0758	718.88	0.205	967.42	1	716.84	0.3			
2013-05-09	957.14	0.0226	725.74	0.0208	955.48	0.0911	718.06	0.0858	970.02	0.602	715.61	0.17			
2016-03-23	933.97	0.0344	769.41	0.0194	933.07	0.725	761.84	0.202	947.52	0.166	759.77	0.216			
2018-04-22	938.75	0.021	708.34	0.021	937.93	1	701.08	1	952.38	0.277	699.15	0.173			
2018-04-24	941.04	0.0396	704.25	0.0359	940.72	0.359	696.36	0.147	954.33	0.369	964.82	0.692			

**Table 25.** Dusty sources DS24-DS26 observed with NACO.

Epoch	DS27				DS28				DS29			
	R.A.	err	R.A.	Dec. err	R.A.	err	R.A.	Dec. err	R.A.	err	R.A.	Dec. err
2002-08-29	812.13	0.4	737.12	0.66	781.45	0.336	715.13	0.411	772.6	687.3	0.11	0.23
2002-08-30	1248	0.33	760.76	0.26	1215	1	739	1	1208.1	710.94	0.09	0.06
2003-05-10	1000.8	0.08	714.58	0.11	369.65	0.249	691.95	0.142	961.54	664.01	0.08	0.77
2004-04-25	804.67	0.13	608.42	0.14	773	1	587	1	765.05	558.44	0.06	0.05
2004-04-26	804.7	0.13	608.56	0.14	772.75	0.603	587.54	0.261	765.09	558.46	0.08	0.07
2005-05-13	915.13	0.12	744.33	0.24	883	1	724	1	875.04	694.48	0.08	0.06
2006-05-29	870.14	0.11	714.39	0.18	838.76	0.224	692.96	0.221	829.74	664.34	0.23	0.58
2007-04-01	899.22	0.10	746.71	0.30	1136.9	0.365	996.67	0.25	861.87	705.18	0.29	0.12
2007-05-15	-	-	-	-	1133.3	0.406	998.16	0.598	-	-	-	-
2007-05-16	-	-	-	-	1104	1	1020	1	-	-	-	-
2007-05-17	-	-	-	-	1132.2	0.435	1007.6	0.816	-	-	-	-
2007-05-18	-	-	-	-	1143	1	997	1	-	-	-	-
2007-05-19	-	-	-	-	-	-	-	-	-	-	-	-
2007-05-22	934.74	0.06	778.68	0.08	901.6	45658	758.67	0.344	896.04	736.98	0.32	0.24
2007-05-23	1183.1	0.06	1048.7	0.07	1151.2	0.303	1027.8	0.182	1145	1007.5	1	1
2008-05-26	875.38	0.77	805.8	0.21	1112.4	0.348	1056	0.153	837.52	764.24	0.11	0.1
2008-05-30	-	-	-	-	1080.8	0.0448	1046.1	0.454	-	-	-	-
2008-05-31	-	-	-	-	1141	1	1016	1	-	-	-	-
2008-06-02	-	-	-	-	1149.4	0.193	1016.1	0.368	-	-	-	-
2008-06-03	-	-	-	-	1153.8	0.673	1016.9	0.288	-	-	-	-
2011-05-25	882.54	0.09	708.52	0.05	957.5	0.248	795.85	0.199	844.37	667.22	0.12	0.1
2012-05-16	991.46	0.12	752.45	0.05	957.73	0.523	733.9	0.203	953.32	710.75	0.08	0.2
2013-05-09	994.12	0.22	751.14	0.13	960.14	0.731	733.12	0.168	956.39	710.13	0.08	0.11
2016-03-23	971.33	0.21	794.48	0.09	937.11	0.514	777.51	0.892	933.37	753.72	0.19	0.11
2018-04-22	907.13	0.10	659.31	0.24	942.56	0.448	716.18	0.508	868.76	620.78	0.17	0.35
2018-04-24	816.18	0.11	771.9	0.09	944.69	0.178	711.86	0.11	778.26	731.67	0.12	0.1

**Table 26.** Dusty sources DS27-DS29 observed with NACO.

Epoch	DS30				DS31				DS32				DS33						
	R.A.	err	R.A.	Dec. err	Dec.	R.A.	err	R.A.	Dec. err	Dec.	R.A.	err	R.A.	Dec. err	Dec.	R.A.	err	R.A.	Dec. err
2002-08-29	792.35	690.38	0.05	0.15	793.05	711.58	0.38	0.15	780.49	721.44	0.11	0.16	783.52	713.28	0.18	0.51			
2002-08-30	1228.4	713.99	0.31	0.13	1228.5	734.73	0.48	0.15	1216.2	744.45	0.16	0.24	1218.9	736.46	0.11	0.22			
2003-05-10	980.6	667.73	0.31	0.35	981.44	687.99	0.16	0.35	969.62	698.43	0.08	0.1	972.22	689.99	0.11	0.16			
2004-04-25	785.01	561.78	0.06	0.09	784.94	582.35	0.14	0.1	773.32	592.86	0.07	0.09	775.55	584.97	0.06	0.11			
2004-04-26	785.02	561.77	0.05	0.11	784.87	582.37	0.13	0.1	773.2	592.92	0.08	0.1	775.35	585.34	0.09	0.16			
2005-05-13	875.04	694.48	0.08	0.06	894.84	717.9	0.35	0.94	882.99	729.18	0.11	0.1	885.91	720.75	0.12	0.21			
2006-05-29	850.44	667.83	0.05	0.08	849.62	689.18	0.14	0.24	838.11	699.61	0.07	0.11	840.57	691.4	0.09	0.18			
2007-04-01	879.19	701.06	0.05	0.09	879.18	722.46	0.11	0.22	867.06	732.18	0.33	0.43	869.77	723.58	0.17	0.33			
2007-05-15	-	-	-	-	-	-	-	-	-	-	-	-	-	-	-	-			
2007-05-16	-	-	-	-	-	-	-	-	-	-	-	-	-	-	-	-			
2007-05-17	-	-	-	-	-	-	-	-	-	-	-	-	-	-	-	-			
2007-05-18	-	-	-	-	-	-	-	-	-	-	-	-	-	-	-	-			
2007-05-19	-	-	-	-	-	-	-	-	-	-	-	-	-	-	-	-			
2007-05-22	914.92	732.45	0.06	0.15	913.96	754.4	0.19	0.42	902.04	763.65	0.16	0.45	904.87	756.03	0.11	0.18			
2007-05-23	1163.5	1001.9	0.07	0.14	1162	1024	0.11	0.43	1150.6	1033.6	0.4	0.49	1153.1	1026.1	0.11	0.17			
2008-05-26	855.37	759.97	0.04	0.08	854.71	780.73	0.14	0.28	843.48	791.47	0.21	0.3	845.66	783.38	0.18	0.22			
2008-05-30	-	-	-	-	-	-	-	-	-	-	-	-	-	-	-	-			
2008-05-31	-	-	-	-	-	-	-	-	-	-	-	-	-	-	-	-			
2008-06-02	-	-	-	-	-	-	-	-	-	-	-	-	-	-	-	-			
2008-06-03	-	-	-	-	-	-	-	-	-	-	-	-	-	-	-	-			
2011-05-25	861.91	663.14	0.08	0.16	861.28	684.15	0.23	0.12	848.99	693.74	0.33	0.12	852.28	686.26	0.12	0.22			
2012-05-16	970.66	707.61	0.13	0.1	970.18	729.19	0.23	0.44	958.45	738.6	0.25	0.52	961.01	730.87	0.15	0.28			
2013-05-09	973.47	706.72	0.13	0.09	972.99	727.45	0.07	0.05	961.13	737.9	0.12	0.13	964.05	729.66	0.08	0.16			
2016-03-23	950.6	750.81	0.08	0.15	949.7	770.57	0.41	0.71	936.74	778.47	0.76	0.15	941.17	773.2	0.14	0.44			
2018-04-22	887.54	612.9	0.13	0.44	885.67	638.42	0.24	0.28	872.07	645.23	0.31	0.3	875.86	642.45	0.13	0.31			
2018-04-24	795.38	728.79	0.2	0.07	795.01	749.25	0.07	0.05	782	758	1	1	785.93	751.05	0.1	0.25			

**Table 27.** Dusty sources DS30-DS33 observed with NACO.

	mean	median	std
H-band	14.40	14.49	0.15
K-band	12.37	12.23	0.50
L-band	10.13	10.19	0.33

**Table 28.** Estimated magnitudes for DS1 using multi-wavelength observations carried out with NACO between 2002 and 2018.

	mean	median	std
L-band (DS2)	12.60	12.54	0.24
L-band (DS3)	12.30	12.19	0.30

**Table 29.** Estimated magnitudes for DS2 and DS3 using L-band observations carried out with NACO between 2002 and 2018.

	mean	median	std
H-band	18.27	18.20	0.59
K-band	15.71	15.56	0.35
L-band	14.03	14.62	1.41

**Table 30.** Estimated magnitudes for DS4 using multi-wavelength observations carried out with NACO between 2002 and 2018.

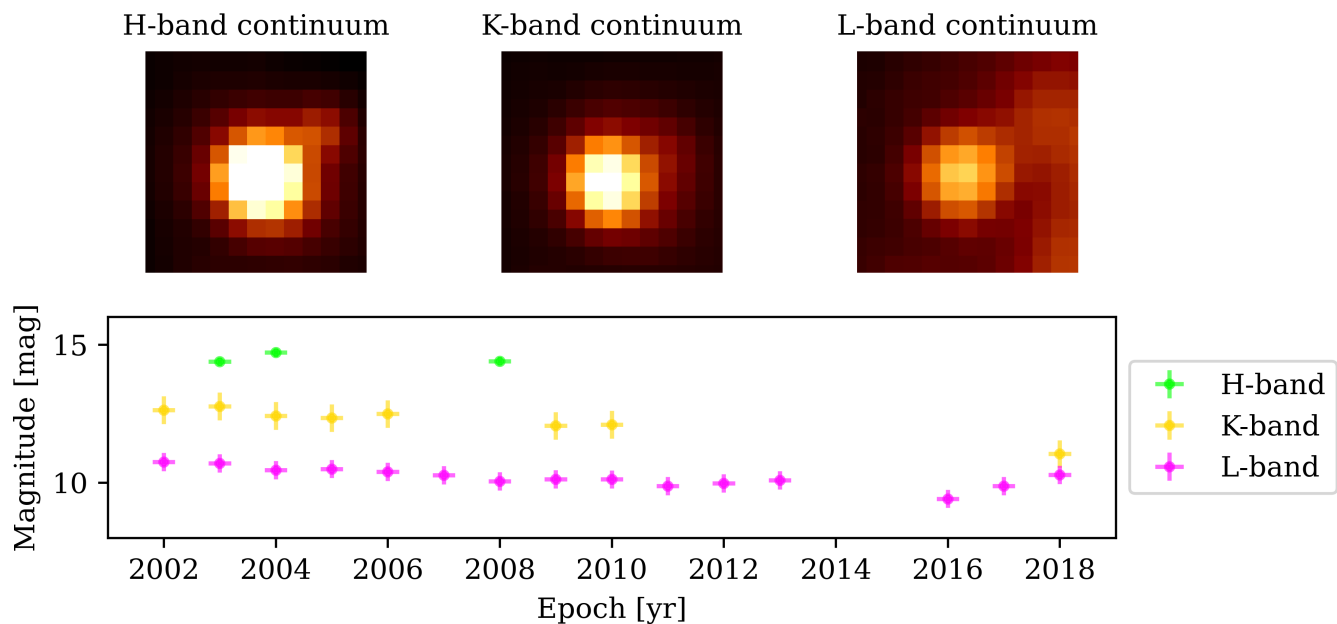


**Figure 19.** Multi-wavelength identification of DS1 with NACO (see Fig. 3, Fig. 18, and Fig. 17). The lower subplot displays the light curve with a fairly constant magnitude distribution between 2002 and 2018.

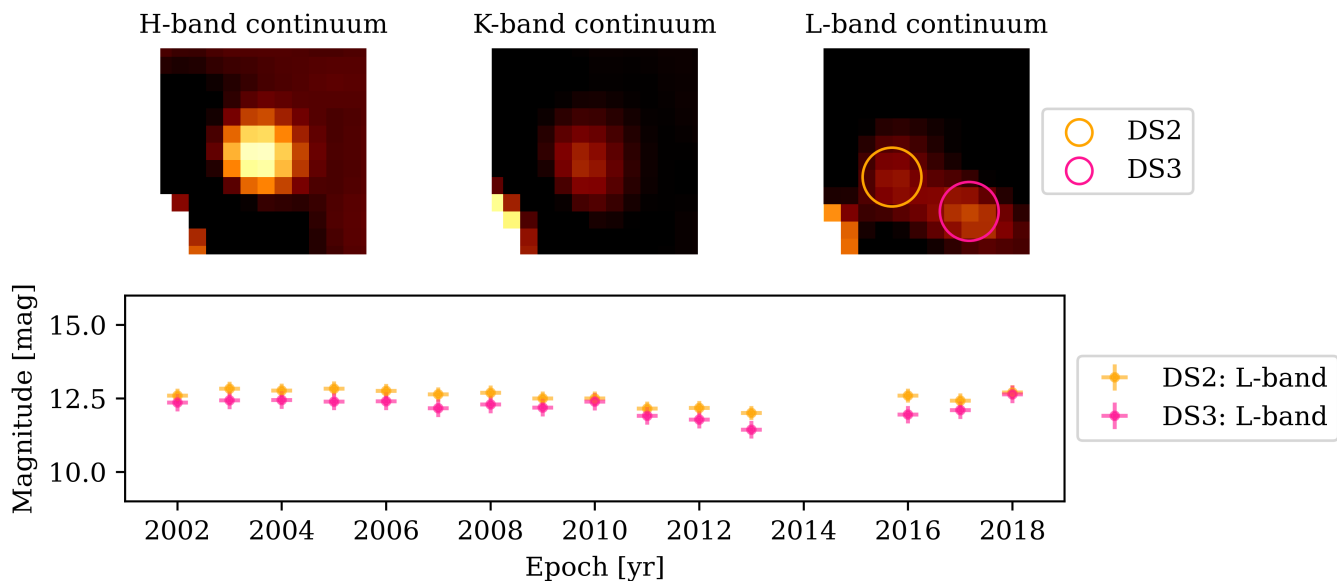


**Figure 20.** Detection of DS2 and DS3 observed with NACO. Both sources are located between DS1 and the star shown in the H- and K-band continuum subplots. As implied, no NIR counterpart of DS2 and DS3 can be detected above the noise. If there are NIR counterparts, the detection is hampered due to the PSF wings of the two stars shown in the H- and K-band continuum subplots.

	mean	median	std
L-band	14.37	15.08	1.68

**Table 31.** Estimated magnitudes for DS5 using multi-wavelength observations carried out with NACO between 2002 and 2018.

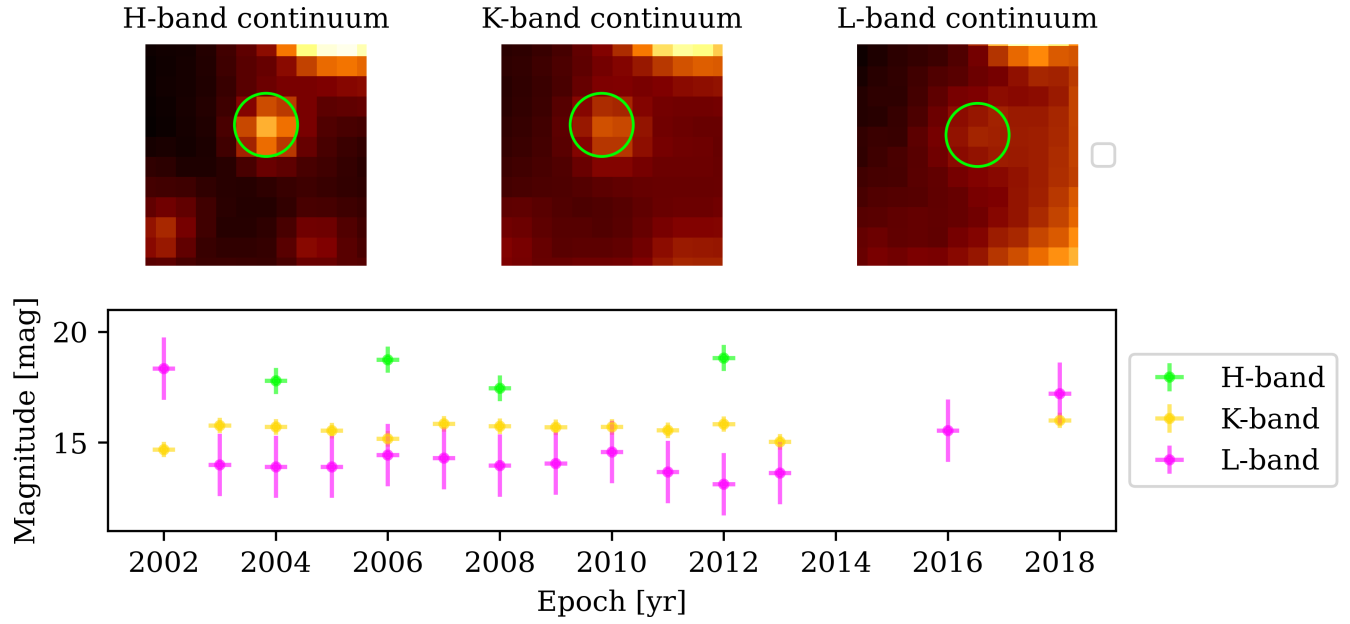


**Figure 21.** Detection of DS4 in the H-, K-, and L-band close to DS1 (upper right boundary of the images).

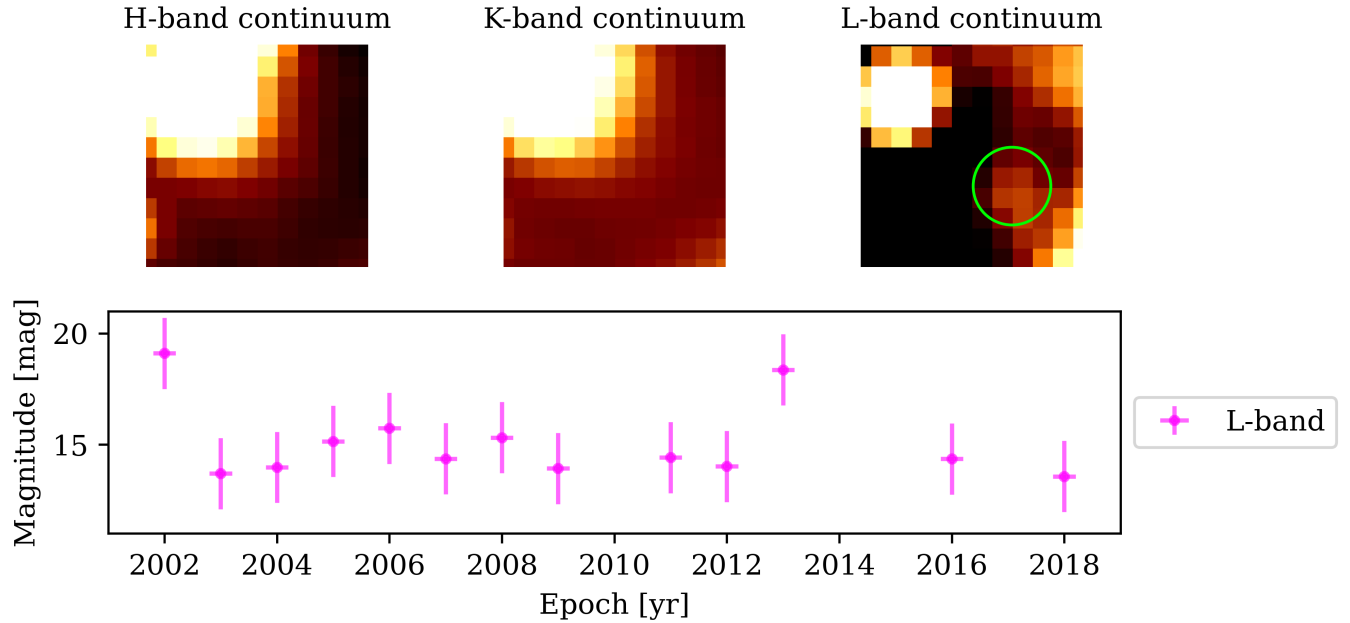


**Figure 22.** Dusty source DS5 close to DS1 that is located in the upper left corner of the subplots. We mark DS5 with a lime-colored circle. Due to the dominant PSF of DS1, the detection of DS5 is challenging. We estimate a median L-band magnitude of  $14.36 \pm 1.68$ . Despite the two outliers in 2002 and 2013, the L-band magnitude is constant inside the uncertainty range.

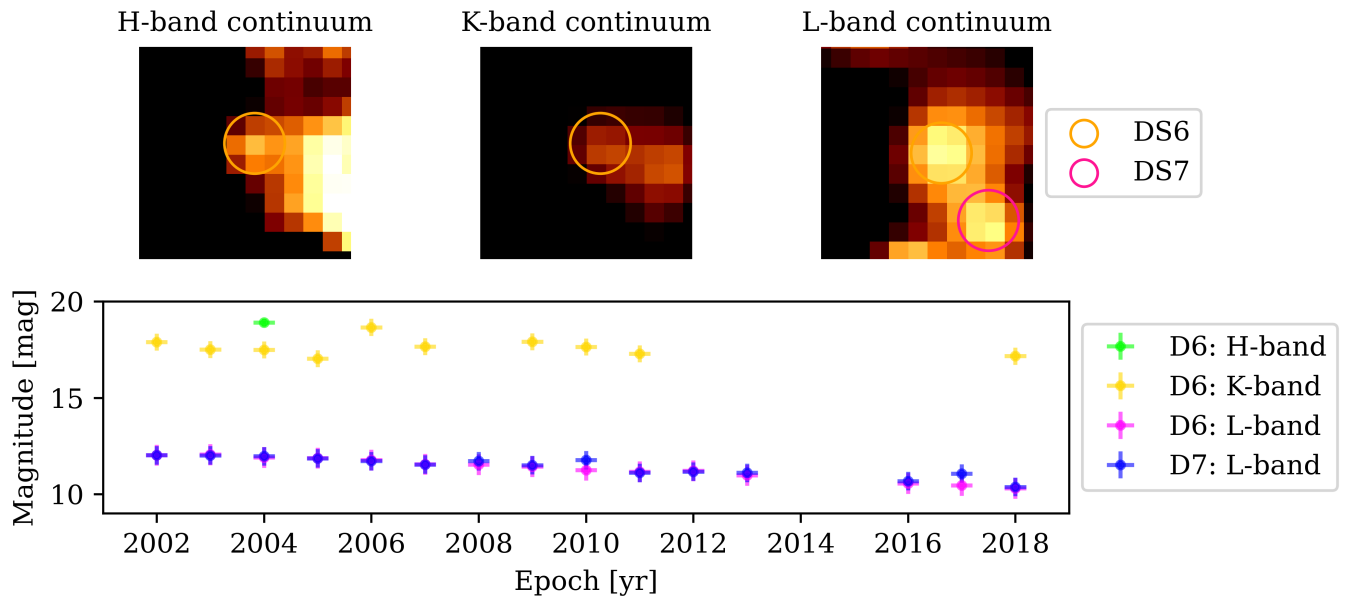


**Figure 23.** Multi-wavelength detection of DS6 and DS7 as observed with NACO.

	mean	median	std
H-band (DS6)	18.91	18.91	0.00
K-band (DS6)	17.62	11.62	0.44
L-band (DS6)	11.43	11.33	0.54
L-band (DS7)	11.54	11.44	0.48

**Table 32.** Estimated magnitudes for DS6 and DS7 using multi-wavelength observations carried out with NACO between 2002 and 2018.

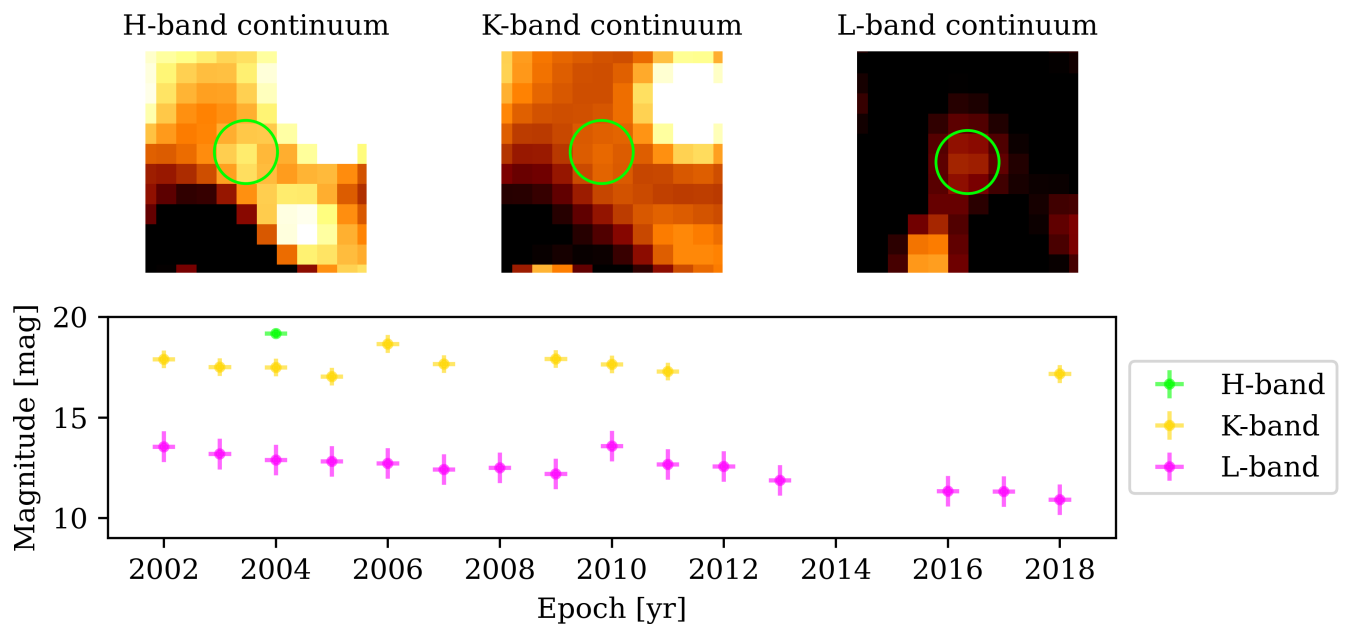


**Figure 24.** Multi-wavelength observation of DS8 with NACO.

	mean	median	std
H-band	19.17	19.17	0.00
K-band	17.57	17.62	0.44
L-band	12.56	12.43	0.76

**Table 33.** Estimated magnitudes for DS8 using multi-wavelength observations carried out with NACO between 2002 and 2018.

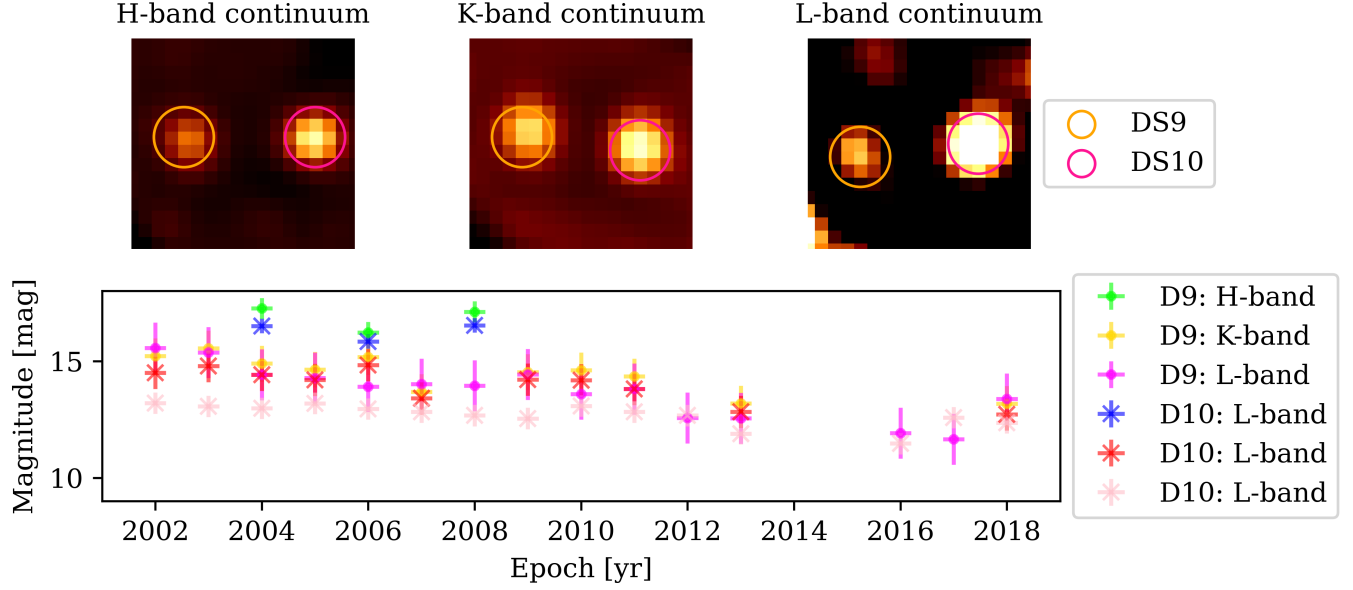


**Figure 25.** Detection of DS9 and DS10 with NACO.

	mean	median	std
H-band (DS9)	17.11	16.86	0.45
K-band (DS9)	14.61	14.45	0.76
L-band (DS9)	13.91	13.69	1.09
H-band (DS10)	16.50	16.29	0.31
K-band (DS10)	14.19	13.98	0.69
L-band (DS10)	12.82	12.68	0.46

**Table 34.** Estimated magnitudes for DS9 and DS10 using multi-wavelength observations carried out with NACO between 2002 and 2018.

	mean	median	std
H-band (DS11)	14.22	14.16	0.35
K-band (DS11)	12.10	11.82	0.70
L-band (DS11)	10.46	10.29	0.64
H-band (DS12)	14.04	14.03	0.36
K-band (DS12)	11.86	11.60	0.72
L-band (DS12)	10.23	10.05	0.60

**Table 35.** Estimated magnitudes for DS11 and DS12 using multi-wavelength observations carried out with NACO between 2002 and 2018.

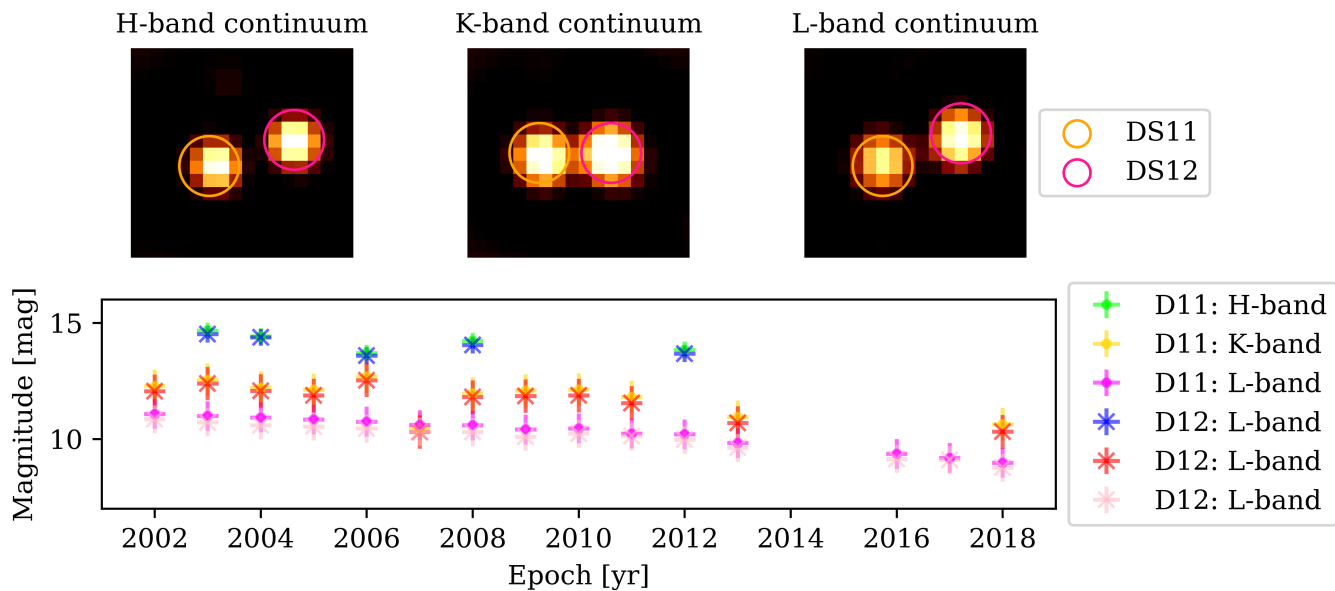


Figure 26. Identification of DS11 and DS12 in various bands.

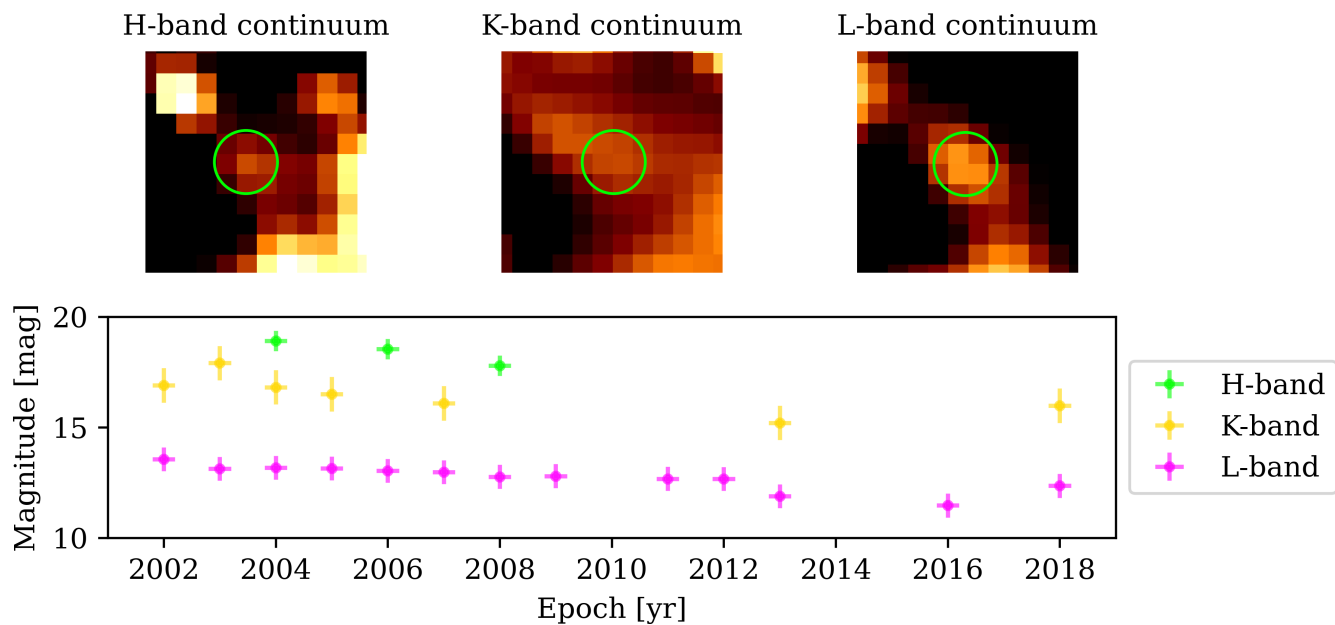
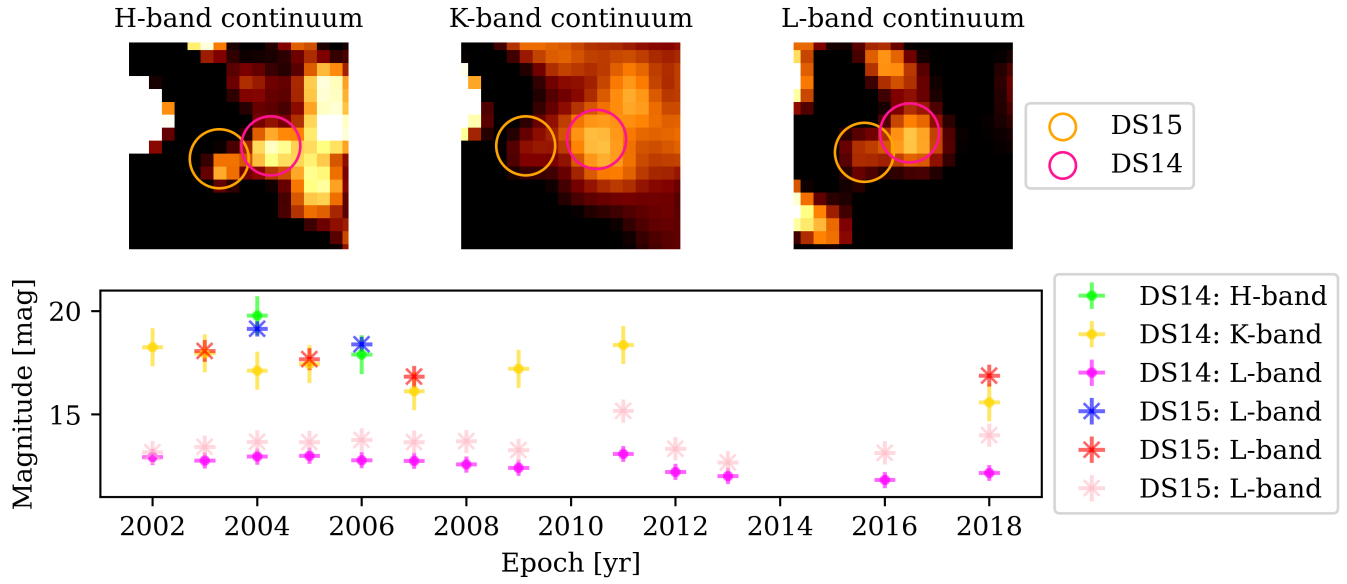


Figure 27. Marked DS13 observed in the H-, K-, and L-band, demonstrating the high confusion reflecting the exceptionally high stellar core density.

	mean	median	std
H-band	18.55	18.42	0.46
K-band	16.51	16.49	0.78
L-band	12.80	12.74	0.54

Table 36. Estimated magnitudes for DS13 using multi-wavelength observations carried out with NACO between 2002 and 2018.





**Figure 28.** Observation of DS14 and DS15 in the H-, K-, and L-band.

	mean	median	std
H-band (DS14)	18.84	18.84	0.94
K-band (DS14)	17.33	17.25	0.92
L-band (DS14)	12.76	12.58	0.39
H-band (DS15)	18.77	18.77	0.37
K-band (DS15)	17.28	17.36	0.53
L-band (DS15)	13.65	13.58	0.56

**Table 37.** Estimated magnitudes for DS14 and DS15 using multi-wavelength observations carried out with NACO between 2002 and 2018.

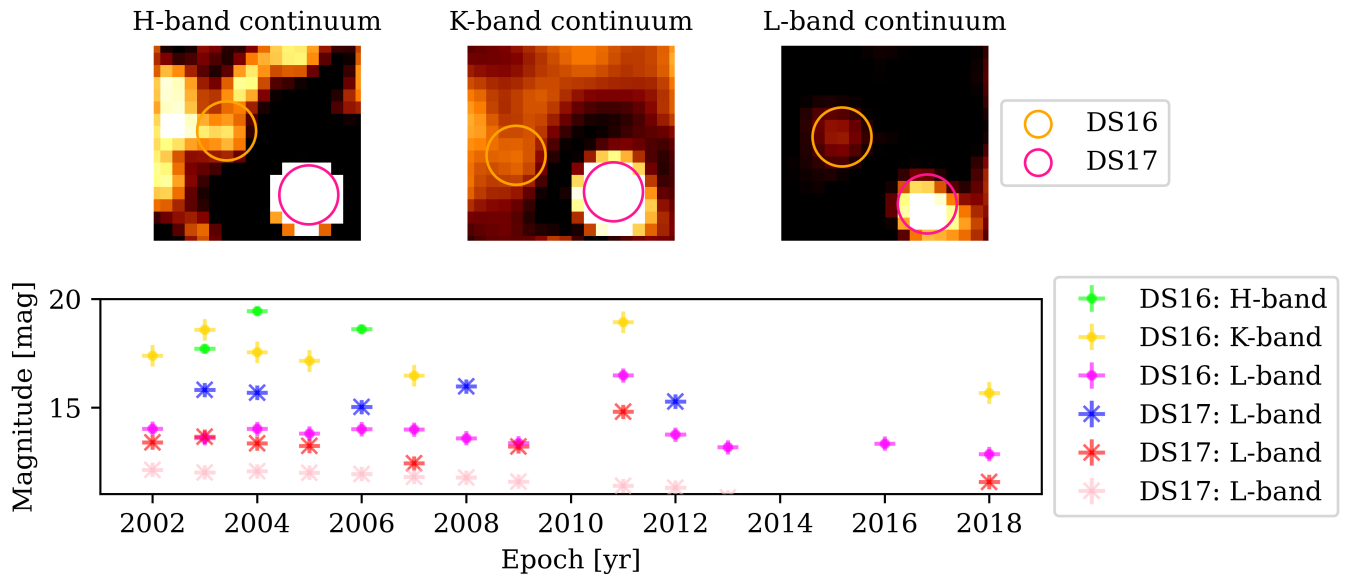


**Figure 29.** Detection of DS16 and DS17 in the NIR and MIR with NACO. We use data from 2004 (H- and L-band) and 2009 (K-band) which is reflected in minor offsets between the two presented sources.

	mean	median	std
H-band (DS16)	18.61	18.59	0.71
K-band (DS16)	17.39	17.39	1.05
L-band (DS16)	13.75	13.83	0.83
H-band (DS17)	15.68	15.55	0.35
K-band (DS17)	13.28	13.19	0.87
L-band (DS17)	11.76	11.47	0.64

**Table 38.** Estimated magnitudes for DS16 and DS17 using multi-wavelength observations carried out with NACO between 2002 and 2018.

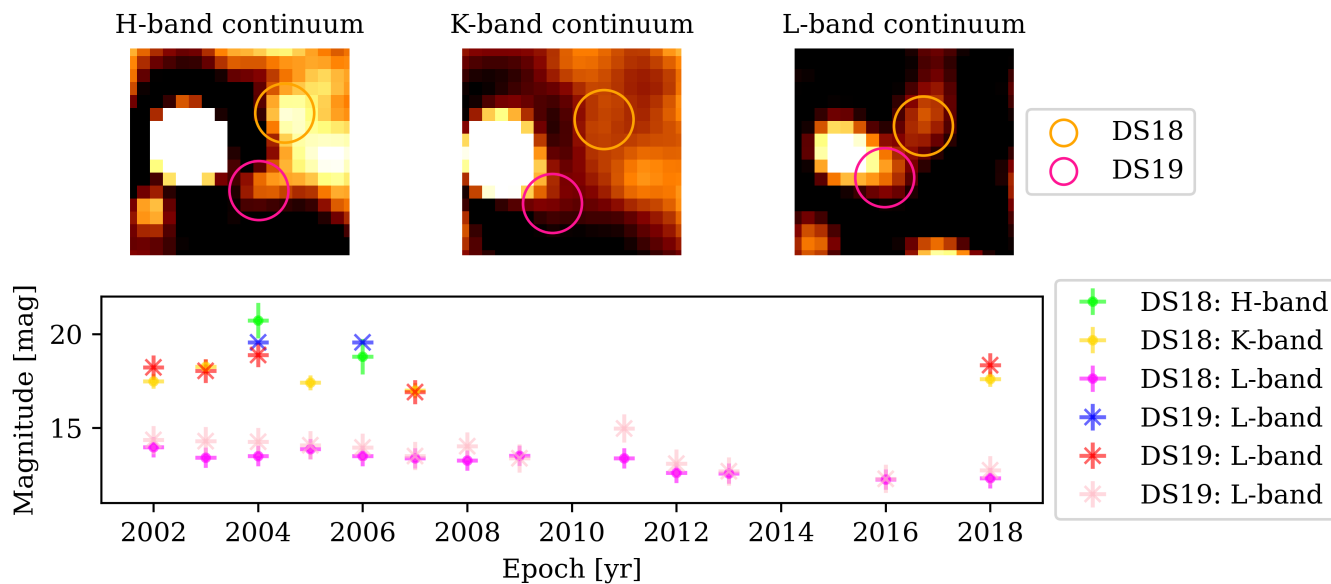


**Figure 30.** Multi-wavelength detection of DS18 and DS19 in the H-,K-, and L-band.

	mean	median	std
H-band (DS18)	19.75	19.75	0.95
K-band (DS18)	17.49	17.54	0.40
L-band (DS18)	13.39	13.19	0.54
H-band (DS19)	19.55	19.55	0.01
K-band (DS19)	18.23	18.08	0.64
L-band (DS19)	13.95	13.66	0.75

**Table 39.** Estimated magnitudes for DS18 and DS19 using multi-wavelength observations carried out with NACO between 2002 and 2018.

	mean	median	std
H-band	18.67	18.67	0.15
K-band	15.81	15.71	0.85
L-band	13.58	13.32	0.72

**Table 40.** Estimated magnitudes for DS20 using multi-wavelength observations carried out with NACO between 2002 and 2018.

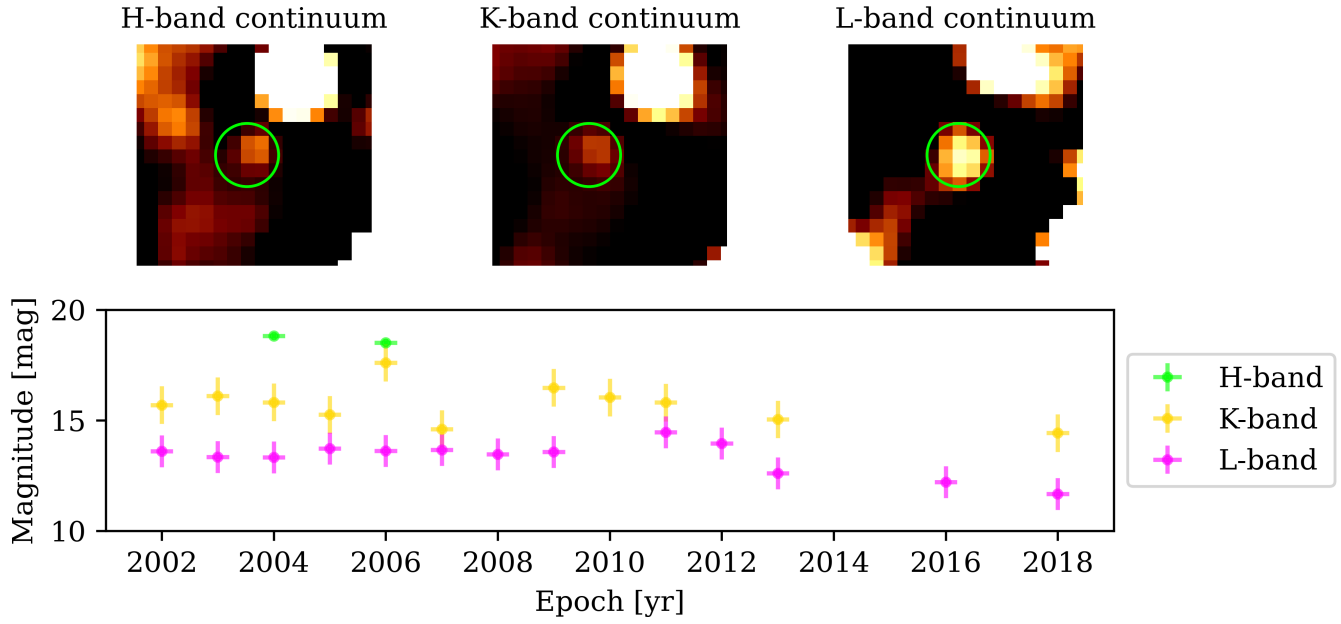


Figure 31. Observation of DS20 close to the bright star DS17 (Fig. 29).

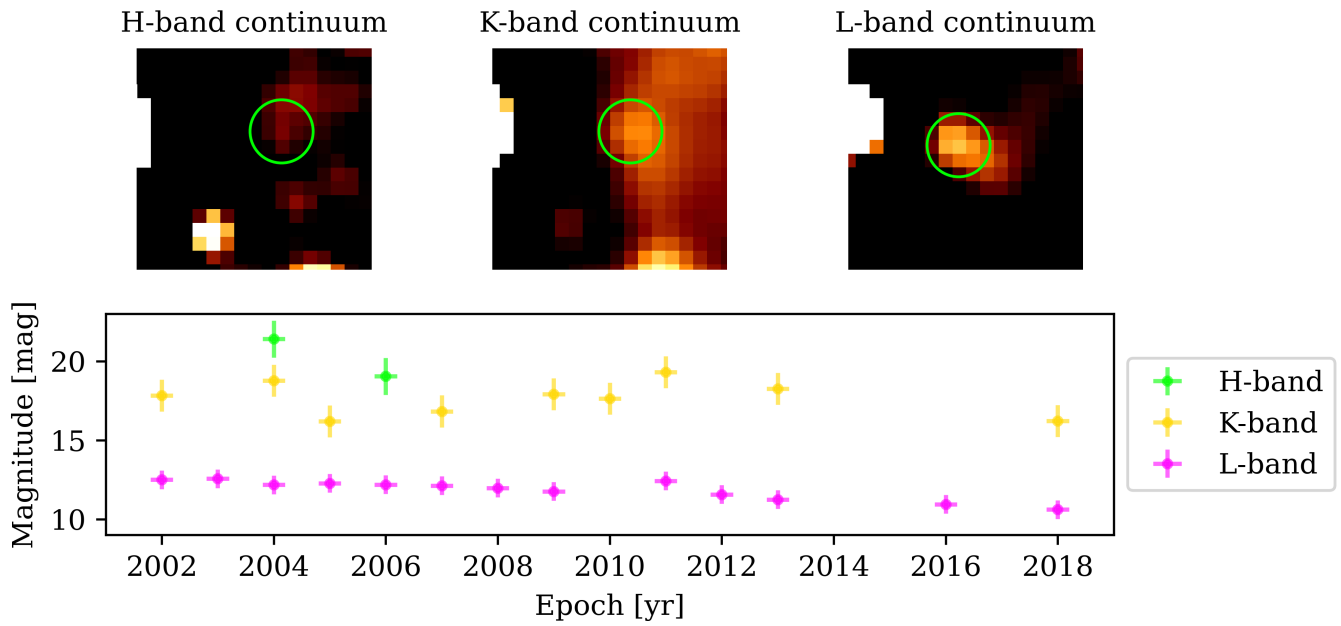
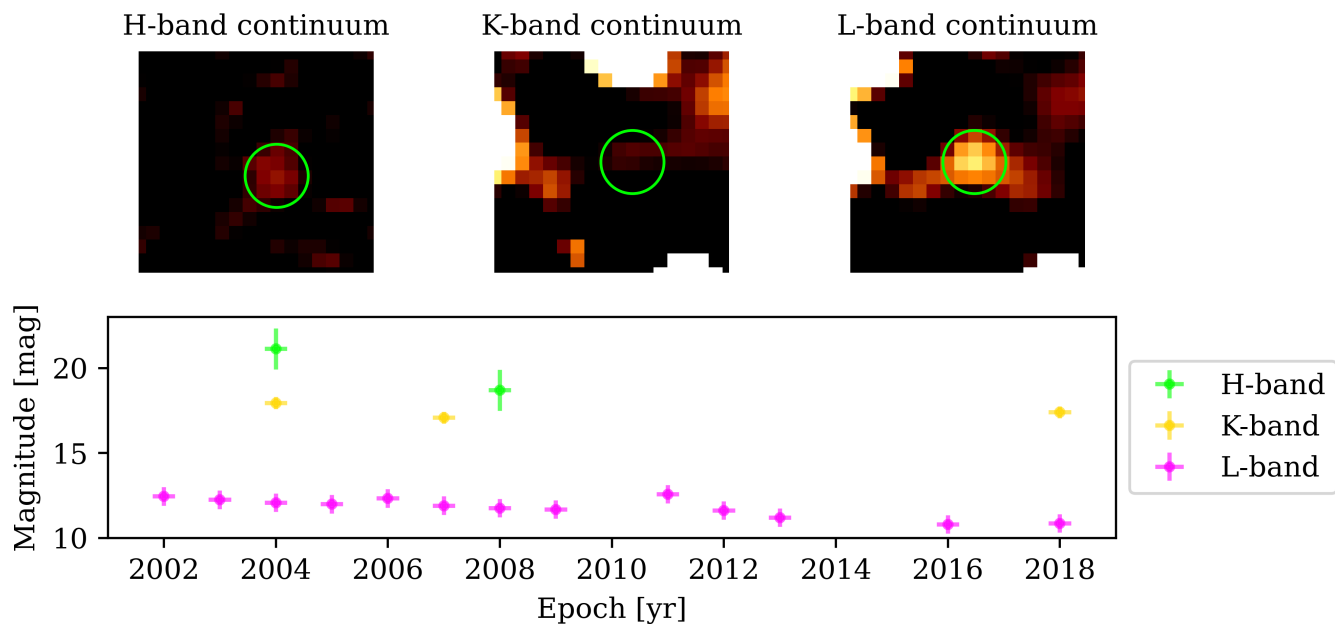


Figure 32. Detection of the source DS21 close to E7.

	mean	median	std
H-band	20.23	20.23	1.17
K-band	17.83	17.66	1.01
L-band	12.12	11.87	0.59

Table 41. Estimated magnitudes for DS21 using multi-wavelength observations carried out with NACO between 2002 and 2018.



**Figure 33.** Observation of DS22 in the H-, K-, and L-band.

	mean	median	std
H-band	19.90	19.90	1.21
K-band	17.40	17.47	0.35
L-band	11.91	11.80	0.54

**Table 42.** Estimated magnitudes for DS22 using multi-wavelength observations carried out with NACO between 2002 and 2018.

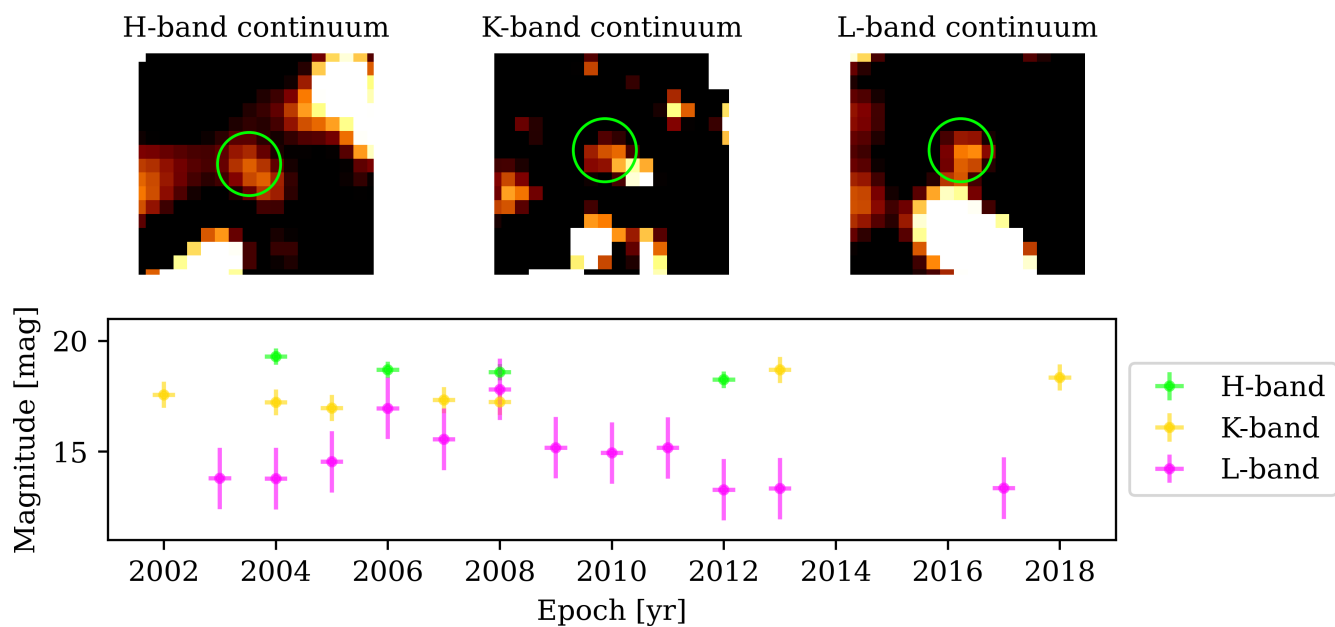


**Figure 34.** Detection of DS23 in various bands observed with NACO.

	mean	median	std
H-band	18.65	18.71	0.37
K-band	17.33	17.62	0.59
L-band	14.73	14.80	1.39

**Table 43.** Estimated magnitudes for DS23 using multi-wavelength observations carried out with NACO between 2002 and 2018.

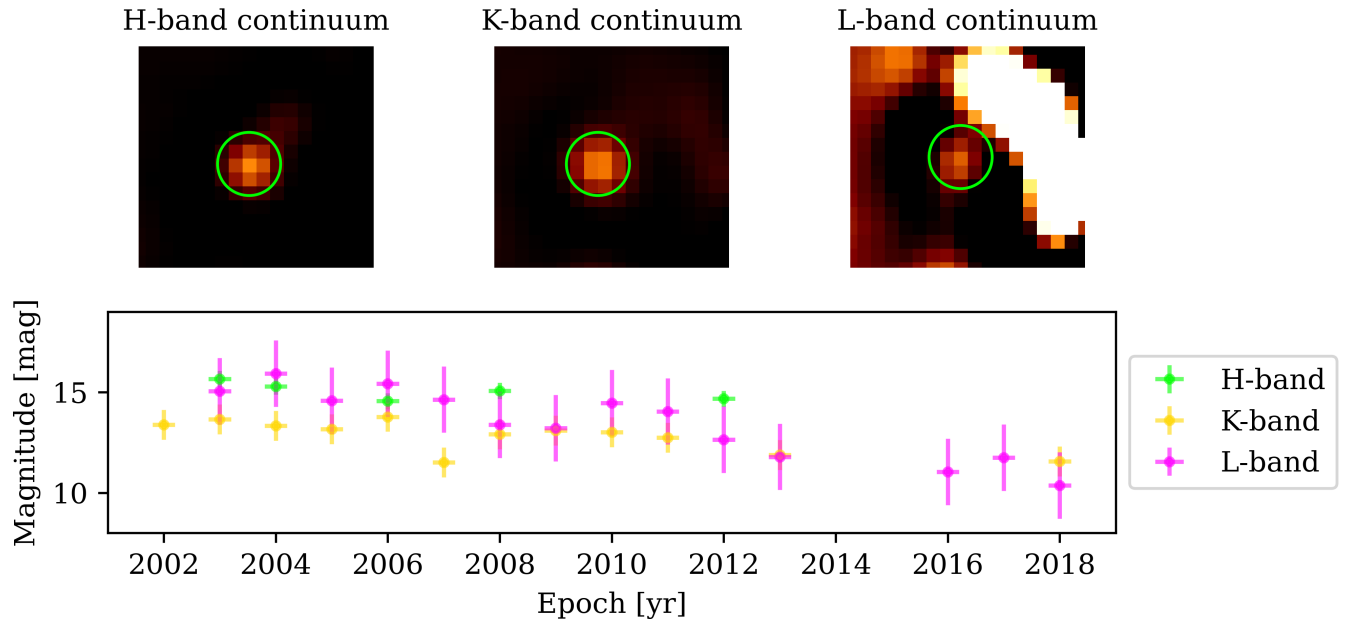


**Figure 35.** Dusty source 24 in several bands observed with NACO between 2002 and 2018.

	mean	median	std
H-band	15.07	15.05	0.40
K-band	13.05	12.83	0.74
L-band	13.71	13.45	1.65

**Table 44.** Estimated magnitudes for DS24 using multi-wavelength observations carried out with NACO between 2002 and 2018.

	mean	median	std
H-band	16.28	16.28	0.30
K-band	14.49	14.29	0.75
L-band	15.46	15.48	1.34

**Table 45.** Estimated magnitudes for DS25 using multi-wavelength observations carried out with NACO between 2002 and 2018.

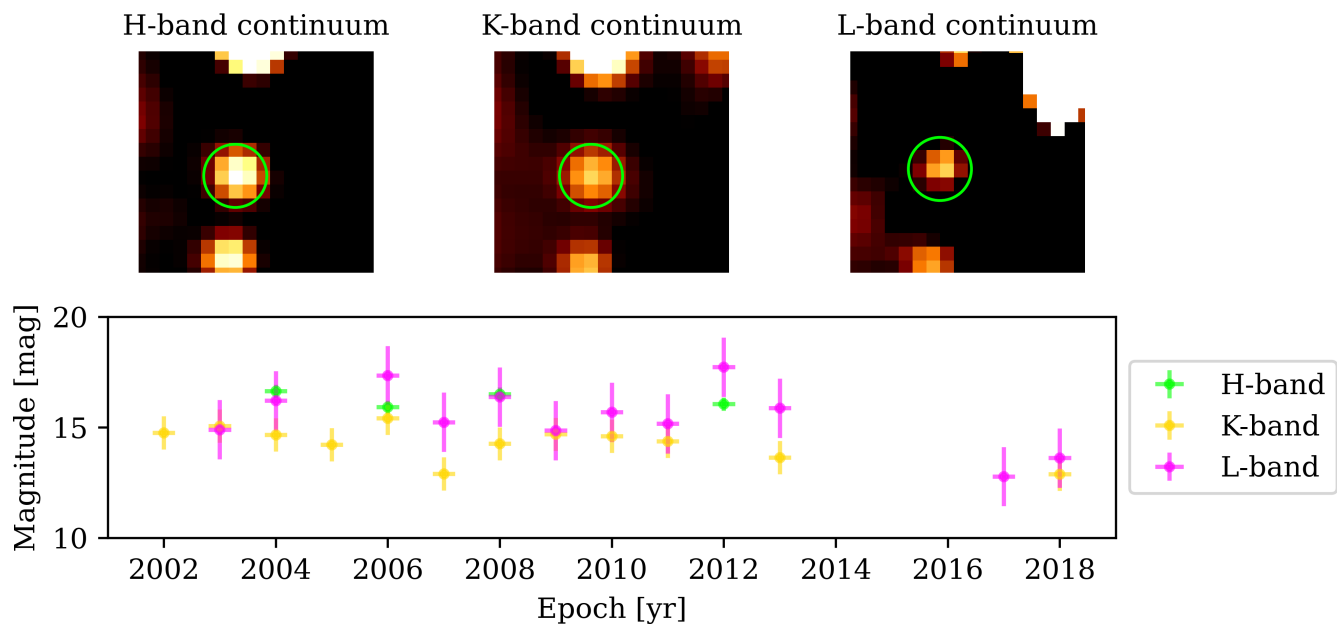


**Figure 36.** The source DS25 located south to DS24. We detect the source in all investigated bands.

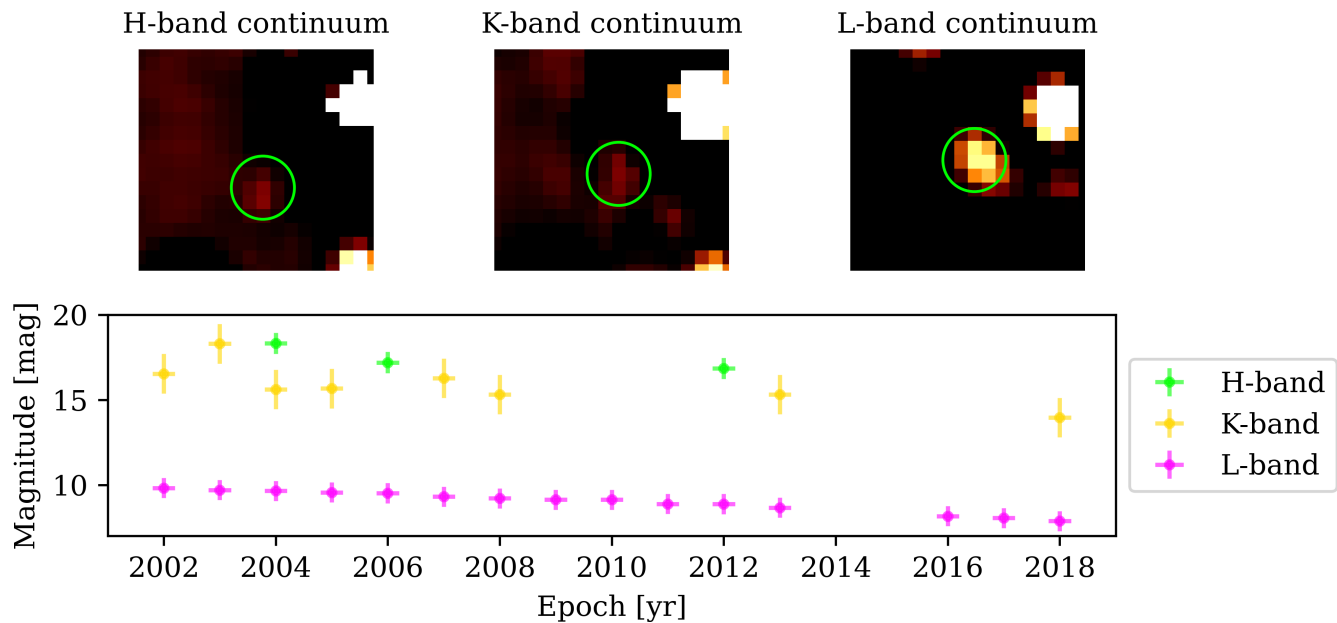


**Figure 37.** Detection of DS26 in the H-, K-, and L-band. The imprint of the dominant PSF wings of the O supergiant E1 in the NIR bands is recognizable.

	mean	median	std
H-band	17.20	17.46	0.62
K-band	15.64	15.87	1.16
L-band	9.13	9.03	0.59

**Table 46.** Estimated magnitudes for DS26 using multi-wavelength observations carried out with NACO between 2002 and 2018.

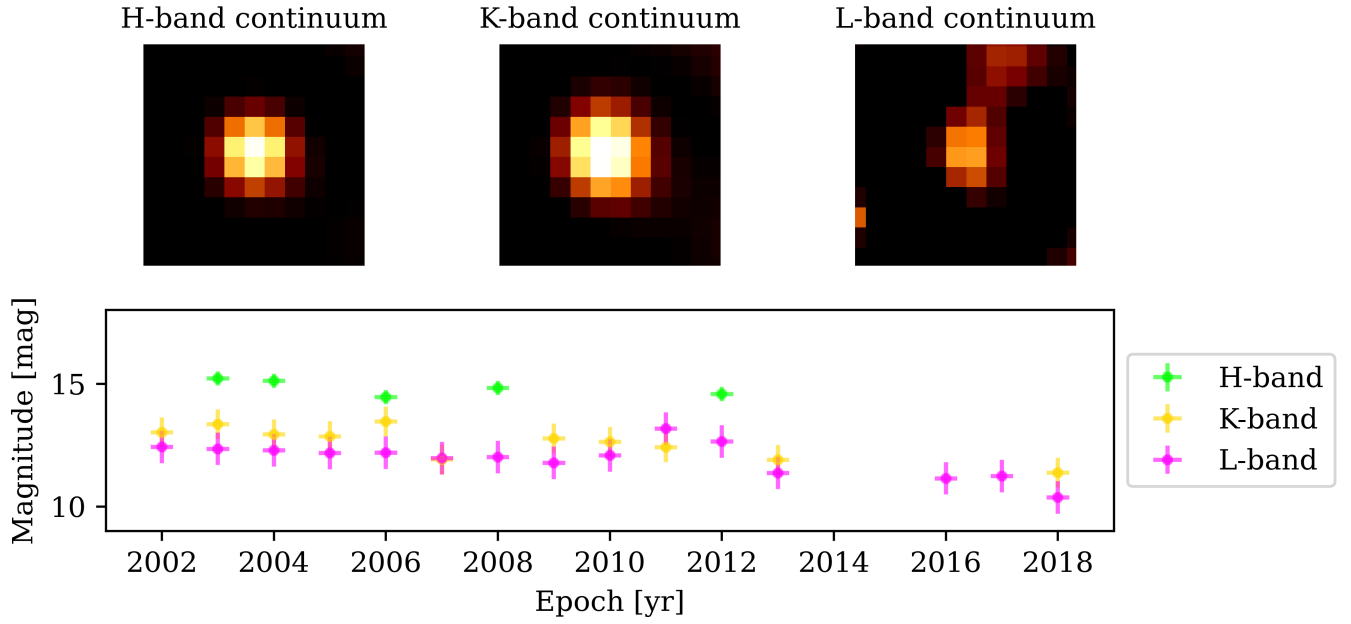


**Figure 38.** Dusty source 27 observed in the H-, K-, and L-band. The source can be observed without confusion close to DS8 (Fig. 24).

	mean	median	std
H-band	14.83	14.83	0.29
K-band	12.77	12.60	0.61
L-band	12.08	11.94	0.66

**Table 47.** Estimated magnitudes for DS27 using multi-wavelength observations carried out with NACO between 2002 and 2018.

	mean	median	std
H-band	16.14	16.30	0.27
K-band	15.80	15.68	0.92
L-band	10.76	10.63	0.42

**Table 48.** Estimated magnitudes for DS28 using multi-wavelength observations carried out with NACO between 2002 and 2018.

	mean	median	std
H-band	16.17	16.21	0.36
K-band	14.42	14.18	0.86
L-band	16.29	16.27	1.33

**Table 49.** Estimated magnitudes for DS29 using multi-wavelength observations carried out with NACO between 2002 and 2018.

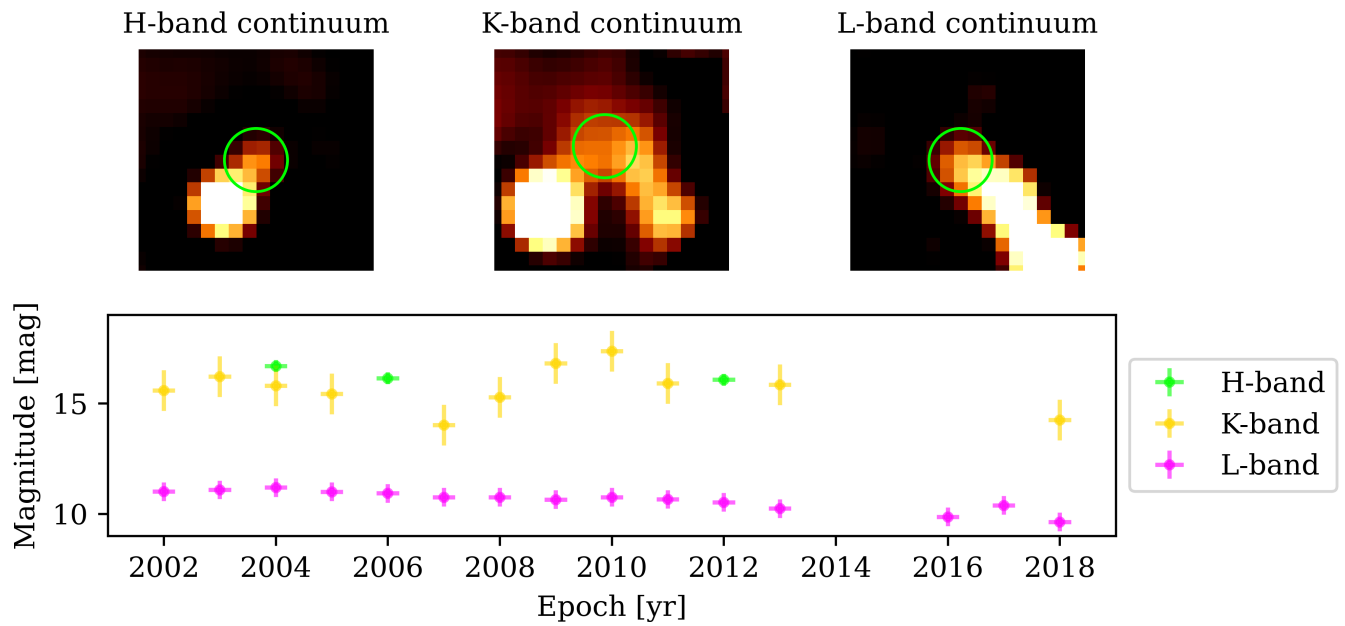


**Figure 39.** Dusty source 28 observed in the H-, K-, and L-band. The source is located at the northern tip of an elongated L-band feature.

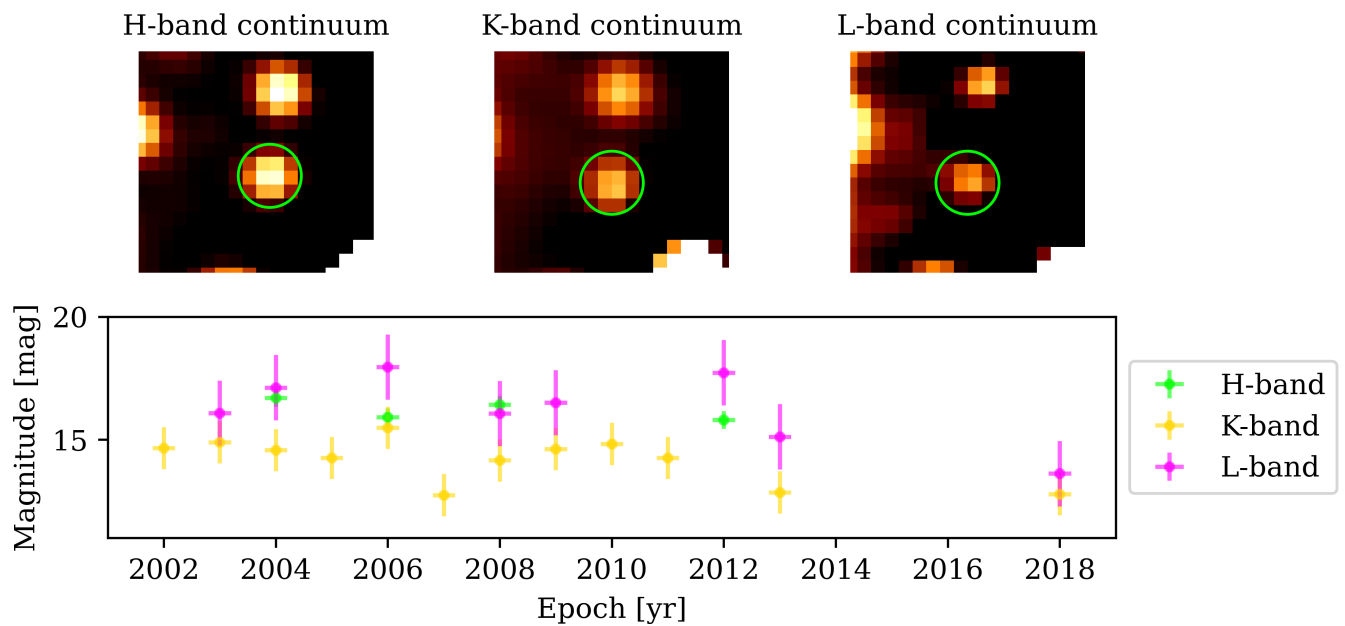


**Figure 40.** Identification of the bright source DS29 in the H-, K-, and L-band. The source is located south of DS25 (Fig. 36) and north of X3 (Peißker et al. 2023b).



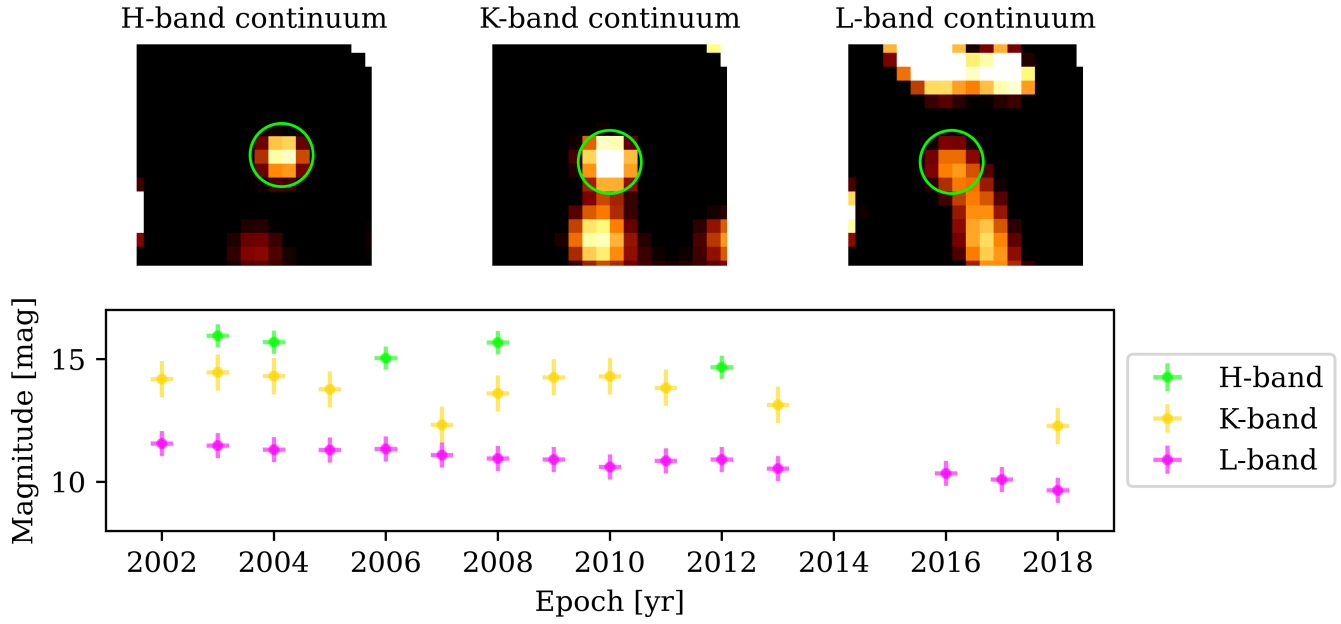


Figure 41. Dusty source 30 located close to the E-star E1.

	mean	median	std
H-band	15.67	15.40	0.47
K-band	13.83	13.67	0.74
L-band	10.92	10.86	0.51

Table 50. Estimated magnitudes for DS30 using multi-wavelength observations carried out with NACO between 2002 and 2018.

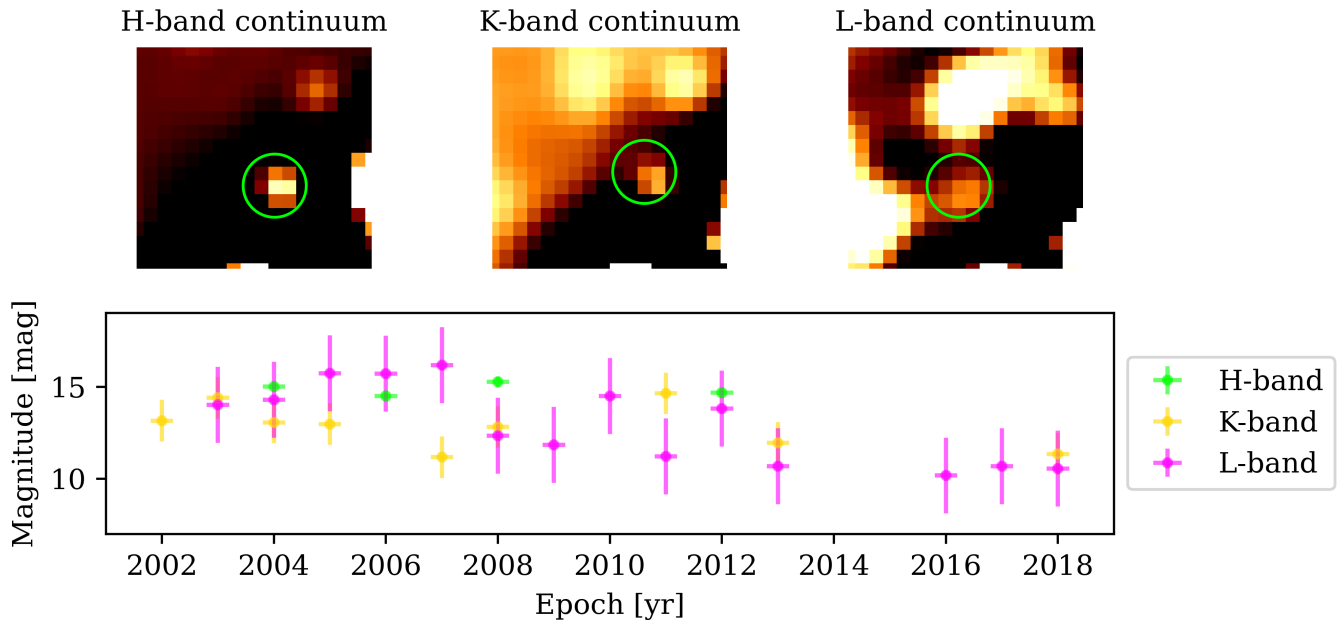
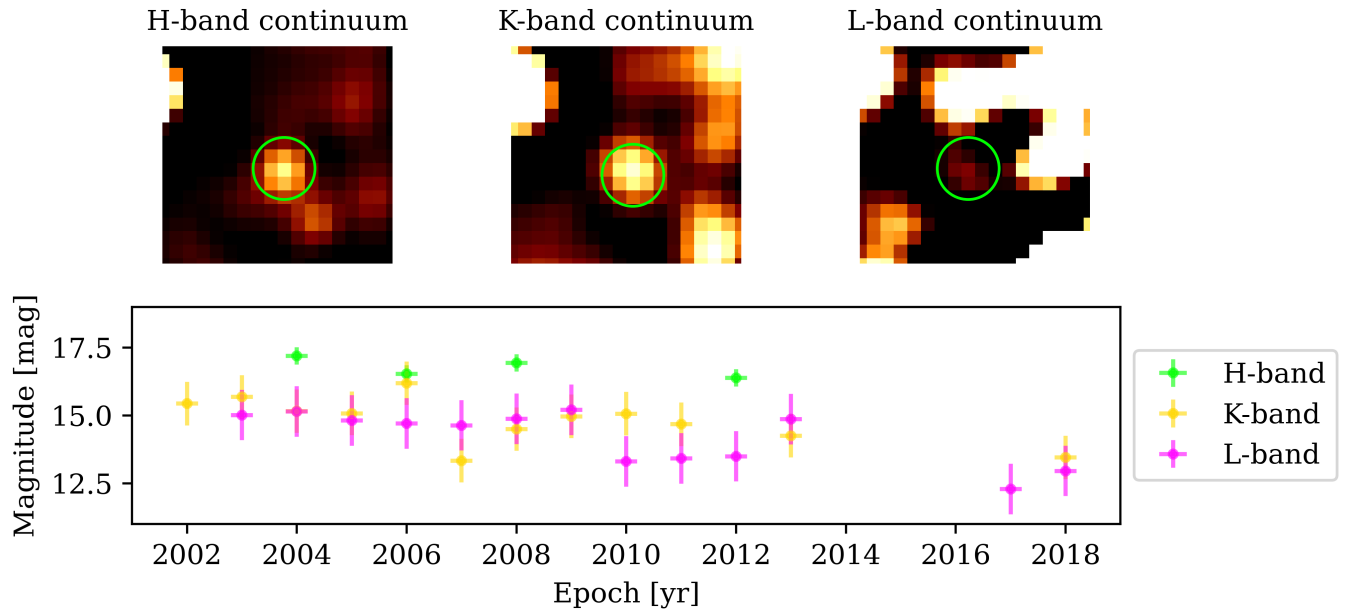


Figure 42. Detection of DS31 in the H-, K-, and L-band suffering from the dominant imprint of the PSF wings of surrounding stars.

	mean	median	std
H-band	14.84	14.85	0.29
K-band	12.97	12.83	1.13
L-band	13.08	12.98	2.06

**Table 51.** Estimated magnitudes for DS31 using multi-wavelength observations carried out with NACO between 2002 and 2018.



**Figure 43.** Observation of DS32 in various band close the bright dusty sources discussed in this work.

	mean	median	std
H-band	16.74	16.76	0.32
K-band	15.02	14.82	0.80
L-band	14.71	14.21	0.93

**Table 52.** Estimated magnitudes for DS32 using multi-wavelength observations carried out with NACO between 2002 and 2018.

	mean	median	std
H-band	18.39	19.00	1.11
K-band	16.16	16.01	0.62
L-band	9.92	9.80	0.57

**Table 53.** Estimated magnitudes for DS33 using multi-wavelength observations carried out with NACO between 2002 and 2018.

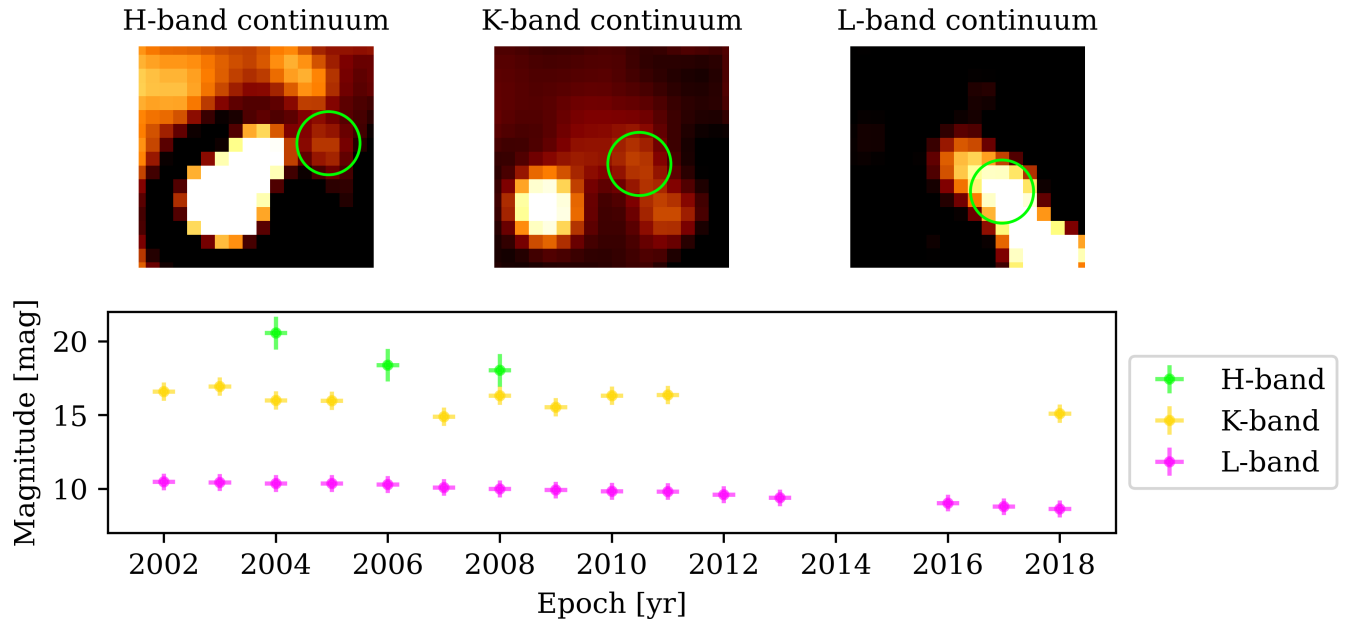


**Figure 44.** Identification of DS33 in the elongated L-band feature consisting of several stars.